

## A SURVEY AND ANALYSIS OF *SPITZER* INFRARED SPECTROGRAPH SPECTRA OF T TAURI STARS IN TAURUS

E. FURLAN<sup>1</sup>, L. HARTMANN<sup>2</sup>, N. CALVET<sup>2</sup>, P. D'ALESSIO<sup>3</sup>, R. FRANCO-HERNÁNDEZ<sup>3</sup>, W. J. FORREST<sup>4</sup>,  
D. M. WATSON<sup>4</sup>, K. I. UCHIDA<sup>1</sup>, B. SARGENT<sup>4</sup>, J. D. GREEN<sup>4</sup>, L. D. KELLER<sup>5</sup>, T. L. HERTER<sup>1</sup>

*To appear in ApJS, 2006 August*

### ABSTRACT

We present mid-infrared spectra of T Tauri stars in the Taurus star-forming region obtained with the *Spitzer* Infrared Spectrograph (IRS). For the first time, the 5–36  $\mu\text{m}$  spectra of a large sample of T Tauri stars belonging to the same star-forming region is studied, revealing details of the mid-infrared excess due to dust in circumstellar disks. We analyze common features and differences in the mid-IR spectra based on disk structure, dust grain properties, and the presence of companions. Our analysis encompasses spectral energy distributions from the optical to the far-infrared, a morphological sequence based on the IRS spectra, and spectral indices in IRS wave bands representative of continuum emission. By comparing the observed spectra to a grid of accretion disk models, we infer some basic disk properties for our sample of T Tauri stars, and find additional evidence for dust settling.

*Subject headings:* circumstellar matter — planetary systems: protoplanetary disks — stars: pre-main sequence — infrared: stars

### 1. INTRODUCTION

The Taurus-Auriga star-forming region is a relatively nearby (140 pc; Kenyon et al. 1994b; Bertout et al. 1999) molecular cloud complex, which is characterized by lower extinction and more isolated, low-mass star formation than other star-forming regions at comparable distances, like Ophiuchus (Kenyon & Hartmann 1995, hereafter KH95). It is therefore fairly well-studied from wavelengths ranging from the X-rays to the radio and used to test theoretical predictions of the star formation process. Given the young age of the Taurus complex (1–2 Myr), many of its pre-main-sequence stars are still surrounded by material left over from their formation process and accrete gas and dust from circumstellar disks.

Dust grains in these disks are heated by irradiation from the star and from the accretion shocks at the stellar surface, as well as by local viscous dissipation (D'Alessio et al. 1998), and emit excess emission, i.e. at flux levels above those expected from a stellar photosphere, at infrared wavelengths. Most disks have flared disk surfaces, i.e. the disk thickness increases more steeply than just linearly with radius; this flaring allows disks to absorb more radiation from the central source than a flat, thin disk, and thus to become hotter (see, e.g., Kenyon & Hartmann 1987).

Over time, accretion rates decrease, and, while the disk

material is depleted, some of the dust and gas could be built into planets. Young, low-mass ( $\lesssim 2M_{\odot}$ ) stars surrounded by these accretion disks are referred to as classical T Tauri stars (CTTSs). Once accretion has virtually stopped and disks are either passive, i.e. only reprocessing stellar radiation, or already dissipated, a young star is called a weak-lined T Tauri star (WTTS). The distinction between CTTSs and WTTSs is based on the equivalent width of their H $\alpha$  emission line (EW[H $\alpha$ ]): CTTSs have broad and asymmetric H $\alpha$  line profiles, which are generated in the magnetospheric accretion flows (Muzerolle et al. 2003a), resulting in an EW[H $\alpha$ ] larger than 10 Å, while WTTSs have an EW[H $\alpha$ ] of less than 10 Å; in WTTSs, strong surface magnetic fields provide the energy for strong X-ray, UV, and H $\alpha$  emission.

Based on an evolutionary sequence derived from the shape of the spectral energy distribution (SED) in the infrared (Lada & Wilking 1984; Lada 1987), young, low-mass stars are divided into three classes. Class I objects have rising SEDs over the infrared spectral range, while Class II objects have either flat or somewhat decreasing SEDs; Class III objects have little infrared excess, and their SEDs can be understood as reddened stellar photospheres for wavelengths  $\lesssim 10 \mu\text{m}$ . Thus, Class II objects are characterized by the presence of mid-infrared excess emission due to dust in circumstellar disks, while Class III objects have, for the most part, already dissipated their disks, and therefore their infrared flux is close to photospheric levels. Classical T Tauri stars fall into the Class II category; weak-lined T Tauri stars can be considered Class II or Class III objects, depending on the presence of disks around them. When a young star has almost completely dissipated its circumstellar material, it is usually classified as a Class III object. Therefore, all Class III objects are WTTSs, but not all WTTSs are Class III objects, as defined by their infrared SEDs.

Mid-infrared spectra of T Tauri stars (mostly CTTSs) reveal the details of the thermal emission by dust grains in the inner regions of circumstellar disks, from a few tenths to several AU from the central object. By de-

<sup>1</sup> Center for Radiophysics and Space Research, 208 Space Sciences Building, Cornell University, Ithaca, NY 14853; furlan@astro.cornell.edu, kuchida@astro.cornell.edu, tlh10@cornell.edu

<sup>2</sup> Department of Astronomy, The University of Michigan, 500 Church St., 830 Dennison Building, Ann Arbor, MI 48109; ncalvet@umich.edu, lhartm@umich.edu

<sup>3</sup> Centro de Radioastronomía y Astrofísica, UNAM, Apartado Postal 3-72 (Xangari), 58089 Morelia, Michoacán, México; p.dallessio@astrosmo.unam.mx

<sup>4</sup> Department of Physics and Astronomy, University of Rochester, Rochester, NY 14627; forrest@pas.rochester.edu, dmw@pas.rochester.edu, bsargent@pas.rochester.edu, joel@pas.rochester.edu

<sup>5</sup> Department of Physics, Ithaca College, Ithaca, NY 14850; lkeller@ithaca.edu

ripping the structure and composition of the dust in protoplanetary disks, we can study the conditions and processes leading to planetary formation. In particular, dust growth and settling are seen as key steps in the formation of larger bodies.

The Spitzer Space Telescope (Werner et al. 2004) enables us, for the first time, to obtain spectra from 5 to 36  $\mu\text{m}$  of T Tauri stars covering a variety of flux densities, from tens of mJy to tens of Jy. As part of a larger Infrared Spectrograph<sup>6</sup> (IRS; Houck et al. 2004) guaranteed-time observing program, we observed 150 young stellar objects in the Taurus-Auriga star-forming region, ranging in evolutionary state from the protostellar, or Class I, stage, when a forming star is still enshrouded by an envelope, to the Class II and III stages, when disk material is accreted and dissipated.

Our Taurus sample is largely based on the sample studied by KH95, who compiled and analyzed photometric data of known young stellar objects in the Taurus-Auriga star-forming region. Here we present 85 IRS spectra of Class II objects and 26 spectra of Class III objects; the remaining spectra of the Class I objects in our sample will be presented in a subsequent paper. We analyze the spectral energy distributions and IRS spectra of Class II and III objects in terms of common features and peculiarities arising from their disk structure, the properties of dust grains embedded within, and their surrounding environment. The large-scale environment has little impact on objects in Taurus, unlike young stars in OB associations or young clusters, where the cluster members are subject to the influence of high-energy radiation and powerful winds from the OB stars.

In § 2 we introduce our *Spitzer* IRS observations and data reduction; in § 3 we present spectral energy distributions, from the optical to the far-infrared, of the Class II and III objects in our sample, as well as a morphological sequence of the IRS spectra of our 85 Class II objects; in § 4 we compare our data with a set of accretion disk models to infer some disk properties, present a new median of mid-infrared fluxes of Class II objects in Taurus, and estimate upper limits for dust masses around our Class III objects. We discuss some of our results in § 5, and give our conclusions in § 6.

## 2. OBSERVATIONS AND DATA REDUCTION

All but three of our Taurus targets were observed with the IRS on *Spitzer* during IRS observing campaigns 3 and 4, from 2004 February 6 to 8, and from 2004 February 27 to March 5. The remaining three targets (FQ Tau, GK Tau, and V830 Tau) were observed during IRS campaign 12, from 2004 August 30 to 31. For all targets the full mid-IR spectrum from 5 to 40  $\mu\text{m}$  was obtained by either using the two low-resolution IRS modules (Short-Low [SL] and Long-Low [LL], 5.2–14  $\mu\text{m}$  and 14–38  $\mu\text{m}$ , respectively,  $\lambda/\Delta\lambda \sim 90$ ) or the SL module and the two high-resolution modules (Short-High [SH] and Long-High [LH], 10–19  $\mu\text{m}$  and 19–37  $\mu\text{m}$ , respectively,  $\lambda/\Delta\lambda \sim 600$ ). The high-resolution modules were usually only used for observations of bright ( $\gtrsim$  a few Jy) targets. While some targets were observed in IRS

staring mode, most of them were observed in mapping mode; with the latter, a  $2 \times 3$  step map on the target was carried out, with three steps separated by three-quarters (for SL) or half (for the other modules) of the slit width in the dispersion direction and two steps of one third of a slit length in the spatial direction. For staring mode observations, the target was placed subsequently in two nod positions along the spatial direction of the slit, at 1/3 and 2/3 of the slit length, respectively.

As a first step in the data reduction process, we fixed all bad pixels in the arrays (identified by the pixel masks, and including the so-called “rogue pixels” in SH and LH) using a simple interpolation over neighboring, good pixels. We then extracted and calibrated our spectra using the SMART software tool (Higdon et al. 2004). When taking low-resolution spectra, the target is first placed on the slit yielding the 2nd order spectrum and then on the slit yielding the 1st order spectrum; each time both orders are observed. We subtracted the sky background by using observations taken at the same nod position, but in different orders. The spectra were extracted using a variable-width column extraction, which varies with the width of the point-spread function, and calibrated with  $\alpha$  Lac (A1 V) and its template spectrum (Cohen et al. 2003). For the high-resolution spectra, the spectra of target and calibrator,  $\xi$  Dra (K2 III), were extracted using a full slit extraction.

Even though we were not able to subtract any sky background from our high-resolution spectra, the contribution from any background emission was only noticeable in our LH spectra. To correct for this contribution, we applied a scalar correction to each LH spectrum to achieve a smooth transition at 19  $\mu\text{m}$ , where SH and LH meet. Our SH spectra usually matched the flux level of our SL spectra in the overlap region between SL and SH (10–14  $\mu\text{m}$ ); given the smaller aperture and shorter wavelength coverage of SH, any background contribution is expected to be negligible. All of our high-resolution data presented in this paper were rebinned to a resolution of  $\lambda/\Delta\lambda = 200$ , and the SH data were truncated below 13  $\mu\text{m}$ . The rebinning of our SH and LH spectra resulted in a clearer representation of the shape of the continuum and in a more homogeneous set of spectra, independent of the modules used for  $\lambda > 14$   $\mu\text{m}$ .

For mapping mode observations, we extracted and calibrated all map positions, but the final spectrum was usually obtained by averaging the two observations in the map’s center. For staring mode observations, the final spectrum is an average of the two nod positions.

We estimate our absolute spectrophotometric accuracy to be of the order of 10%, in some cases as good as 5%. The scatter of neighboring flux values determines our relative accuracy and thus our ability to reliably identify spectral features. This relative accuracy depends not only on the brightness of the object, but also on the modules used: while in SL, and usually also in LL2 (14–21  $\mu\text{m}$ ) and in SH, spectral features above the noise level can be considered real, the LL1 (20–36  $\mu\text{m}$ ) and especially the LH spectra are often dominated by artifacts due to unresolved calibration issues, which makes the identification of real features difficult. Therefore, spectral features beyond 20  $\mu\text{m}$  need careful checking before they are identified. In addition, the wavelength region between 13.5 and 14.5  $\mu\text{m}$ , where SL and LL meet, is

<sup>6</sup> The IRS was a collaborative venture between Cornell University and Ball Aerospace Corporation funded by NASA through the Jet Propulsion Laboratory and the Ames Research Center.

affected by larger uncertainty in the calibration at the order edges and by possible flux mismatches between SL and LL. In some cases a spectral feature seems to appear in this wavelength region; at this point, we are not sure whether this is a real feature or just an artifact introduced by the order edges.

It should be noted that many of our targets are members of close multiple systems, ranging in separation from tenths of an arcsecond to several arcseconds (see Tables 1 and 3). Given that the narrowest IRS slit width is  $3''.6$  (SL), several targets could not be resolved by our observations. For these targets, we show the combined spectrum of the unresolved components; however, in many cases one component clearly dominates the mid-IR spectrum. For a small group of targets, a companion entered only partially in the wider slits ( $4''.7$  for SH,  $10''.6$  for LL,  $11''.1$  for LH) and more fully at the longer wavelength ends of these modules. For these objects we made sure that the contribution of the companion was small before interpreting the object's spectrum, or we excluded the "contaminated" part of the spectrum from the analysis.

A few objects presented problems in their reduction; they will be listed below.

*IT Tau.* This classical T Tauri star is a  $2''.4$  binary. Both components entered the SL and LL slits, even though some flux of the B component was lost at longer SL wavelengths due to the larger size of the point-spread function. The A component should dominate the short-wavelength part of the IRS spectrum; however, it is likely that in LL ( $> 14 \mu\text{m}$ ) A and B contribute about equally, since IRAC measurements (Hartmann et al. 2005a) indicate that the contribution of the B component to the total flux of the system increases from 15% at  $3.6 \mu\text{m}$  to  $\sim 30\%$  at  $8 \mu\text{m}$ . This is also suggested by the IRS spectrum, where we multiplied SL by 1.25 to match it with LL, thus creating a combined spectrum for A and B. Due to this scaling the SL spectrum of IT Tau carries a large uncertainty.

*CW Tau, V773 Tau.* These two objects are part of a mispointed mapping-mode observation. We created continuous IRS spectra by using the brightest map positions for each star; however, due to likely slit losses the absolute flux levels and, to a lesser degree, the shape of the spectra could be off.

*CX Tau, FN Tau, FO Tau.* The spectra of these objects were also affected by mispointed observations, and therefore their IRS spectra are less accurate.

*MHO 3.* This young star is so bright that a small part of its LL spectrum (from about  $22$  to  $26 \mu\text{m}$ ) was saturated.

*AB Aur, RY Tau.* These objects are also very bright and partly saturated the central map position in SL. We recovered an unsaturated spectrum by using an off-center map position for SL and scaled it to match the SH and LH observations.

*V892 Tau.* Due to the brightness of this star, SL and LH were partly saturated. Similarly to RY Tau, we used off-center map positions for SL and LH and matched them to the central map observation of SH.

### 3. THE SAMPLE

#### 3.1. Characterization and Classification

The targets of our Taurus sample were selected from the objects analyzed by KH95, and from objects in the *IRAS* Faint Source Catalogue, selected on the basis of their infrared colors. For the latter, we used a filter on

the brightness and on the 12/25, 25/60, and 60/100  $\mu\text{m}$  flux ratios (the first one being the most important one):  $12/25 < 1.0$ ,  $25/60 < 1.2$ , and  $0.1 < 60/100 < 1.5$ , similar to Beichman et al. (1992). Sources from the Faint Source Catalogue that do not have common names are labeled with their *IRAS* identifier, e.g. F04101+3103.

Spectral indices have commonly been used to classify the SEDs of protostars and pre-main-sequence stars (Lada 1987; Adams et al. 1987). The slope of the SED from the near- to the mid-infrared ( $2.2\text{--}25 \mu\text{m}$ ) in a log-log plot is used to define Class I, II, and III objects:  $n \equiv d \log(\lambda F_\lambda) / d \log(\lambda)$ , where  $n > 0$  identifies a Class I object,  $-2 < n < 0$  a Class II object, and  $n < -2$  a Class III object. A value of  $n$  of  $-3$  is equivalent to a stellar photosphere. However, this is just a simple classification scheme, since it does not take into account the detailed shape of the SED in this wavelength range; it describes the shape of the SED from  $2$  to  $25 \mu\text{m}$  as a simple power law  $\lambda F_\lambda \propto \lambda^n$ . For example, some objects identified as Class I objects might actually be Class II objects with cleared-out inner disk regions, which are characterized by little excess emission at near-IR wavelengths and a large mid-IR excess, resulting in a steep slope of the near- to mid-infrared SED. Only mid-IR spectra reveal spectral features that can aid in the detailed evolutionary classification of a young stellar object, like the presence of the  $10\text{-}\mu\text{m}$  silicate emission feature, which is indicative of a flared circumstellar disk.

We separated our sample into Class II and III sources based on the existence of an infrared excess in the IRS spectral range. This subdivision resulted in a reclassification of some objects previously identified based on their SED slope between  $2$  and  $25 \mu\text{m}$ . Since the  $25\text{-}\mu\text{m}$  data points were usually derived from *IRAS* measurements with limited spatial resolution and lower sensitivity, many previous classifications were more uncertain. Reclassification was done for FP Tau, V836 Tau, VY Tau, and ZZ Tau, which were originally classified as Class III objects (e.g., KH95), and for DI Tau and HBC 423, which were considered Class II objects. Also, we reclassified a few Class II objects as Class I objects due to the presence of ice and silicate absorption features in their IRS spectra, as well as their SED shape; among these objects are CoKu Tau/1, HL Tau, and LkHa 358, which will be included in a subsequent paper.

Accretion signatures, like broad  $\text{H}\alpha$  emission and an excess in the UV or blue spectral range, are an indication for the presence of inner disk material. Combined with magnetospheric accretion models, these signatures are used to derive mass accretion rates (Gullbring et al. 1998; Hartmann et al. 1998; Muzerolle et al. 2003a). Classical T Tauri stars in Taurus have average mass accretion rates of  $\sim 10^{-8} M_\odot \text{yr}^{-1}$ ; accretion rates seem to increase with the mass of the star and also decrease over time (Calvet et al. 2004; Muzerolle et al. 2005; Hartmann et al. 1998).

However,  $\text{H}\alpha$  emission is not necessarily correlated with the presence or absence of a disk; several stars identified as WTTSs do have substantial disk masses, as derived from their millimeter emission (see, e.g., Beckwith et al. 1990), or have considerable mid-IR excesses, as our sample shows. This observational fact could be explained with the presence of inner disk holes: a star with a missing inner disk might not be accreting,

and thus be classified as a WTTS, but still possess a prominent outer disk (e.g., CoKu Tau/4; D’Alessio et al. 2005). On the other hand, all stars with inner disks, as inferred from their infrared excesses, are accreting and thus CTTSs. A few CTTSs (e.g., TW Hya, GM Aur; Jayawardhana et al. 1999; Uchida et al. 2004; Calvet et al. 2005) have low near-IR excesses, but prominent mid-IR excesses, which could be an indication of grain growth in the inner disk. An extreme example is DM Tau (Calvet et al. 2005), which is an accreting T Tauri star but has no near-IR excess.

Many, if not most, T Tauri stars in Taurus have companions. A list of our Class II objects belonging to multiple systems can be found in Table 1; many components are separated by fractions of an arcsecond, and usually they form a binary or a hierarchical quadruple system. The multiplicity of young stars adds complexity when their stellar and circumstellar properties are studied. Some systems are surrounded by circumbinary disks or rings (e.g., Krist et al. 2002), often in addition to a circumprimary and a circumsecondary disk. These disks can be tidally truncated (Artymowicz & Lubow 1994); in general, disks are found well within or outside binary orbits. Therefore, the components of a binary system can be either both CTTSs or both WTTSs, especially in close ( $\lesssim$  a few arcseconds) binary systems, or form a mixed pair (Prato & Simon 1997; Duchêne et al. 1999). A circumbinary reservoir can replenish both the circumprimary and circumsecondary disk; for wider companions, the circumprimary disk is preferentially replenished, resulting in a stronger infrared excess for the primary component (White & Ghez 2001). Depending on the presence of material in its inner disk and thus its accretion signatures, the primary may be classified as CTTS or WTTS; eventually, both components will evolve into Class III objects (and thus WTTSs), once all the disk material has dispersed.

### 3.2. Spectral Energy Distributions

Our full sample of Class II and III objects is listed in Tables 2 and 3, respectively, together with the adopted spectral type, visual extinction  $A_V$ , and T Tauri star type (CTTS, WTTS), taken from the literature (mainly KH95; White & Ghez 2001). Due to the variability of these sources and their multiplicity (where applicable) some measurements are quite uncertain. Several spectral types are not known or are only determined with an uncertainty of a few subclasses, and ages and mass accretion rates depend on the models used to derive them, which can cause uncertainties of an order of magnitude. When derived using the same assumptions, these quantities usually agree within a factor of two. When separating the stars of our sample into CTTSs and WTTSs, we adopted the White & Basri (2003) criteria for CTTSs, where the traditional EW[H $\alpha$ ] boundary of 10 Å between WTTSs and CTTSs is adjusted for spectral type, with a delimiting width smaller than 10 Å for spectral types earlier than K7 and a larger width for spectral types later than M2.5.

For each object with known spectral type, we checked whether the  $A_V$  value from the literature or the  $A_V$  value we derived from observed V-I colors yielded dereddened optical photometry consistent with the intrinsic colors of a main-sequence star with the same spectral type as the

object under consideration. If the dereddened flux values were off, we adjusted the  $A_V$  values, usually by less than a factor of two, until a value was found that brought the observed and expected colors into agreement. Several  $A_V$  values remain uncertain, but since for most Taurus targets the extinction is low, changes in  $A_V$  by less than a factor of two will only minimally affect the shape of the IRS spectrum and will not affect the results of our analysis.

Figure 1 shows the SEDs of the objects in our Class II sample, while figure 2 displays those of our Class III objects. For all objects with measured extinction, their fluxes have been corrected for reddening using the object’s  $A_V$  from Tables 2 and 3 and Mathis’s reddening law (Mathis 1990) with  $R_V = 3.1$ . Included are photometric data points from the optical to the mid-IR mostly from KH95, the 2MASS  $J$ ,  $H$ , and  $K_s$  fluxes, the *IRAS* 12, 25, and 60  $\mu\text{m}$  fluxes, the IRAC 3.6, 4.5, 5.8, and 8.0  $\mu\text{m}$  fluxes (Hartmann et al. 2005a), where available, and the IRS spectrum.

Also shown is the stellar photosphere for those objects with known spectral types; photospheric fluxes were derived from colors of main-sequence stars given in KH95 and normalized at the J-band flux of each object with a spectral type later than G, and at the V-band flux of stars with an earlier spectral type (AB Aur, V892 Tau, RY Tau, and SU Aur). This normalization is based on the fact that for K and early M stars, most of the photospheric radiation is emitted around the J-band, but for earlier spectral types the peak emission shifts to shorter wavelengths. For spectral types earlier than G, the U-band would be better suited for normalization, but since U-band measurements are often poor and very sensitive to extinction, the V-band is a better choice. For F04101+3103, which is of A1 spectral type, the J-band was used for normalization, since it might have an excess in the V-band.

The *IRAS* data shown in the SED plots are mainly from Weaver & Jones (1992), who used co-added *IRAS* data to determine fluxes even for faint objects (as many Class III objects are), which usually fell just below the sensitivity limit of *IRAS*. As can be seen in the comparison with our IRS data, the fluxes for most Class III objects, as determined by Weaver & Jones (1992), were often overestimated, resulting in mid-IR excesses for objects whose emission is actually close to photospheric over the entire infrared range. For objects not included in Weaver & Jones (1992), such as objects with identifiers from the *IRAS* Point Source or Faint Source Catalogues, we used the *IRAS* fluxes from these catalogs, mostly from the latter one.

#### 3.2.1. Class II SEDs

All Class II objects, even the ones defined as WTTS based on the equivalent width of their H $\alpha$  emission line, show a clear mid-IR excess, indicative of the presence of circumstellar disks. The majority of our Class II objects are classical T Tauri stars, either single or in multiple systems; since they show a pronounced accretion signature, indicated by their H $\alpha$  emission or UV excess, it is expected that the circumstellar material in their inner disks generates a substantial infrared excess.

There are only two single WTTSs in our Class II sample: CoKu Tau/4 and IQ Tau. Their SEDs are quite

different from each other; IQ Tau has a substantial excess from the near- to the mid-IR, indicating that at least the disk's inner regions (out to a few AU) are still prominent, while CoKu Tau/4 has no excess up to about  $8\ \mu\text{m}$ . This would indicate that WTTS disks are not all characterized by inner disk clearings, which is anticipated given that they are no longer accreting. However, CoKu Tau/4 might be the only true single WTTS in our sample of Class II objects; it is a so-called transitional disk, where the inner disk has been cleared out, but a prominent outer disk is still present (Forrest et al. 2004; D'Alessio et al. 2005). Even though IQ Tau is classified as a WTTS based on its  $\text{H}\alpha$  equivalent width ( $7.8\ \text{\AA}$ ; Herbig & Bell 1988), it has a U-band excess, which possibly indicates that it is still accreting (Hartmann et al. 1998 derived a mass accretion rate of  $\sim 3 \times 10^{-8}\ \text{M}_{\odot}\ \text{yr}^{-1}$ , while White & Ghez 2001 only derived an upper limit of  $\sim 5 \times 10^{-9}\ \text{M}_{\odot}\ \text{yr}^{-1}$  but noted its red K-L color). Therefore, WTTSs with prominent inner disks seem to be rare, confirming previous results of a short transition time from the CTTS state to a diskless WTTS state (e.g., Simon & Prato 1995).

When comparing the SEDs of single and of multiple T Tauri stars, there are no obvious systematic differences. However, since the IRS spectral range is sensitive to disk emission from a few tenths to a few AU from the star, we only expect to see any effects of multiplicity in close multiple systems ( $\lesssim 0''.5$ , or 70 AU at the distance of Taurus). Disks can surround each component or the entire multiple system; companions will truncate both circumstellar disks (at outer radii 0.2–0.5 times the semimajor axis of the binary) and circumbinary disks (at inner radii 2–3 times the semimajor axis of the binary), depending on the properties of the binary system (Artymowicz & Lubow 1994). In wider systems, inner disks are not influenced by the presence of the other components and are thus expected to have the same properties and lifetimes as disks around single stars.

For most close multiple systems, the SED shows the combined photometry and spectrum of all components, and therefore the mid-IR flux could be generated by circumstellar dust from disks around each component or from a disk surrounding the multiple system. Given that most binaries consist of CTTS pairs, both components will likely contribute to the IRS spectrum.

By using ground-based near-IR photometry (K-band or, where available, L-band) that resolved both components (e.g., White & Ghez 2001), we estimated each object's contribution to the IRS spectrum (see Table 1). There is no clear correlation with binary separation: while in some close ( $\lesssim 1''$ ) systems each component contributes roughly to equal amounts to the IRS spectrum (e.g., GN Tau), in some other close systems one component is the dominating one (e.g., V955 Tau). In the few mixed-pair binaries of our sample, where one component is a CTTS and the other a WTTS, the primary component is usually the CTTS and dominates the mid-IR spectrum. Therefore, the IRS spectrum shows emission mostly from the circumprimary disk. This implies that the disk around the CTTS is either preferentially replenished or was formed as a more massive disk; the companion ends up with a smaller disk and a lower-mass star. This would also indicate that each system is

strongly shaped by its initial conditions, i.e. the mass of each cloud fragment that formed a binary component, its kinematics, and whether other components formed nearby.

Almost all of the Class II objects display pronounced 10- and 20- $\mu\text{m}$  emission features due to silicates. Usually the 10- $\mu\text{m}$  feature is stronger than the 20- $\mu\text{m}$  feature, and it also varies from object to object due to different grain composition and sizes. A smooth 10- $\mu\text{m}$  feature centered around  $9.8\ \mu\text{m}$  is indicative of amorphous silicates (similar to the interstellar medium), while a structured 10- $\mu\text{m}$  feature (see, e.g., the IRS spectrum of DH Tau) reveals the presence of crystalline silicates, likely processed from amorphous silicates in the circumstellar environment (Sargent et al. 2006; Forrest et al. 2004). In a separate paper, we explore the correlations between disk properties and the structure and strength of the 10- $\mu\text{m}$  silicate feature (D. M. Watson et al. 2006, in preparation).

In addition to the almost ubiquitous presence of silicate emission features, we note the close to complete absence of PAH emission features in our objects of spectral type later than about G1, with the possible exception of UX Tau A (see section 3.3). PAH emission is typical for the more massive counterparts of T Tauri stars, the Herbig Ae/Be stars (see, e.g., Meeus et al. 2001), and their absence in the circumstellar environment of lower mass stars is probably a result of the weaker UV radiation field of these stars.

### 3.2.2. Class III SEDs

All Class III objects in our sample have narrow  $\text{H}\alpha$  equivalent widths – all of them are WTTSs – and are not accreting within the detection limits, indicative for dispersal of their inner disks. Our IRS spectra support this finding: almost all Class III mid-IR spectra are photospheric. Even though the dispersal of disk material would suggest that these objects are more evolved, and thus older, the ages of Class III objects do not seem to be systematically larger than those of Class II objects, which are supposedly in an earlier phase of evolution (see, e.g., White & Ghez 2001). It appears that the timescales for circumstellar disk evolution are rather determined by the initial conditions and the specific environment around a young star than set by some universal processes. Young Class III objects ( $\lesssim 1\text{--}2\ \text{Myr}$ ) apparently dispersed their circumstellar material faster than some long-lived Class II objects; multiplicity could play a role (see, e.g., Meyer et al. 1997) but is likely not the only factor.

Three of our Class III objects have nearby companions with infrared excesses that partly entered the  $10''.6$  wide LL slit but not the narrower SL slit: DI Tau, HBC 423, and HP Tau/G2. DI Tau is separated by  $15''$  from DH Tau, which is a classical T Tauri star (see figure 1 for the SED of DH Tau). In the case of HBC 423, V955 Tau, which is  $10''$  away, and, to a small degree, HBC 422, which is  $26''$  away, contribute to the flux past  $14\ \mu\text{m}$  (see figure 1 for the SED of V955 Tau). HP Tau/G2 is  $10''$  from HP Tau/G3; both stars contribute to the LL flux, and in addition light of HP Tau (see figure 1), which is  $21''$  from HP Tau/G2, probably entered in LL, especially toward the longer wavelengths. Given that the fluxes of DI Tau, HBC 423, and HP Tau/G2 are at photospheric

levels over the SL wavelength range (5–14  $\mu\text{m}$ ), but show a sharp increase where LL starts (at 14  $\mu\text{m}$ ), it is very likely that all of their apparent excess is caused by their companion(s). For these sources, we only show their SL spectra.

Two more Class III objects show a similar behavior to the three previously mentioned objects: HBC 427 and V819 Tau. These two stars do not have any known companions with infrared excesses; however, for each of them the 2MASS K-band image shows a nearby source that likely contaminated the LL observation. V819 Tau is separated by about  $10''$  from a faint source to the south, whose flux in the K-band is about 30 times smaller than that of V819 Tau. HBC 427 has a “companion” about  $15''$  to the southeast, which is about half as bright as HBC 427 in the K-band. Given that either “companion” did not fully enter the LL slit, but still likely contributed to the flux in this module due to the sharp rise in flux at the SL-LL boundary, they might have substantial mid-IR excesses. Since the mid-IR flux of those nearby sources is not known, we cannot determine which fraction of the infrared excess we observe is due to the target itself; the almost photospheric flux levels of HBC 427 and V819 Tau at wavelengths shorter than 14  $\mu\text{m}$  indicates that the intrinsic infrared excess is likely small.

V410 X-ray 3 seems to have an excess at wavelengths longer than 20  $\mu\text{m}$ , but since its spectrum is very faint in that wavelength region ( $\sim 2$  mJy), it could be an artifact of the extraction. This object is one of the lowest-mass T Tauri stars in our sample; its spectrum was first presented in Furlan et al. (2005a).

HBC 356, Hubble 4, and L1551-51 were too faint beyond 14  $\mu\text{m}$ , so only their SL spectra could be extracted. For HBC 392, LkCa 1, and LkCa 21, the longer-wavelength part of LL (beyond 21  $\mu\text{m}$ ) was too faint, so their spectra include only a part of the LL spectrum.

### 3.3. Notes on Individual Objects

#### 3.3.1. 04303+2240, 04370+2559, 04385+2550, CoKu Tau/3, FV Tau, Haro 6-13, MHO 3, V410 Anon 13

These objects are all highly reddened T Tauri stars with an  $A_V$  larger than about 5 mag (see Table 2); in addition, 04303+2240 and Haro 6-13 have relatively high mass accretion rates (White & Hillenbrand 2004). 04370+2559 has a companion that is likely a substellar object (Itoh et al. 1999, 2002). 04385+2550, also known as Haro 6-33, has been considered as a Class I object by some authors based on its SED shape and bolometric temperature (e.g., Motte & André 2001; Young et al. 2003). It is detected at sub-mm and mm wavelengths and is somewhat extended in the former, but not in the latter wavelength range (Motte & André 2001; Young et al. 2003). On the other hand, the high extinction could indicate that 04385+2550 is a Class II object seen edge-on. V410 Anon 13 is a very low-mass classical T Tauri star, whose IRS spectrum was already studied in Furlan et al. (2005a).

The objects 04370+2559, CoKu Tau/3, and FV Tau have a CO<sub>2</sub> ice absorption feature at 15.2  $\mu\text{m}$  in their spectra. Since the lack of other ice features, the presence of a prominent silicate emission feature, and the SED shape suggest that these objects are T Tauri stars and

not protostars surrounded by an envelope, the CO<sub>2</sub> ice absorption feature is likely due to dense cold material along the line of sight to these objects. The relatively high extinction towards all of these objects would support the idea of molecular cloud material causing the CO<sub>2</sub> ice feature.

#### 3.3.2. CZ Tau B, DG Tau, DR Tau, FS Tau (Aa+Ab), HN Tau A, XZ Tau B

According to White & Ghez (2001), these T Tauri stars have veiled optical spectra, unusually red K–L colors ( $> 1.4$  mag), and, where measured, large H $\alpha$  equivalent widths, indicative of high accretion rates. Therefore, their luminosities and temperatures are uncertain, and thus extinctions, ages, and mass accretion rates are not well determined. These stars might be experiencing an episodic phase of high accretion, which could be accompanied by a larger amount of extinction (White & Ghez 2001).

*CZ Tau.* CZ Tau has a peculiar IRS spectrum, which has a positive slope from 5 to 20  $\mu\text{m}$ , but falls sharply beyond 20  $\mu\text{m}$ . Based on their K- and L-band flux ratios (White & Ghez 2001), the two components of this 0'32 binary are probably contributing in equal measure to the IRS spectrum, but the B component is in a high-accretion state and therefore likely suffering from larger extinction. This could explain the shorter-wavelength slope of the IRS spectrum, but not the longer-wavelength drop; for the latter, disk truncation might be responsible.

*DG Tau, DR Tau.* These two objects are the only single stars in this sample of high-accretion-rate stars; 04303+2240 could be added to this subgroup, too. It seems that for these objects the excess emission from the accretion shock strongly veils the emission of the photosphere, possibly dominating the emission from the ultraviolet to the optical (see, e.g., Gullbring et al. 1998, 2000). Since it is difficult to determine the extinction and the flux level of the photosphere, we did not add stellar photospheres in their SED plots; we also did not attempt to adjust the extinction, but instead adopted the values published in the literature.

DG Tau is a “flat-spectrum” T Tauri star, i.e. it has a flat SED over the infrared spectral range. Like other “flat-spectrum” sources, it is likely surrounded by an infalling envelope (e.g., Calvet et al. 1994). Wooden et al. (2000) reported variations from emission to absorption behavior in the 10- $\mu\text{m}$  silicate feature, in addition to changes in dust mineralogy, on the timescales of months to years. Our IRS spectrum, taken in 2004 March, shows a very weak 10- $\mu\text{m}$  silicate emission feature whose shape indicates that crystalline silicates might be present. We note that the flux level of the IRS spectrum is much lower than the *IRAS* fluxes at 12 and 25  $\mu\text{m}$ . This is partly an aperture effect, since the *IRAS* beam included flux contributions from DG Tau, DG Tau B (a Class I object about half as bright as DG Tau), and FV Tau (a Class II source, 0.25–0.5 times fainter than DG Tau), while the IRS observed only DG Tau (with slit sizes of 3'6, 4'7, and 11'1). Part of the discrepancy could also be caused by intrinsic variability of the target(s).

*FS Tau.* FS Tau A and B, which are separated by  $20''$ , are both surrounded by reflection nebulosities (Krist et al. 1998; White & Ghez 2001); in our IRS observations, only the sub-arcsecond binary FS Tau

Aa+Ab was included. Given the smaller aperture of the IRS, we note that the IRS fluxes are considerably lower than the *IRAS* fluxes of FS Tau.

*HN Tau and XZ Tau.* In the HN Tau and XZ Tau binary systems, both components are classical T Tauri stars, but the one component with the high mass accretion rate is clearly dominating the IRS spectrum (HN Tau A and XZ Tau B, respectively).

### 3.3.3. *AB Aur, F04101+3103, V892 Tau*

These three objects are Herbig Ae/Be stars and therefore more massive and brighter than classical T Tauri stars. For AB Aur, we adopted the spectral type (A0) and extinction ( $A_V=0.25$  mag) from DeWarf et al. (2003). F04101+3103 was assigned an A1 spectral type by Kenyon et al. (1990); in its SED plot, we used the *BVRI* photometry of Iyengar & Parthasarathy (1997).

The spectral type of V892 Tau published in the literature varies from B9, with an extinction of  $A_V=8.85$  mag, to A6 and an extinction of 4 mag (e.g., Strom & Strom 1994; Kenyon & Hartmann 1995). Here, we adopted the earlier spectral type and higher extinction (adjusted somewhat to  $A_V=8.0$ ), as it yields a more realistic SED. The high extinction is also supported by evidence of a nearly edge-on disk around V892 Tau (Haas, Leinert, & Richichi 1997). In addition, for V892 Tau we used the B-, V-, and R-band measurements from the Herbig-Bell Catalog (Herbig & Bell 1988, hereafter HBC), and the R-I color from Strom & Strom (1994), since KH95 only list a V-band magnitude. The R and I photometry of Strom & Strom (1994) is about 1 mag brighter than the HBC measurements, probably a sign of variability or an aperture effect.

In the SED plots, the photospheres of AB Aur and V892 Tau were normalized at V; both objects already have an excess in the J-band. Even though the near-IR excess suggests the presence of an inner disk around V892 Tau, it is classified as a WTTS. This could be explained by its early spectral type, for which the identification as WTTS based on its narrow H $\alpha$  emission line profile might not be valid (Calvet et al. 2004).

We note that V892 Tau is a 60 mas binary, and it also has a faint T Tauri star companion 4".1 away (Smith et al. 2005). Our IRS observations included all three stars, but the subarcsecond binary likely dominates the flux of the system.

### 3.3.4. *GG Tau, UX Tau, UZ Tau, V773 Tau*

All of these four objects form quadruple systems, the highest-order multiple systems in our sample.

*GG Tau.* GG Tau is a hierarchical quadruple system, consisting of two pairs of binaries: components Aa and Ab are separated by 0".25, Ba and Bb by 1".48, and components A and B by  $\sim 10''$ . Our observations were pointed at the A binary; while in LL some flux of the B components also entered the slit, they are so much fainter than A that their contribution is negligible. In fact, the GG Tau B components are of late M spectral type, and Bb is most likely a brown dwarf (White et al. 1999). All four stars exhibit accretion signatures in the form of strong H $\alpha$  emission and are therefore surrounded by accretion disks; additionally, GG Tau A is surrounded by a circumbinary ring (e.g., McCabe, Duchêne, & Ghez 2002).

*UX Tau.* UX Tau consists of component A, separated by 2".6 from C, and by 5".9 from B, which itself is a subarcsecond binary. Both A and C entered the SL slit, and in LL all four components contributed to the IRS spectrum. However, the A component is likely to dominate the mid-IR spectrum; it is the only classical T Tauri star of the system (the other components are classified as WTTSs), and it is brighter than components B and C by a factor of 7 and 24, respectively, in the L-band (3.6  $\mu\text{m}$ ; White & Ghez 2001). To only contribute substantially beyond 13  $\mu\text{m}$ , but not at 10  $\mu\text{m}$  and shorter wavelengths, the other components would have to have very red spectra.

The peculiar IRS spectrum of UX Tau suggests the presence of some material in the inner disk and a substantial outer disk. Since the other stars are a few arcseconds away, they are unlikely to influence the disk around the primary. UX Tau A has a very weak 10- $\mu\text{m}$  silicate emission feature, but a prominent 20- $\mu\text{m}$  feature, as well as some small peaks beyond about 20  $\mu\text{m}$  possibly indicating the presence of crystalline silicates. Interestingly, UX Tau A shows a PAH feature at 11.3  $\mu\text{m}$  (forsterite has a feature centered at slightly shorter wavelengths that is wider than the feature we observe); the 6.2 and 7.7  $\mu\text{m}$  PAH features could be hidden by the strong continuum. Since UX Tau A's spectral type is K5, and we usually do not observe any PAH features in stars later than G, it would be the latest spectral type in our sample to show any PAH features. This latter fact might partly be due to the weak silicate emission of UX Tau, which allows us to easily identify the 11.3  $\mu\text{m}$  PAH feature.

*UZ Tau.* In the UZ Tau system, component A, a spectroscopic binary, is separated by 3".5 from the  $\sim 0".4$  binary Ba-Bb. All four components entered the IRS slits. UZ Tau A is surrounded by an accreting circumbinary disk; even though the B components are also surrounded by accretion disks, their outer disks are likely truncated (Jensen, Koerner, & Mathieu 1996; Simon, Dutrey, & Guilloteau 2000; Hartigan & Kenyon 2003). Therefore, the A component likely dominates the IRS spectrum. We note that in the SED plot the IRS fluxes are below the IRAC data points, which are the sum of the measured fluxes of UZ Tau e (i.e., A) and UZ Tau w (i.e., Ba+Bb); this could indicate that the IRS observations were somewhat mispointed and therefore missing part of the flux of the brighter component (which is  $\sim 5$ –7 times brighter than the B components in the IRAC bands).

*V773 Tau.* V773 Tau is a very tight quadruple system: all four stars are found within 0".25 from each other. V773 Tau AB is a spectroscopic binary and a WTTS, V773 Tau C is a CTTS, and the fourth component, discovered by Duchêne et al. (2003), is an optically faint, and therefore deeply embedded, "infrared companion". V773 Tau D gradually increases in brightness from 2  $\mu\text{m}$ , where it is the faintest object in the system, to 4.7  $\mu\text{m}$ , where it is the brightest source (Duchêne et al. 2003). Thus, component D is likely the dominating source in the IRS spectrum.

The SED of V773 Tau is somewhat similar to that of V807 Tau, which consists of a primary CTTS and a close binary WTTS, with separations of less than 0".5 between the components: both systems have little excess emission in the near-IR, a very weak 10- $\mu\text{m}$  silicate feature, but

a prominent 20- $\mu\text{m}$  feature, suggesting that their inner disks have been partially cleared, possibly due to the action of the close components in these systems.

### 3.3.5. *HK Tau*

HK Tau consists of two components, separated by  $2''.3$ ; while the primary is surrounded by a face-on disk, the secondary's disk is oriented edge-on (Stapelfeldt et al. 1998). We were not able to resolve the binary in our IRS observations, but the primary is likely much brighter than the secondary (flux ratios of 21 and 30 in the K- and L-band, respectively; White & Ghez 2001).

### 3.3.6. *RY Tau and SU Aur*

These two stars are the only early G-type T Tauri stars in our sample. As with the SED plots of the Herbig Ae/Be stars, we normalized their photospheres at V. The IRS spectra of both objects display pronounced 10- and 20- $\mu\text{m}$  silicate features; the smoothness of the 10- $\mu\text{m}$  feature indicates that the dust is mostly amorphous.

SU Aur has an infrared excess already in the J-band, which would point to the presence of inner disk regions. Previous determinations of its  $\text{EW}[\text{H}\alpha]$  of 2 Å indicated that it likely is a WTTS (Kenyon et al. 1998), in apparent conflict with the existence of an inner disk; however, given its G1 spectral type, the classification as a CTTS or WTTS based on  $\text{EW}[\text{H}\alpha]$  might not be appropriate (see White & Basri 2003). Recent measurements by Calvet et al. (2004) suggest that it has a wide  $\text{H}\alpha$  equivalent line width, typical of CTTSs. Also, its UV excess reveals that it is accreting; it has an inferred mass accretion rate of  $\sim 5 \times 10^{-9} M_{\odot} \text{ yr}^{-1}$  (Calvet et al. 2004). Therefore, SU Aur is probably a classical T Tauri star. However, it has a peculiarity in its spectrum: it displays PAH emission features like those seen in Herbig Ae/Be stars (Meeus et al. 2001; Acke & van den Ancker 2004; Sloan et al. 2005) but not in the late-type young stars of our sample.

### 3.3.7. *T Tau*

T Tau is a triple system; the northern and southern component are separated by  $0''.7$ , while the southern binary has an orbital separation of  $0''.1$ . The northern component, which is more massive and the source detected in the optical, is not very veiled, while the southern components are heavily extinguished and might therefore be surrounded by an envelope (Calvet et al. 1994; Koresko et al. 1997). In the infrared, the southern components vary in brightness due to variable extinction; in addition, the brightness ratio of the two components is changing on timescales of several months to a year (Beck et al. 2004).

T Tau N and S probably contribute about equally to the mid-infrared flux, even though the southern components could be brighter especially at the longer wavelengths (see Ghez et al. 1991). The IRS spectrum of the T Tau system is the only spectrum in our sample of T Tauri stars that shows a 10- $\mu\text{m}$  absorption feature. Since it was observed before that the northern component likely has a 10- $\mu\text{m}$  emission feature, while the southern component displays a silicate absorption feature at 10  $\mu\text{m}$  (Ghez et al. 1991; Van Cleve et al. 1994), the fact that we observe a 10- $\mu\text{m}$  absorption feature in the

spectrum of the T Tau system suggests that T Tau S is the brighter source already at 10  $\mu\text{m}$  and is indeed surrounded by an envelope.

### 3.3.8. *FP Tau, V836 Tau, VY Tau, ZZ Tau*

These four objects were classified as Class III objects in KH95. However, our IRS spectra clearly show that they are Class II objects; their SEDs show excess above photospheric flux levels roughly starting at the L-band (3.5  $\mu\text{m}$ ) – V836 Tau, whose L-band flux is likely erroneous, already has some excess at K (2.2  $\mu\text{m}$ ) – and their SED slopes are shallower than expected for Class III objects. The lack of near-IR excess emission in FP Tau, VY Tau, and ZZ Tau could be explained by cleared-out inner disk regions and/or very low mass accretion rates. In fact, the spectrum of ZZ Tau is reminiscent of the spectrum of St 34 (Hartmann et al. 2005b), where a spectroscopic binary caused partial clearing of the inner disk regions, and dust growth and settling are likely responsible for weak silicate features and low dust continuum levels. ZZ Tau is also a close binary, with a separation of only  $0''.04$  between the two components. Like St 34, it has little excess emission below about 8  $\mu\text{m}$ , but it does have a prominent silicate feature with a narrow peak at about 9.2  $\mu\text{m}$ , most likely due to silica (see, e.g., Bowey & Adamson 2002).

The dust excess of VY Tau is particularly interesting. Herbig (1977) emphasized that VY Tau has had a remarkable history of outbursts, varying in photographic magnitude from a lower base of  $m_{pg} \sim 14$  up to  $\sim 10$  or brighter, on timescales of a year or less. These intermittent, highly-irregular outbursts may then plausibly be attributed to events of accretion from a disk, possibly mostly cleared in its inner regions. This object should be monitored more extensively for further insights into its behavior.

## 3.4. *Morphological Sequence*

We arranged the IRS spectra of our 85 Class II objects into a morphological sequence according to the shape of their SED and the strength of their 10- and 20- $\mu\text{m}$  silicate features (see Figures 3 to 9). In each figure the spectra are ordered so that objects with stronger silicate features are at the top and objects with a steeper SED and weaker silicate feature are at the bottom; however, this sequence is not strictly followed to prevent overlaps of spectra in the figures. In addition, the spectra in figures 8 and 9 should be considered as “outliers”, whose peculiar IRS spectra cannot easily be assigned to any group of our sequence. To avoid erroneous reddening corrections due to uncertain extinctions  $A_V$ , which could result in more pronounced 10- $\mu\text{m}$  features for large values of  $A_V$ , figures 3 to 9 show the IRS spectra without any reddening correction. Since few T Tauri stars in our sample have large extinctions, most spectra show the actual shape of the SED in this wavelength range even without reddening correction.

Our first group of objects (Fig. 3), group A, shows pronounced silicate features and a flat or somewhat decreasing SED beyond about 20  $\mu\text{m}$ . The next group (Fig. 4), group B, is very similar to group A but has somewhat weaker silicate features. Group C (Fig. 5) is also characterized by more or less prominent silicate features, but it has clearly decreasing SEDs beyond 18  $\mu\text{m}$ . Among these objects, DH Tau has a somewhat peculiar SED: the slope

of its spectrum between 5 and 8  $\mu\text{m}$  and between 20 and 35  $\mu\text{m}$  matches that of the other spectra in this group, while there is a steep increase in flux between 14 and 20  $\mu\text{m}$ . Also, its silicate feature is relatively wide and shows substructure characteristic of crystalline silicates (see Sargent et al. 2006).

The spectra in groups A, B, and C display a large variety in their silicate feature, which does not seem to be correlated with the slope of the spectrum. Some 10- $\mu\text{m}$  features are smooth and narrow, indicating amorphous silicates (e.g., UY Aur), while other silicate features are wider and show distinct peaks, which is a sign of grain growth and the presence of crystalline silicates (e.g., DK Tau).

The fourth group (Fig. 6), group D, is characterized by a weak 10  $\mu\text{m}$  feature and an overall negative SED slope over the IRS range. Many weak silicate features are relatively square and wide and show characteristic peaks of crystalline silicates; trends between the relative strengths of crystalline and amorphous silicates and the FWHM of the silicate feature will be explored by D. M. Watson et al. (2006, in preparation). In some spectra of group D, the 20- $\mu\text{m}$  silicate feature is somewhat more prominent than the feature at shorter wavelengths. This trend becomes more pronounced in our group E (Fig. 7), where almost no discernible 10- $\mu\text{m}$  feature is left in the spectrum (F04570+2520 being the exception), and the SED is decreasing steeply.

Figures 8 and 9 show spectra that are not part of our morphological sequence. The spectra in figure 8 display an overall rising SED over the IRS spectral range and prominent 10- $\mu\text{m}$  emission features. V892 Tau, F04101+3103, and SU Aur are of earlier spectral types than most of the Class II objects in our sample and, as opposed to T Tauri stars of spectral type later than G1, have prominent PAH features in their spectra. CoKu Tau/4, DM Tau, and GM Aur are so-called transitional disks (Rice et al. 2003; Forrest et al. 2004; Quillen et al. 2004; D’Alessio et al. 2005; Calvet et al. 2005), characterized by a lack or decrease of excess emission shortward of about 8  $\mu\text{m}$  due to inner disk clearings and a steep SED beyond 13  $\mu\text{m}$ . UX Tau A would seem like a transitional disk due to its steep increase in flux at about 13  $\mu\text{m}$ , but it has a substantial excess above photospheric flux levels beyond 2  $\mu\text{m}$  and only a very weak 10- $\mu\text{m}$  silicate emission feature. As mentioned in section 3.3, UX Tau is a quadruple system, but the A component is likely the dominating source; some disk evolution has likely occurred in this system.

Figure 9 shows a few sources with roughly flat SEDs from 5 to 35  $\mu\text{m}$ , as well as the spectrum of CZ Tau, whose SED is peculiar, unlike those of any other object in our sample (see section 3.3). The flat-spectrum sources in this figure are objects associated with Herbig-Haro jets and nebulosities in their surroundings (White & Hillenbrand 2004; Krist et al. 1998, and references therein). These objects are probably in transition between Class I and II stage, when their envelopes have not fully dissipated yet. These “young” T Tauri stars include, for example, DG Tau, T Tau, and XZ Tau.

The mid-IR excess emission from Class II objects can be divided into optically thin emission from sub-micron sized dust grains in the flared disk surface layer (i.e., the upper layers of the disk atmosphere), whose most prominent signature is the silicate emission feature at 10  $\mu\text{m}$ , and a continuum component, which originates from deeper, optically thick layers of the disk atmosphere. As disks evolve in time, dust grains grow and settle towards the midplane (Weidenschilling 1997; Dullemond & Dominik 2004); the upper disk layers close to the star (within a few AU) are depleted on a very short timescale, much less than the  $\sim 10$  Myr lifetime of a protoplanetary disk (Dullemond & Dominik 2004), with larger grains settling faster than the small grains. The larger grains around the midplane of the disk generate more emission at mm wavelengths, while the depletion of small grains in the upper disk layers causes a decrease in the continuum emission from the mid- to the far-IR, but these small grains still generate an emission band at 10  $\mu\text{m}$ . Therefore, the effects of dust settling, and thus the extent of disk evolution, can be seen clearly at mid-IR wavelengths (Miyake & Nakagawa 1995; Furlan et al. 2005b; D’Alessio et al. 2006).

However, the idea of dust evolving from small grains to larger grains and eventually to planetesimals over the course of a few Myr is probably too simplistic: recently, Dullemond & Dominik (2005) found that dust growth by coagulation occurs on very short timescales (less than  $\sim 1$  Myr, the typical age of a T Tauri star) in their simulations, and argued that small grains must therefore be replenished to produce the observed infrared excess. If grain growth and fragmentation both occur at the same time, grain sizes cannot be used to infer the evolutionary state of a disk, i.e. the presence of large grains in disks does not necessarily mean that a disk is older and thus more evolved.

Over the last several years, it has become increasingly clear that disk models with dust settling are needed to explain the observed SEDs of T Tauri stars: maximum grain sizes and dust-to-gas mass ratios are different for the disk interior and the disk surface, with larger grains ( $\lesssim 1$  mm) close to the midplane and small, ISM-like dust in the disk surface layer. To quantify the amount of dust settling, we use a variable,  $\epsilon$ , which is the ratio of the dust-to-gas mass ratio in the disk atmosphere and the standard dust-to-gas mass ratio of the interstellar medium (1:100) (D’Alessio et al. 2006). A value of  $\epsilon=1$  means that no settling has taken place, while a small value of  $\epsilon$  indicates the presence of larger grains towards the midplane of the disk and fewer small grains in the upper layers.

The morphological sequence from group A to E could be partly understood in terms of disk evolution: as dust grows, the 10- $\mu\text{m}$  silicate feature becomes wider and flatter (Przygodda et al. 2003), and as it settles, the mid-IR excess decreases, causing a steeper negative slope of the mid-IR part of the SED (D’Alessio et al. 2006). Due to small dust grains still present in the disk atmosphere, the 10- $\mu\text{m}$  feature can still be strong relative to the continuum; it is more pronounced than the 20- $\mu\text{m}$  feature due to the wavelength-dependent emissivity of the dust. A decrease in the 10- to 20- $\mu\text{m}$  flux ratio could indicate a decrease of emission from inner disk regions relative to the outer parts, since the 10- $\mu\text{m}$  emission arises

#### 4. ANALYSIS

##### 4.1. Dust Growth and Settling

mostly from inner regions of the disk, while the main 20- $\mu\text{m}$  emission region lies further out. Given that dust growth and settling is fastest in the inner parts of the disk (Hayashi et al. 1985; Weidenschilling 1997), it is expected that the silicate emission from the inner disk would decrease first. A more detailed, quantitative study, which is beyond the scope of this paper, is required to tie our morphological sequence to disk evolution; here, we tentatively suggest that dust has grown and settled to a larger extent in the disks of groups D and E than in groups A, B, and C.

#### 4.2. Settled Disk Models

To analyze our Class II objects in a more quantitative way, we compare them to a grid of accretion disk models that include dust settling (D’Alessio et al. 2006). The vertical disk structure is derived self-consistently, as in D’Alessio et al. (1998, 1999, 2001); the resulting flared disk extends from the dust sublimation radius to an outer radius of 300 AU, which was set arbitrarily, but does not affect the shape of the mid-infrared spectrum. At the inner disk edge, the “wall”, light from the star is incident parallel to the surface normal. The disk is heated by viscous dissipation and stellar irradiation. The central source is a typical T Tauri star in Taurus:  $T=4070$  K,  $R=1.864 R_{\odot}$ ,  $M=0.8 M_{\odot}$ ,  $L=0.79 L_{\odot}$ .

Silicates and graphite make up the dust grains in the disk (optical constants from Draine & Lee 1984); their sizes range from 0.005 to 0.25  $\mu\text{m}$  in the upper disk layers (i.e., similar to the interstellar medium), while in the lower disk layers, the maximum grain size is set at 1 mm. The dust particles follow a size distribution of the form  $n(a)da = a^{-3.5}da$  between the minimum and maximum grain sizes. Models with either isotropic scattering of the incident radiation by dust grains or perfect forward scattering were considered, with the true case lying in between the two limiting cases. The value of  $\epsilon$  was also varied; to include the effect of both dust settling and grain growth, a higher depletion of small grains in the upper layers is accompanied by an increase of large grains in the lower disk layers. Thus, while the dust is depleted in the disk atmosphere, the amount of dust is increased in the layers around the midplane, conserving the total amount of dust. The models of the grid vary in accretion rate ( $10^{-8}$  and  $10^{-9} M_{\odot} \text{ yr}^{-1}$ ), inclination angle along the line of sight ( $75^{\circ}5$ ,  $60^{\circ}$ ,  $50^{\circ}$ ,  $40^{\circ}$ ,  $30^{\circ}$ ,  $20^{\circ}$ , and  $11^{\circ}5$ ), amount of dust settling ( $\epsilon = 1, 0.1, 0.01, \text{ and } 0.001$ ), and dust composition. As we did in Furlan et al. (2005b), we use the spectral coverage of the IRS combined with models to estimate the degree of dust settling.

### 4.3. Spectral Indices

#### 4.3.1. Definition

To characterize the SEDs of the T Tauri stars in our sample, we computed spectral indices at different wavelengths in the IRS spectral range that represent continuum emission, similar to our analysis in Furlan et al. (2005b). We integrated the flux of our dereddened spectra in the following wave bands: 5.4–6.0  $\mu\text{m}$  (center wavelength,  $\lambda_c$ , at 5.7  $\mu\text{m}$ ), 12.5–14.0  $\mu\text{m}$  ( $\lambda_c = 13.25 \mu\text{m}$ ), and 23.5–26.5  $\mu\text{m}$  ( $\lambda_c = 25 \mu\text{m}$ ). Then we divided the result by the width of the respective wave band, which yielded a flux density in wavelength units ( $F_{\lambda}$ ) for each

band. To obtain spectral indices,  $n$ , we computed

$$n = \log \left( \frac{\lambda_2 F_{\lambda_2}}{\lambda_1 F_{\lambda_1}} \right) / \log \left( \frac{\lambda_2}{\lambda_1} \right),$$

first between 5.7 and 13.25  $\mu\text{m}$  ( $n_{6-13}$ ), then between 13.25 and 25  $\mu\text{m}$  ( $n_{13-25}$ ).

Furthermore, to quantify the properties of our morphological sequence, we used our IRS spectra not corrected for reddening and calculated a spectral index covering most of the IRS spectral range, from 6 to 25  $\mu\text{m}$  ( $n_{6-25}$ ), and estimated the strength of the 10- $\mu\text{m}$  silicate feature. For the latter, we interpolated the continuum from data between 5.0 and 7.5  $\mu\text{m}$  and between 13.0 and 16.0  $\mu\text{m}$  with a third-order polynomial, subtracted it from the silicate feature defined between 8.0 and 12.4  $\mu\text{m}$ , integrated the flux of the continuum-subtracted silicate feature, and normalized it to the continuum integrated over the same wavelength range. Due to uncertainties in the continuum fit, this procedure might not always yield accurate measurements of the 10- $\mu\text{m}$  silicate feature strength, but for the majority of objects it will result in reasonable estimates.

#### 4.3.2. Results: IRS Data

Figure 10 displays the continuum-subtracted, integrated flux of the 10- $\mu\text{m}$  feature, normalized to the continuum, versus the  $n_{6-25}$  spectral index. The data points belonging to spectra from groups A to E of our morphological sequence are identified by different plotting symbols; the data for the plot can be found in Table 4. As indicated by our morphological sequence, objects with the smallest values of  $n_{6-25}$  in our sample ( $n_{6-25} < -1.0$ ) have weak 10- $\mu\text{m}$  silicate features. The spectra of groups D and E have the smallest 10- $\mu\text{m}$  feature strengths, but SED slopes in the range of those of group C, which has stronger silicate features. Only objects with  $n_{6-25} > -0.5$  have very strong features, but for these values of the spectral index there is a large spread in silicate feature strength.

Figure 11 shows a plot of  $n_{13-25}$  versus  $n_{6-13}$ , computed using the IRS spectra of the Class II and III objects in our sample (*open diamonds and crossed squares, respectively*), and for two extremes, a flat, passive disk and a naked photosphere; the data for the plot are also given in Table 5. A photosphere in the mid-IR has a spectral index of  $-3$  (Rayleigh-Jeans limit), while a geometrically thin, optically thick disk has an index of  $-4/3$ . Due to some spectrophotometric uncertainty in our IRS data, the typical error bars for the spectral indices are about  $\pm 0.05$ . The dashed boxes delineate outliers and will be discussed below.

As noted in Furlan et al. (2005b), the fact the Class II objects in Fig. 11 have spectral indices that are larger than the value expected for a flat, optically thick disk means that their disks must be flared. Only one object in our sample, F04570+2520, has an  $n_{13-25}$  spectral index that is slightly smaller than that of a flat, optically thick disk; its SED shows only a weak 10- $\mu\text{m}$  silicate feature and a steep decrease in flux beyond it, probably indicating an evolved disk in which a large fraction of the dust has grown and settled. For most objects, the  $n_{6-13}$  and  $n_{13-25}$  spectral indices seem to be correlated; a steeper slope of the spectrum between 6 and 13  $\mu\text{m}$  is

usually accompanied by a steeper slope from 13 to 25  $\mu\text{m}$ . As can be seen from the frequency distribution of both indices in Figure 12, the distribution peaks at values between  $-1.5$  and  $0$  for  $n_{6-13}$ , and between  $-1$  and  $0.5$  for  $n_{13-25}$ . While negative spectral slopes larger than  $\sim -1$  prevail for both wavelength ranges, which is typical for Class II objects, the slope measured between 13 and 25  $\mu\text{m}$  tends to be flatter than the one measured between 6 and 13  $\mu\text{m}$ .

In addition, there is a small number of objects with spectral indices  $n_{13-25}$  larger than about 0.5, which is represented by the seemingly randomly scattered points at positive  $n_{13-25}$  values in Figure 11, and framed by dotted boxes in the figure. These “outliers” can be divided up into three groupings: the 6 objects in the lower left box, the 4 objects in the right box, and the 4 objects in the uppermost box.

The first-mentioned grouping contains DH Tau, LkCa 15, AB Aur, HK Tau, Haro 6-13, and SU Aur. These Class II objects are characterized by a steep rise in slope starting at 13  $\mu\text{m}$ , indicating a strong 20- $\mu\text{m}$  silicate feature, and a relatively flat SED past 20  $\mu\text{m}$ . The right box frames F04101+3103, MHO 3, V892 Tau, and, at a negative  $n_{13-25}$  value, CZ Tau. These objects also have a strong 20- $\mu\text{m}$  silicate feature, in addition to a pronounced 10- $\mu\text{m}$  emission feature, but their SEDs decrease past 20  $\mu\text{m}$ . Also, their emission from 5 to 8  $\mu\text{m}$  is lower than the emission at longer wavelengths, resulting in a positive index  $n_{6-13}$ . The decrease of the SED beyond about 20  $\mu\text{m}$  is especially dramatic for CZ Tau, which explains the low value of  $n_{13-25}$  of this object. As mentioned earlier, CZ Tau’s outer disk might be truncated, resulting in a substantial decrease of its far-IR flux.

The final grouping includes the known transitional disks in Taurus, CoKu Tau/4, GM Aur, and DM Tau, as well as UX Tau A at  $n_{6-13} \sim -2$ . These “outliers” have negative spectral indices from 6 to 13  $\mu\text{m}$  and positive spectral indices from 13 to 25  $\mu\text{m}$ , the latter due to a steep increase in flux at about 13  $\mu\text{m}$ .

Also included in Figure 11 are the spectral indices  $n_{13-25}$  versus  $n_{6-13}$  for those Class III objects in our sample whose 25  $\mu\text{m}$  flux was detected. However, in many cases the 25- $\mu\text{m}$  flux is very weak and the LL spectrum noisy, resulting in a larger uncertainty for the index calculation. Nevertheless, most of the indices of our Class III objects are close to values of  $-3$ , as expected for close-to-photospheric fluxes. One object, V410 Tau, which was not included in the plot, lies at spectral indices smaller than  $-3$ , which is mainly a result of its very noisy LL spectrum; its IRS spectrum seems to follow the slope of a photosphere, with a possible slight excess. V410 X-ray 3 lies at  $n_{13-25} = -1.6$  and  $n_{6-13} = -2.9$ ; HBC 427 and V819 Tau, which have an apparent infrared excess in LL, can be found at  $n_{13-25} = -0.7$  and  $n_{6-13} = -2.8$  and  $-2.6$ , respectively. If at least part of their infrared excess is real, the latter three objects would constitute the transition phase between Class II and Class III, which seems to be very rapid due to the lack of objects with spectral indices between  $-1$  and  $-2$ . This result is similar to what is found when the K–L colors are plotted versus the K–N colors (see, e.g., Kenyon & Hartmann 1995): there is a continuous transition between Class I and II objects, with the latter displaying bluer IR colors, but a gap between the Class II sources with the small-

est infrared excess and the Class III sources, which have almost photospheric colors.

#### 4.3.3. Results: IRS Data and Models

We computed analogous spectral indices ( $n_{13-25}$  vs.  $n_{6-13}$ ) for the grid of accretion disk models and overplotted the results from IRS data and disk models in Figure 13. We show indices computed from two sets of disk models, one with isotropic scattering of the incident stellar radiation by dust grains and the other with perfect forward scattering (which has the same effect as no scattering, i.e. albedo=0); they represent the two limiting cases of scattering. There is only a slight difference between these two sets; spectral indices are not very sensitive to the degree of scattering in the models. Each model set contains models computed with two mass accretion rates,  $10^{-8}$  and  $10^{-9}$   $M_{\odot} \text{ yr}^{-1}$ , which are typical for T Tauri stars in Taurus (see, e.g. Gullbring et al. 1998; Hartmann et al. 1998).

The spread in the  $n_{6-13}$  index is partly due to different accretion rates, but mostly an effect of varying inclination angles. This can be understood in terms of the wall emission, which dominates the flux at wavelengths shortward of about 6  $\mu\text{m}$ ; the wall emission increases as the inclination angle increases, resulting in a larger increase of the 6- $\mu\text{m}$  flux than of the 13- $\mu\text{m}$  flux, while the disk emission, which dominates at 25  $\mu\text{m}$ , decreases (D’Alessio et al. 2006). The different extents of dust settling in the models, which are described by  $\epsilon$ , cause a spread in both  $n_{6-13}$  and  $n_{13-25}$ . Since for mass accretion rates of  $10^{-8}$  and  $10^{-9}$   $M_{\odot} \text{ yr}^{-1}$  irradiation heating represents the main heating source (D’Alessio et al. 1999, 2006), more settling causes a decrease in the mid-IR continuum emission; the disk intercepts less radiation from the central star if its outer parts are less flared. This affects the 25- $\mu\text{m}$  flux more than the flux at shorter wavelengths, resulting in smaller spectral indices (i.e., steeper SED slopes) for smaller  $\epsilon$ .

For example, AA Tau, which has a mass accretion rate of  $6.5 \times 10^{-9}$   $M_{\odot} \text{ yr}^{-1}$  (White & Ghez 2001), lies at  $n_{6-13} = -0.87$  and  $n_{13-25} = -0.37$ , which is close to the model with an accretion rate of  $10^{-8}$   $M_{\odot} \text{ yr}^{-1}$ ,  $\epsilon = 0.001$ , and inclination angle of  $50^{\circ}$ . Bouvier et al. (1999) derived a lower limit for the inclination angle of AA Tau of  $53^{\circ}$ , but favored  $i = 75^{\circ}$  to explain the peculiar variability of this object. Our comparison would suggest a somewhat lower inclination angle, and in addition a large amount of settling in the disk of AA Tau. As another example, BP Tau, which has an inclination angle of  $39^{\circ}$  (Muzerolle et al. 2003b) and a mass accretion rate of  $1.3 \times 10^{-8}$   $M_{\odot} \text{ yr}^{-1}$  (White & Ghez 2001) lies at  $n_{6-13} = -0.67$  and  $n_{13-25} = -0.24$ , which is in between the model points for  $\dot{M} = 10^{-8}$   $M_{\odot} \text{ yr}^{-1}$ ,  $\epsilon = 0.001$ , and inclination angles of  $30^{\circ}$  and  $40^{\circ}$ , respectively.

Most Class II objects can be described with models that include substantial settling, with an  $\epsilon$  between 0.01 and 0.001, which means dust depletions of factors of 100 to 1000 in the upper layers. The spectral indices for accretion disks with  $\epsilon < 1$  are lower than for those in which no settling has taken place, since the reduced mid-IR continuum causes a steeper slope, towards the value of  $-4/3$  of a flat, optically thick disk. The settling of dust does not affect the silicate emission features, which we see in virtually all of our Class II spectra; these features are

generated by the small grains still present in the upper hot layers of the disk atmosphere. As indicated earlier with a smaller sample of CTTSs (Furlan et al. 2005b), we conclude with this larger sample of CTTSs and WTTSs that the majority of T Tauri stars have disks in which dust has started to grow and settle towards the mid-plane, thus affecting the SEDs of these young (1–2 Myr) pre-main-sequence stars. This is consistent with the simulations of Dullemond & Dominik (2005), which predict dust growth on timescales of  $\sim 1$  million years or less.

Given that all of our T Tauri stars are at about the same age, the difference in the spectra of various objects must be due to different initial conditions and different circumstellar environments influenced, for example, by the presence of close companions. Thus, the extent to dust settling in a disk, at least in its initial stages, might be less a function of age and more related to the object’s formation history and current environment.

We caution that the comparison of our data with a grid of accretion disk models is valid to gauge trends in our data, but that additional parameters, in particular the composition of the dust, need adjustments before any detailed interpretations can be carried out reliably. For example, choosing glassy pyroxene or olivine instead of “astronomical” silicates and graphite will generate different dust emission, both in the continuum and in the emission bands, and different spectral indices will result. Therefore, the detailed composition of the dust adds additional scatter to the spectral indices plot, which has to be considered in addition to the effects of inclination and dust settling. The values we derived for  $\epsilon$  should thus be treated as rough estimates only. The effect of dust composition on the models, as well as models of individual objects, will be presented in a future paper (P. D’Alessio et al. 2006, in preparation).

#### 4.4. Taurus Median

In order to determine a typical SED range for T Tauri stars in Taurus, we computed a median SED from 1.25 to 34  $\mu\text{m}$  using the 2MASS J, H, and  $K_s$  photometry and the IRS spectra of all our 85 Class II objects, dereddened using the  $A_V$  values listed in Table 2. To obtain a clearer representation of the flux values in the IRS spectral range, we integrated the IRS spectra over narrow wave bands and divided by the width of the band, creating the equivalent of narrowband photometric measurements at 5.7, 7.1, 8.0, 9.2, 9.8, 11.3, 12.3, 13.25, 16.25, 18.0, 21.0, 25.0, 30.0, and 34.0  $\mu\text{m}$ . The width of the bands ranged from 0.6  $\mu\text{m}$  at the shorter wavelengths to 3  $\mu\text{m}$  at the longer wavelengths; the width of the silicate bands, centered at 9.8 and 18  $\mu\text{m}$ , was chosen to be 2  $\mu\text{m}$ . As in D’Alessio et al. (1999), we normalized all flux values at H (1.65  $\mu\text{m}$ ) before computing median values, since, for most objects, the H-band flux is photospheric, and thus normalization at H is equivalent to normalizing to the stellar luminosity. Since for most of the T Tauri stars in our sample mass accretion rates are low enough ( $\lesssim 10^{-7} M_\odot \text{ yr}^{-1}$ ) that the star is the main heating source of the disk, the infrared excess of the disk should scale with stellar luminosity. By computing the median values, we also obtained the quartiles, which define the range around the median where 50% of all flux values lie.

Figure 14 shows our median with the quartiles (in-

dicated by the error bars) and that obtained by D’Alessio et al. (1999). We computed the median using all 85 Class II objects in our sample (*upper, green data points*), and by including only stars with spectral types between K5 and M2 (*lower, red data points*). The latter data set constitutes a more homogeneous sample of stars with similar effective temperatures and allows a more direct comparison to the median from D’Alessio et al. (1999); it is also given in table 6.

With the IRS data, we are able to resolve the silicate emission features at 10 and 20  $\mu\text{m}$ ; the median SED clearly shows that most objects have pronounced silicate emission and thus small grains in the hot upper layers of the disk atmospheres. It is remarkable that our median SED at 25  $\mu\text{m}$  almost coincides with the one from D’Alessio et al. (1999), who used *IRAS* 25  $\mu\text{m}$  flux measurements. The median SED for K5–M2 stars is lower than the one for all Class II objects in our sample, as expected for a sample of stars that excludes earlier, and thus hotter, spectral types. In particular, the decrease in the 13–25  $\mu\text{m}$  range is more pronounced than that at shorter wavelengths, indicating that the silicate feature at 20  $\mu\text{m}$  decreases more than the 10- $\mu\text{m}$  silicate feature for late spectral types.

Figure 15 displays the IRS median SED for spectral types K5–M2 (*red*), the median computed from IRAC data (Hartmann et al. 2005a, *purple*), and the photospheric component (*dotted line*), represented by the SED of the WTTS HBC 427 (Hartmann et al. 2005a). We compare these to SEDs of two irradiated accretion disk models with different degrees of dust settling. The photospheric component is normalized at J, while all the other SEDs are normalized at H.

The models shown in figure 15 were constructed according to the methods of D’Alessio et al. (2006) and are described in section 4.2, with a few differences: accretion shock irradiation is included as heating mechanism for the disk (but it does not make a significant difference for  $\dot{M} \lesssim 10^{-8} M_\odot \text{ yr}^{-1}$ ), and the dust mixture consists of spherical particles of amorphous pyroxene (glassy  $\text{Mg}_{0.7}\text{Fe}_{0.3}\text{SiO}_3$ , optical constants from Dorschner et al. 1995) and graphite (optical constants from Draine & Lee 1984). This dust composition results in higher silicate emission at 10 and 20  $\mu\text{m}$  and therefore is a better fit for the Taurus median SED (see also discussion in § 4.3.3). The models were computed for an inclination angle of 60°, a mass accretion rate of  $3 \times 10^{-8} M_\odot \text{ yr}^{-1}$ , and two values of the settling parameter  $\epsilon$ , 0.1 and 0.001. Comparison of the models with the median and quartiles suggests large degrees of depletion in the upper layers of disks in Taurus: about 50% of the disks have a dust depletion larger than a factor of 1000 ( $\epsilon \leq 0.001$ ), while about 25% of the disks can be characterized with degrees of depletion between a factor of 10 and 1000. Only about 25% of the disks have between a factor of 10 and no depletion of dust in the upper disk layers.

#### 4.5. Class III Objects: Upper Limits for Disk Masses

We estimated upper limits for the mass of small, warm dust grains (size  $\lesssim 10 \mu\text{m}$ , temperature  $\gtrsim 100 \text{ K}$ ) in the disks around the 26 Class III objects we observed, assuming optically thin dust emission from “astronomical” silicates (optical constants from Draine & Lee 1984). Since none of the Class III objects considered here show sili-

cate emission bands at 10 or 20  $\mu\text{m}$ , larger grains ( $\gtrsim 3\text{--}4\ \mu\text{m}$ ), if any, must be present in their disks; for this reason we included only grains between sizes of 3 and 10  $\mu\text{m}$  (the mid-infrared is not sensitive to emission from larger particles). First, we calculated the equilibrium temperature for each grain size at a distance  $r$  from the star by solving the following equation numerically:

$$\left(\frac{R_*}{r}\right)^2 \int_0^\infty Q_{abs}(\nu) B_\nu(T_*) d\nu = 4 \int_0^\infty Q_{abs}(\nu) B_\nu(T_d) d\nu, \quad (1)$$

where  $R_*$  is the stellar radius,  $Q_{abs}$  is the absorption efficiency, and  $B_\nu(T)$  is the Planck function, evaluated at the stellar effective temperature  $T_*$  and at the dust grain temperature  $T_d$ , respectively. Assuming that the disk is axially symmetric and geometrically thin, we parametrized the optical depth as

$$\tau(r, a) = \Sigma_0(r_0) \left(\frac{r}{r_0}\right)^{-\gamma} \left(\frac{a}{a_0}\right)^{-3.5} \pi a^2 Q_{abs}(a, \nu), \quad (2)$$

where  $\Sigma_0(r_0)$  is the reference surface number density of dust grains of size  $a_0$  at a distance  $r_0$  from the star; this column density varies with radius as  $r^{-\gamma}$ , and the grain size distribution varies as  $a^{-3.5}$ . We chose  $r_0 = 1\ \text{AU}$ ,  $a_0 = 1\ \mu\text{m}$ , and, besides for a few exceptions,  $\gamma = 1$ . The flux emitted from the disk at each wavelength is obtained by integrating over annuli and summing over each dust grain size:

$$F_\lambda = \sum_{a_i} \left( \frac{1}{D^2} \int_{r_{in}}^{r_{out}} 2\pi r \tau(r, a_i) B_\nu(T_d(r, a_i)) dr \right), \quad (3)$$

where  $\tau(r, a_i)$  is defined in equation (2),  $T_d(r, a_i)$  is obtained from equation (1), and  $D$  is the distance to the star, assumed to be 140 pc, the distance to the Taurus star-forming region. The total dust mass in the disk is given by

$$M_d = \sum_{a_i} m_d \int_{r_{in}}^{r_{out}} 2\pi r \Sigma(r) dr, \quad (4)$$

where  $m_d$  is the mass of a single dust grain. To obtain upper limits for the dust masses in our Class III objects, we adjusted the parameter  $\Sigma_0(r_0)$  (and in some cases also  $\gamma$ ), until the disk emission from equation (3) matched the emission of each Class III object after photosphere subtraction. The photospheres are represented by AMES-dusty models of Allard et al. (2001) for effective temperatures up to 5000 K; for hotter stars, we approximated the photospheres by blackbodies in the Rayleigh-Jeans limit. We integrated the flux from 0.1 to 50 AU and summed over 11 grain sizes from 3 to 10  $\mu\text{m}$  radius.

With all the assumptions mentioned above, our model fits result in typical upper limits for warm, small dust grains in any circumstellar disks around our Class III objects of a few times  $10^{-4}$  lunar masses. Assuming that the infrared excess of HBC 427 and V819 Tau can be fully attributed to disks around these objects, the maximum amount of dust mass in these disks would amount to a few times  $10^{-3}$  lunar masses. In addition, since their excess starts rather abruptly at 14  $\mu\text{m}$ , their disks would require inner holes of a few AU in size to explain the lack of shorter-wavelength excess emission. HP Tau/G2 seems to already have a slight excess shortward of 14  $\mu\text{m}$ ;

again assuming all the excess emission originates in a disk around this object, the upper limit to the dust mass would amount to somewhat less than  $10^{-4}$  lunar masses. A dust mass of a few times  $10^{-4}$  lunar masses is comparable to that found around debris disks (Habing et al. 2001), although closer to the lower mass values.

## 5. DISCUSSION

The multi-wavelength SEDs, which weight the spectrum in terms of the relative power emitted at each wavelength, provide an immediate initial estimate of the relative luminosities of the star and the disk. In most cases, the luminosity of the disk is less than that of the star because most of the disk heating and thus disk emission are due to absorption and reprocessing of stellar radiation. However, of the 85 Class II systems shown in Figure 1, XZ Tau, UY Aur, HN Tau, FS Tau, 04187+1927, 04200+2759, DG Tau, and DP Tau appear to have anomalously large IRS excesses relative to the central star. As noted in section 3.3, a few of these objects have envelopes; UY Aur has an IR companion separated by  $0''.9$  from the primary and likely seen through the disk of the primary, given its larger reddening (Hartigan & Kenyon 2003). Together with the other  $\sim 9$  objects with very high and therefore uncertain  $A_V$  mentioned in section 3.3, there might be about 17 candidates for edge-on disks. In addition, HK Tau B (Stapelfeldt et al. 1998) and likely also AA Tau (Ménard et al. 2003; Bouvier et al. 2003) have edge-on disks, bringing the total of T Tauri stars likely seen at an inclination angle close to  $90^\circ$  to 19. Thus, 22% of the Class II objects in our sample (or 17% of the T Tauri stars of our Taurus sample) are likely seen edge-on, which is roughly what is expected from statistical considerations for objects with inclinations between  $77^\circ$  and  $90^\circ$ . In addition, these objects do not show any deep silicate absorption features, as expected from models (D'Alessio et al. 1999); therefore, either these highly inclined disks are not massive enough, or we are observing the 10- $\mu\text{m}$  thermal emission from the inner disk, scattered by the dust in the outer disk atmosphere (see McCabe, Duchêne, & Ghez 2003).

A few of our Class II objects show a decrease or lack of IR excess at shorter IRS wavelengths, indicative of inner disk clearings or gaps. Some of these sources (GM Aur, DM Tau, CoKu Tau/4) have been described as transition disks and are the subject of other papers (D'Alessio et al. 2006; Calvet et al. 2005). Only 4% of the Class II objects in our sample, or 3% of the 111 T Tauri stars we observed in Taurus, are in this transitional disk phase, which would indicate that this stage is short-lived.

If their longer-wavelength excess proves to be real, HBC 427, V819 Tau, and possibly also V410 X-ray 3, could also be considered as objects in transition, even though their excess emission is so weak that it is probably not optically thick disk emission. On the other hand, they might be regarded as debris disks, where dust is generated by collisions of larger bodies and is optically thin at all wavelengths. If that were the case, they would be among the youngest debris disks discovered so far.

UX Tau A has a very peculiar spectrum, with significant excess at shorter wavelengths, but a sharp transition at 20  $\mu\text{m}$ . Even though it is a multiple system, the other components are at distances that are unlikely to affect

the inner disk we are observing with the IRS. Also, their flux contribution in the mid-IR is expected to be small. Thus, the IRS spectrum of UX Tau A suggests that it might be in a pre-transition state, when most dust in the inner disk has already settled and grown, and thus the lifetime of the inner disk is coming to an end.

Other objects that could be in a pre-transition state are 04385+2550, Haro 6-13, HK Tau, and LkCa 15; their 20- $\mu\text{m}$  silicate feature is stronger or comparable to the 10- $\mu\text{m}$  feature, reminiscent of transitional disks, but they have substantial excess emission in the near-IR. In these objects, a gap might be opening, but a significant inner disk is still present.

## 6. CONCLUSIONS

We presented the mid-infrared spectra of 85 Class II and 26 Class III objects in Taurus, obtained with the Infrared Spectrograph on board the *Spitzer Space Telescope*. This large sample of pre-main-sequence stars of similar age, belonging to the same star-forming region, allows us to draw the following conclusions about circumstellar disk evolution:

- All CTTSs and some WTTs display mid-IR excesses, which are generated in the inner (a few tenths to a few AU) parts of circumstellar disks. Accretion signatures like the H $\alpha$  equivalent line width do not necessarily indicate the presence or absence of disks, but they usually reveal whether the innermost disk regions are still present. While accreting T Tauri stars have dusty disks extending from the dust sublimation radius outward and thus generate excess emission starting at near-IR wavelengths, WTTs often have inner disk holes and thus lack near-IR excess emission. Since there are few WTTs with disks, the transition period between an active (i.e., accreting) and a passive (i.e., purely reprocessing) disk stage seems short-lived.

- The details of the mid-IR excess, and thus the distribution and properties of the dust in circumstellar disks, do not seem to be correlated with the multiplicity of the young star system. A sub-arcsecond ( $\lesssim 140$  AU at the distance of Taurus) companion does not necessarily influence the inner disk; even spectroscopic binaries, like DQ Tau, seem to have substantial inner disks. We note that our IRS spectra cannot separate the contribution of close multiple systems, and therefore, in some cases, they show the combined mid-IR spectrum of circumprimary, circumsecondary, and circumbinary disk. The mid-IR spectra of multiple systems do not have any peculiarities that would set them apart from single stars; this could be explained if most disks in these systems are not influenced by the presence of companions and either the circumprimary disk clearly dominates the system or all components have similar disks, or if a circumbinary disk mimicked the behavior of a circumstellar disk around a single star.

- Almost all Class II objects show 10- and 20- $\mu\text{m}$  silicate emission features in their mid-IR spectra, generated in the optically thin disk surface layer. There is a wide variety of feature strengths and crystallinity, independent of the spectral type and multiplicity of the objects. However, objects with weak 10- $\mu\text{m}$  silicate features usually have a decreasing SED in the mid-IR range, which could be an indication of dust growth and settling. In objects where the 10- and 20- $\mu\text{m}$  features are suppressed,

dust grains must exceed radii of about 4  $\mu\text{m}$ .

- After comparing the spectral indices  $d\log(\lambda F_\lambda)/d\log(\lambda)$  between 6 and 13  $\mu\text{m}$  and between 13 and 25  $\mu\text{m}$  of our Class II objects with accretion disk models that include dust settling, we infer that our data are consistent with these models. Within the assumptions of the adopted models, most T Tauri stars seem to have experienced substantial dust settling (and likely also dust growth), with depletions of factors of about 100–1000 of the standard dust-to-gas mass ratio in the disk atmosphere. Thus, we are able to estimate the amount of dust settling for a large sample of T Tauri stars, using the high sensitivity and spectral coverage of the IRS. This result will aid in the refinement of models predicting the evolution of dust in protoplanetary disks.

- Most WTTs in our sample are Class III objects, which have nearly photospheric fluxes in the infrared, indicating a dispersal of dust in their circumstellar disks. The upper limit for the mass of small, warm dust grains in these disks lies around  $10^{-4}$  lunar masses, which is similar to the dust mass of low-mass debris disks. In some cases nearby companions ( $\sim 10''$ ), which seem to have an infrared excess, contaminated the LL part of our Class III sources. It is interesting that objects of roughly the same age, formed in close proximity to each other, do evolve on different time scales. This result, as well as the diversity in mid-IR spectra observed for our Class II objects, indicates that age does not seem to be the dominating factor determining disk evolution, but rather the initial conditions of the star-forming core, like its mass and angular momentum.

While there likely is an evolutionary sequence from a classical T Tauri star with an accretion disk to a weak-lined T Tauri star with a passive disk to a T Tauri star with little or no disk left, there does not seem to be an absolute, evolutionary timescale regulating when the transitions from one stage to the next occur. Therefore, we can witness circumstellar disk evolution in young star-forming regions such as Taurus and infer the major steps in the process by analyzing a large sample of pre-main-sequence stars; this paper is a contribution to this effort by presenting and analyzing unprecedented data from the *Spitzer Space Telescope*.

We thank our anonymous referee for helpful comments and suggestions. This work is based on observations made with the *Spitzer Space Telescope*, which is operated by the Jet Propulsion Laboratory, California Institute of Technology, under NASA contract 1407. Support for this work was provided by NASA through contract number 1257184 issued by JPL/Caltech. N.C. and L.H. acknowledge support from NASA grants NAG5-13210 and NAG5-9670, and STScI grant AR-09524.01-A. P.D. acknowledges grants from PAPIIT, UNAM and CONACyT, México. This publication makes use of data products from the Two Micron All Sky Survey, which is a joint project of the University of Massachusetts and the Infrared Processing and Analysis Center/California Institute of Technology, funded by the National Aeronautics and Space Administration and the National Science Foundation. It has also made use of the SIMBAD and VizieR databases, operated at CDS (Strasbourg, France), NASA's Astrophysics Data System Ab-

stract Service, and of the NASA/ IPAC Infrared Science Archive operated by JPL, California Institute of Tech-

nology (Caltech), under contract with NASA.

## REFERENCES

- Acke, B., & van den Ancker, M. E. 2004, *A&A*, 426, 151
- Adams, F. C., Lada, Ch. J., & Shu, F. H. 1987, *ApJ*, 312, 788
- Allard, F., Hauschildt, P. H., Alexander, D. R., Tamanai, A., Schweitzer, A. 2001, *ApJ*, 556, 357
- Artymowicz, P., & Lubow, S. H. 1994, *ApJ*, 421, 651
- Beck, T. L., Schaefer, G. H., Simon, M., Prato, L., Stoesz, J. A., & Howell, R. R. 2004, *ApJ*, 614, 235
- Beckwith, S. V. W., Sargent, A. I., Chini, R. S., & Güsten, R. 1990, *AJ*, 99, 924
- Beichman, C. A., Boulanger, F., & Moshir, M. 1992, *ApJ*, 386, 248
- Bertout, C., Robichon, N., & Arenou, F. 1999, *A&A*, 352, 574
- Bouvier, J., Chelli, A., Allain, S., Carrasco, L., Costero, R., Cruz-Gonzalez, I., Dougados, C., Fernández, M., et al. 1999, *A&A*, 349, 619
- Bouvier, J., Grankin, K. N., Alencar, S. H. P., Dougados, C., Fernández, M., Basri, G., Batalha, C., Guenther, E., et al. 2003, *A&A*, 409, 169
- Bowey, J. E., & Adamson, A. J. 2002, *MNRAS*, 334, 94
- Briceño, C., Hartmann, L., & Stauffer, J. 1998, *AJ*, 115, 2074
- Calvet, N., Hartmann, L., Kenyon, S. J., & Whitney, B. A. 1994, *ApJ*, 434, 330
- Calvet, N., Muzerolle, J., Briceño, C., Hernández, J., Hartmann, L., Saucedo, J. L., & Gordon, K. D. 2004, *AJ*, 128, 1294
- Calvet, N., D'Alessio, P., Watson, D. M., Franco-Hernández, R., Furlan, E., Green, J., Sutter, P. M., Forrest, W. J., et al. 2005, *ApJ*, 630, L185
- Cohen, M., Megeath, S. T., Hammersley, P. L., Martín-Luis, F., & Stauffer, J. 2003, *AJ*, 125, 2645
- D'Alessio, P., Cantó, J., Calvet, N., & Lizano, S. 1998, *ApJ*, 500, 411
- D'Alessio, P., Calvet, N., Hartmann, L., Lizano, S., & Cantó, J. 1999, *ApJ*, 527, 893
- D'Alessio, P., Calvet, N., & Hartmann, L. 2001, *ApJ*, 553
- D'Alessio, P., Hartmann, L., Calvet, N., Franco-Hernández, R., Forrest, W. J., Sargent, B., Furlan, E., Uchida, K., et al. 2005, *ApJ*, 621, 461
- D'Alessio, P., Calvet, N., Hartmann, L., Franco-Hernández, R., & Servin, H. 2006, *ApJ*, 638, 314
- DeWarf, L. E., Sepinsky, J. F., Guinan, E. F., Ribas, I., & Nadalin, I. 2003, *ApJ*, 590, 357
- Dorschner, J., Begemann, B., Henning, Th., Jäger, C., & Mutschke, H. 1995, *A&A*, 300, 503
- Draine, B. T., & Lee, H. M. 1984, *ApJ*, 285, 89
- Duchêne, G. 1999, *A&A*, 341, 547
- Duchêne, G., Monin, J.-L., Bouvier, J., & Ménard, F. 1999, *A&A*, 351, 954
- Duchêne, G., Ghez, A. M., McCabe, C., & Weinberger, A. J. 2003, *ApJ*, 592, 288
- Duchêne, G., Bouvier, J., Bontemps, S., André, P., & Motte, F. 2004, *A&A*, 427, 651
- Dullemond, C. P., & Dominik, C. 2004, *A&A*, 421, 1075
- Dullemond, C. P., & Dominik, C. 2005, *A&A*, 434, 971
- Forrest, W. J., Sargent, B., Furlan, E., D'Alessio, P., Calvet, N., Hartmann, L., Uchida, K. I., Green, J. D., et al. 2004, *ApJS*, 154, 443
- Furlan, E., Calvet, N., D'Alessio, P., Hartmann, L., Forrest, W. J., Watson, D. M., Luhman, K. L., Uchida, K. I., et al. 2005a, *ApJ*, 621, L129
- Furlan, E., Calvet, N., D'Alessio, P., Hartmann, L., Forrest, W. J., Watson, D. M., Uchida, K. I., Sargent, B., et al. 2005b, *ApJ*, 628, L65
- Ghez, A. M., Neugebauer, G., Gorham, P. W., Haniff, C. A., Kulkarni, S. R., Matthews, K., Koresko, C., & Beckwith, S. 1991, *AJ*, 102, 2066
- Ghez, A. M., Neugebauer, G., & Matthews, K. 1993, *AJ*, 106, 2005
- Gullbring, E., Hartmann, L., Briceño, C., & Calvet, N. 1998, *ApJ*, 492, 323
- Gullbring, E., Calvet, N., Muzerolle, J., & Hartmann, L. 2000, *ApJ*, 544, 927
- Haas, M., Leinert, Ch., & Richichi, A. 1997, *A&A*, 326, 1076
- Habing, H. J., Dominik, C., Jourdain de Muizon, M., Laureijs, R. J., Kessler, M. F., Leech, K., Metcalfe, L., Salama, A., et al. 2001, *A&A*, 365, 545
- Hartigan, P., Strom, K. M., & Strom, S. E. 1994, *ApJ*, 427, 961
- Hartigan, P., & Kenyon, S. J. 2003, *ApJ*, 583, 334
- Hartmann, L., Calvet, N., Gullbring, E., & D'Alessio, P. 1998, *ApJ*, 495, 385
- Hartmann, L., Megeath, S. T., Allen, L., Luhman, K., Calvet, N., D'Alessio, P., Franco-Hernández, R., & Fazio, G. 2005a, *ApJ*, 629, 881
- Hartmann, L., Calvet, N., Watson, D. M., D'Alessio, P., Furlan, E., Sargent, B., Forrest, W. J., Uchida, K. I., et al. 2005b, *ApJ*, 628, L147
- Hayashi, C., Nakazawa, K., & Nakagawa, Y. 1985, *Protostars and Planets II*, 1100
- Herbig, G. H. 1977, *ApJ*, 217, 693
- Herbig, G. H., & Bell, K. R. 1988, *Lick Observatory Bulletin, Santa Cruz: Lick Observatory*, 1988
- Higdon, S. J. U., et al. 2004, *PASP*, 116, 975
- Houck, J. R., et al. 2004, *ApJS*, 154, 18
- Itoh, Y., Tamura, M., & Nakajima, T. 1999, *AJ*, 117, 1471
- Itoh, Y., Tamura, M., & Tokunaga, A. 2002, *PASJ*, 54, 561
- Iyengar, K. V. K., & Parthasarathy, M. 1997, *A&AS*, 121, 45
- Jayawardhana, R., Hartmann, L., Fazio, G., Fisher, R. S., Telesco, Ch. M., & Piña, R. K. 1999, *ApJ*, 521, L129
- Jensen, E. L. N., Koerner, D. W., & Mathieu, R. D. 1996, *AJ*, 111, 2431
- Kenyon, S. J., & Hartmann, L. 1987, *ApJ*, 323, 714
- Kenyon, S. J., Hartmann, L. W., Strom, K. M., & Strom, S. E. 1990, *AJ*, 99, 869
- Kenyon, S. J., Gomez, M., Marzke, R. O., & Hartmann, L. 1994a, *AJ*, 108, 251
- Kenyon, S. J., Dobrzycka, D., & Hartmann, L. 1994b, *AJ*, 108, 1872
- Kenyon, S. J., & Hartmann, L. 1995, *ApJS*, 101, 117 (KH95)
- Kenyon, S. J., Brown, D. I., Tout, Ch. A., & Berlind, P. 1998, *AJ*, 115, 2491
- Koresko, C. D., Herbst, T. M., & Leinert, Ch. 1997, *ApJ*, 480, 741
- Koresko, Ch. D. 2000, *ApJ*, 531, L147
- Krist, J. E., Stapelfeldt, K. R., Burrows, Ch. J., Ballester, G. E., Clarke, J. T., Crisp, D., Evans, R. W., Gallagher, J. S. III, et al. 1998, *ApJ*, 501, 841
- Krist, J. E., Stapelfeldt, K. R., & Watson, A. M. 2002, *ApJ*, 570, 785
- Lada, Ch. J., & Wilking, B. A. 1984, *ApJ*, 287, 610
- Lada, Ch. J. 1987, in *Star Forming Regions, proceedings of the IAU Symposium No. 115*, ed. M. Peimbert & J. Jugaku, Dordrecht:Reidel, 1
- Leinert, Ch., Zinnecker, H., Weitzel, N., Christou, J., Ridgway, S. T., Jameson, R., Haas, M., & Lenzen, R. 1993, *A&A*, 278, 129
- Leinert, Ch., Richichi, A., & Haas, M. 1997, *A&A*, 318, 472
- Luhman, K. L. 2004, *ApJ*, 617, 1216
- Martín, E. L., Rebolo, R., Magazzú, A., & Pavlenko, Ya. V. 1994, *A&A*, 282, 503
- Mathieu, R. D., Martin, E. L., & Magazzu, A. 1996, *BAAS*, 188, 60.05
- Mathieu, R. D., Stassun, K., Basri, G., Jensen, E. L. N., Johns-Krull, Ch., M., Valenti, J. A., Hartmann, L. W. 1997, *AJ*, 113, 1841
- Mathis, J. S. 1990, *ARA&A*, 28, 37
- McCabe, C., Duchêne, G., & Ghez, A. M. 2002, *ApJ*, 575, 974
- McCabe, C., Duchêne, G., & Ghez, A. M. 2003, *ApJ*, 588, L113
- Meeus, G., Waters, L. B. F. M., Bouwman, J., van den Ancker, M. E., Waelkens, C., & Malfait, K. 2001, *A&A*, 365, 476
- Ménard, F., Bouvier, J., Dougados, C., Mel'nikov, S. Y., & Grankin, K. N. 2003, *A&A*, 409, 163
- Meyer, M. R., Beckwith, S. V. W., Herbst, T. M., & Robberto, M. 1997, *ApJ*, 489, L173
- Miyake, K., & Nakagawa, Y. 1995, *ApJ*, 441, 361
- Monin, J.-L., Ménard, F., & Duchêne, G. 1998, *A&A*, 339, 113
- Motte, F., & André, P. 2001, *A&A*, 365, 440
- Mundt, R., Bührke, T., Fried, J. W., Neckel, T., Sarcander, M., & Stoeke, J. 1984, *A&A*, 140, 17
- Muzerolle, J., Hillenbrand, L., Calvet, N., Briceño, C., Hartmann, L. 2003a, *ApJ*, 592, 266

- Muzerolle, J., Calvet, N., Hartmann, L., & D'Alessio, P. 2003b, *ApJ*, 597, L149
- Muzerolle, J., Luhman, K. L., Briceño, C., Hartmann, L., & Calvet, N. 2005, *ApJ*, 625, 906
- Padgett, D. L., Brandner, W., Stapelfeldt, K. R., Strom, S. E., Terebey, S., & Koerner, D. 1999, *AJ*, 117, 1490
- Prato, L., & Simon, M. 1997, *ApJ*, 474, 455
- Przygodda, F., van Boekel, R., Àbrahàm, P., Melnikov, S. Y., Waters, L. B. F. M., & Leinert, Ch. 2003, *A&A*, 412, L43
- Quillen, A. C., Blackman, E. G., Frank, A., Varnière, P. 2004, *ApJ*, 612, L137
- Rice, W. K. M., Wood, K., Armitage, P. J., Whitney, B. A., & Bjorkman, J. E. 2003, *MNRAS*, 342, 79
- Richichi, A., Leinert, Ch., Jameson, R., & Zinnecker, H. 1994, *A&A*, 287, 145
- Sargent, B., Forrest W. J., D'Alessio, P., Li, A., Najita, J., Watson, D. M., Calvet, N., Furlan, E., et al. 2006, *ApJ*, in press
- Schaefer, G. H., Simon, M., Nelan, E., & Holfeltz, S. T. 2003, *AJ*, 126, 1971
- Simon, M., & Prato, L. 1995, *ApJ*, 450, 824
- Simon, M., Ghez, A. M., Leinert, Ch., Cassar, L., Chen, W. P., Howell, R. R., Jameson, R. F., Matthews, K., Neugebauer, G., & Richichi, A. 1995, *ApJ*, 443, 625
- Simon, M., Holfeltz, S. T., & Taff, L. G. 1996, *ApJ*, 469, 890
- Simon, M., Dutrey, A., & Guilloteau, S. 2000, *ApJ*, 545, 1034
- Sloan, G. C., Keller, L. D., Forrest, W. J., Leibensperger, E., Sargent, B., Li, A., Najita, J., Watson, D. M., et al. 2005, *ApJ*, 632, 956
- Smith, K. W., Balega, Y. Y., Duschl, W. J., Hofmann, K.-H., Lachaume, R., Preibisch, T., Schertl, D., & Weigelt, G. 2005, *A&A*, 431, 307
- Stapelfeldt, K. R., Krist, J. E., Ménard, F., Bouvier, J., Padgett, D. L., & Burrows, Ch., J. 1998, *ApJ*, 502, L65
- Steffen, A. T., Mathieu, R. D., Lattanzi, M. G., Latham, D. W., Mazeh, T., Prato, L., Simon, M., Zinnecker, H., & Loreggia, D. 2001, *AJ*, 122, 997
- Strom, K. M., & Strom, S. E. 1994, *ApJ*, 424, 237
- Uchida, K. I., Calvet, N., Hartmann, L., Kemper, F., Forrest, W. J., Watson, D. M., D'Alessio, P., Chen, C. H., et al. 2004, *ApJS*, 154, 439
- Van Cleve, J. E., Hayward, T. L., Miles, J. W., Gull, G. E., Schoenwald, J., & Houck, J. R. 1994, *Ap&SS*, 212, 231
- Weaver, W. B., & Jones, G. 1992, *ApJS*, 78, 239
- Weidenschilling, S. J. 1997, *Icarus*, 127, 290
- Werner, M. W. et al. 2004, *ApJS*, 154, 1
- White, R. J., Ghez, A. M., Reid, I. N., & Schultz, G. 1999, *ApJ*, 520, 811
- White, R. J., & Ghez, A. M. 2001, *ApJ*, 556, 265
- White, R. J., & Basri, G. 2003, *ApJ*, 582, 1109
- White, R. J., & Hillenbrand, L. A. 2004, *ApJ*, 616, 998
- White, R. J., & Hillenbrand, L. A. 2005, *ApJ*, 621, L65
- Wooden, D. H., Bell, K. R., Harker, D. E., & Woodward, C. E. 2000, *BAAS*, 197, 4707
- Young, C. H., Shirley, Y. L., Evans, N. J., Rawlings, J. M. C. 2003, *ApJS*, 145, 111

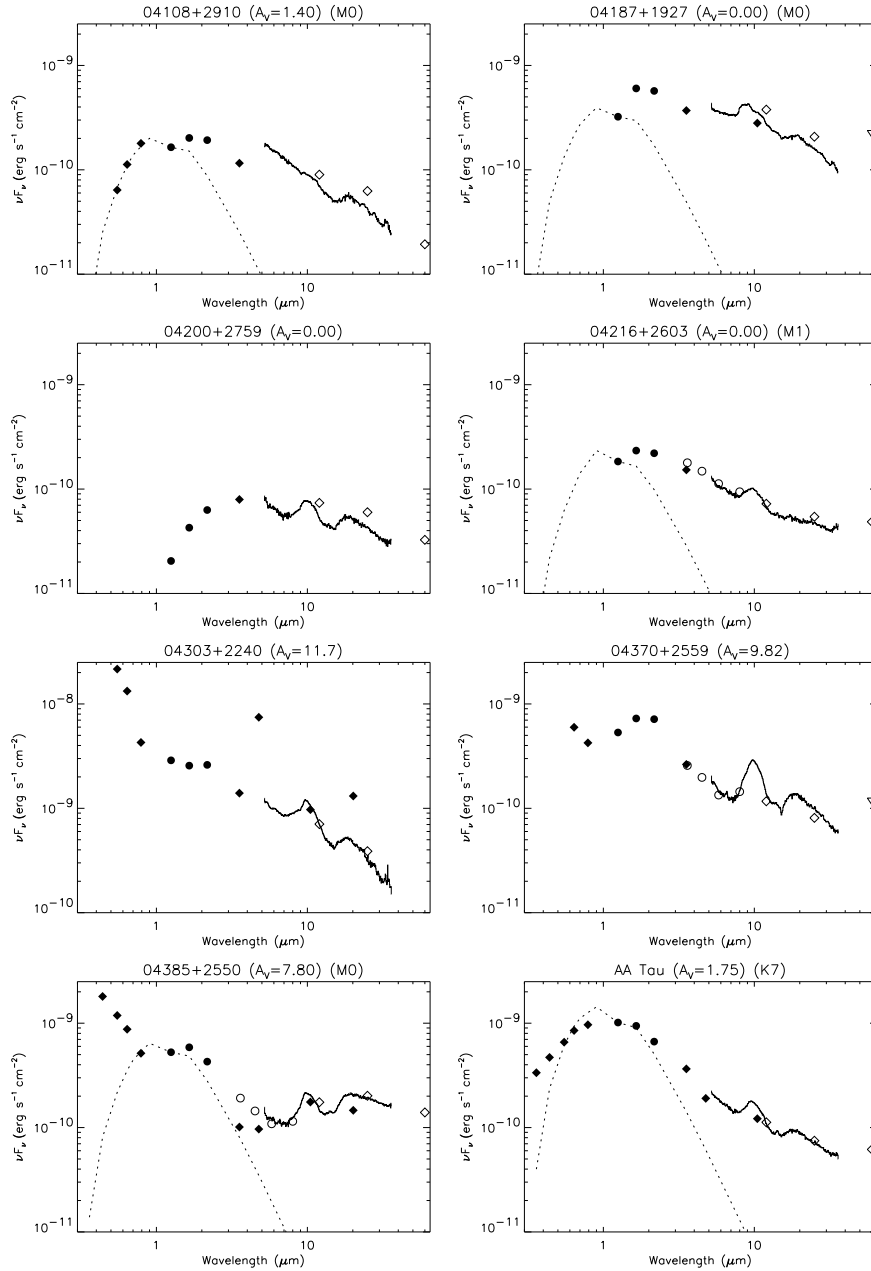


FIG. 1.— SED plots of the Class II objects in our sample, ordered alphabetically by their name. In addition to the IRS spectrum, we include optical to mid-IR, ground-based photometry (*filled diamonds*) mostly from KH95, the 2MASS  $J$ ,  $H$ , and  $K_s$  fluxes (*filled circles*), the IRAC 3.6, 4.5, 5.8, and 8.0  $\mu\text{m}$  fluxes (*open circles*) from Hartmann et al. (2005a), where available, and the *IRAS* 12, 25, and 60  $\mu\text{m}$  fluxes (*open diamonds*, or *open triangles* if upper limit) mostly from Weaver & Jones (1992). The photosphere is also sketched in for objects with known spectral type (see text for details). All fluxes, including the IRS spectrum, were dereddened using Mathis’s reddening law (Mathis 1990) and the extinctions listed in table 2.

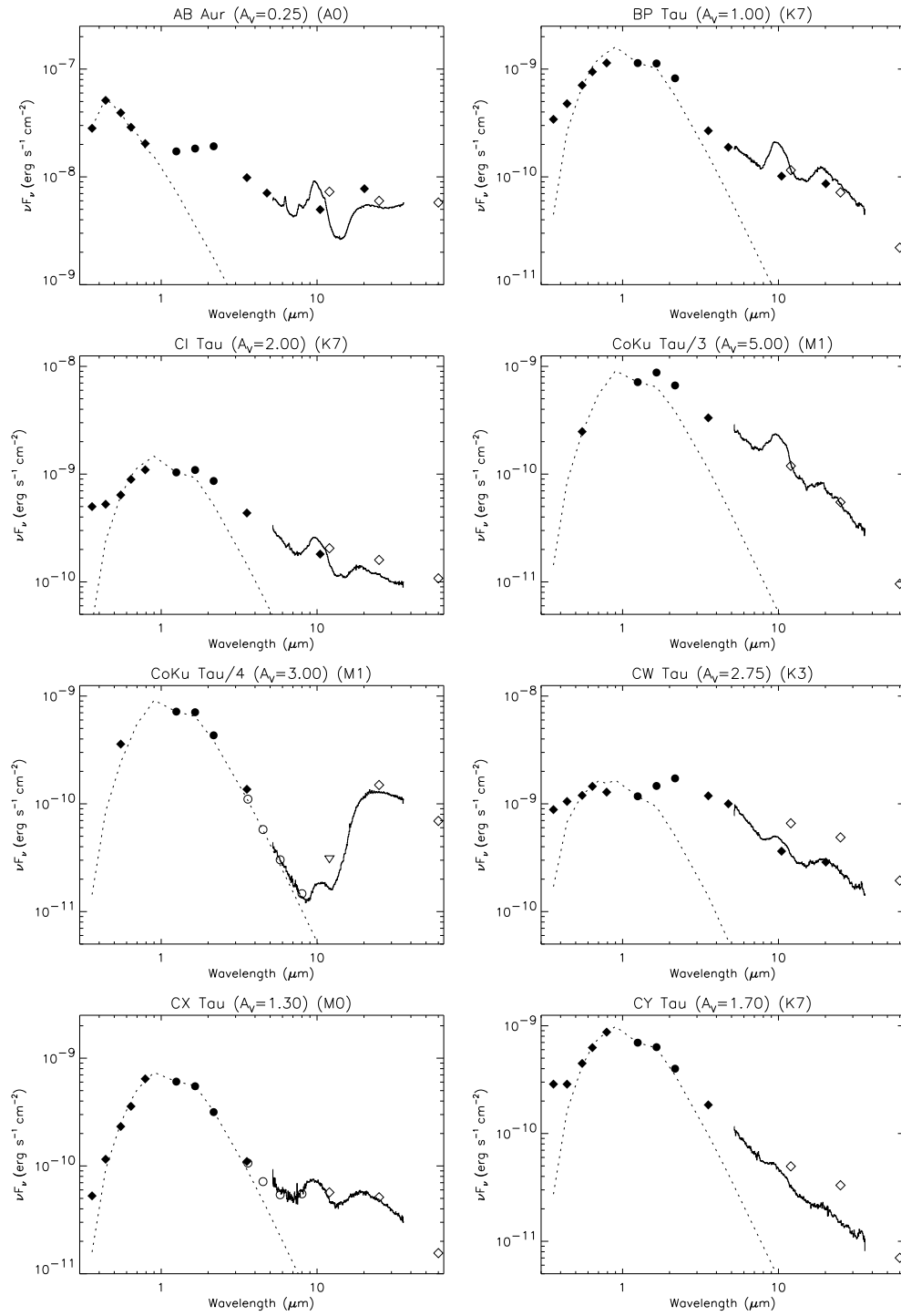


FIG. 1.— continued.

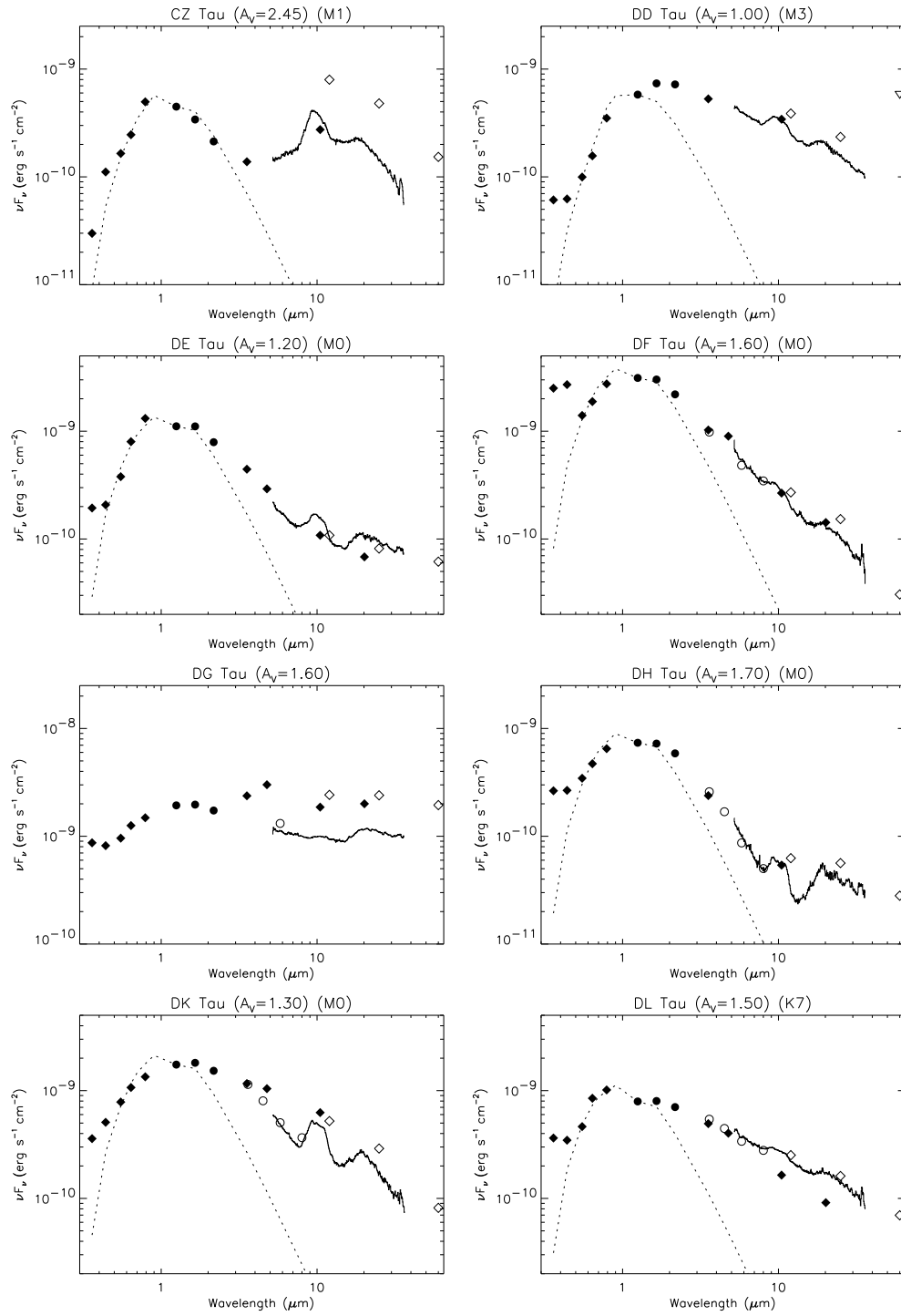


FIG. 1.— continued.

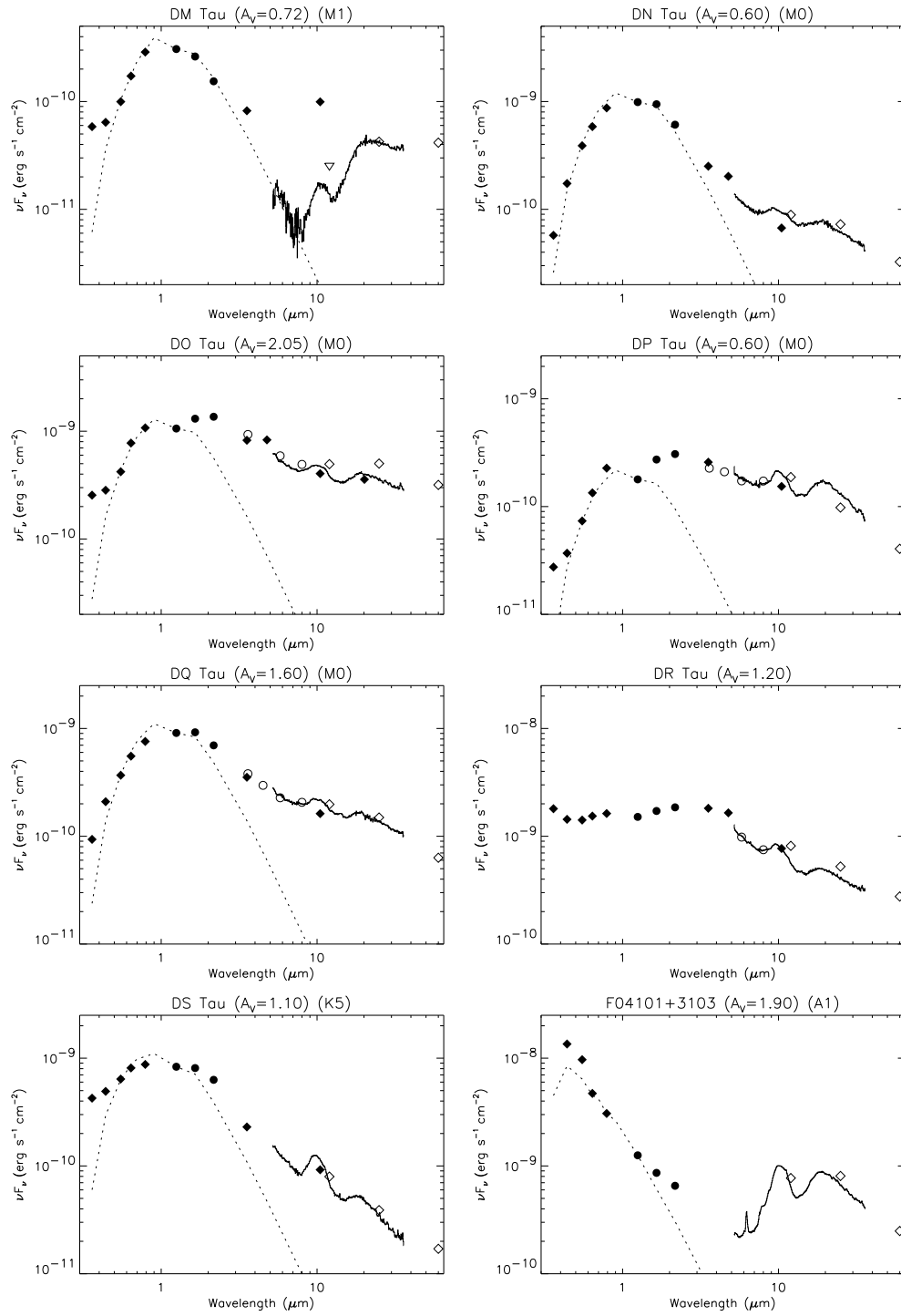


FIG. 1.— continued.

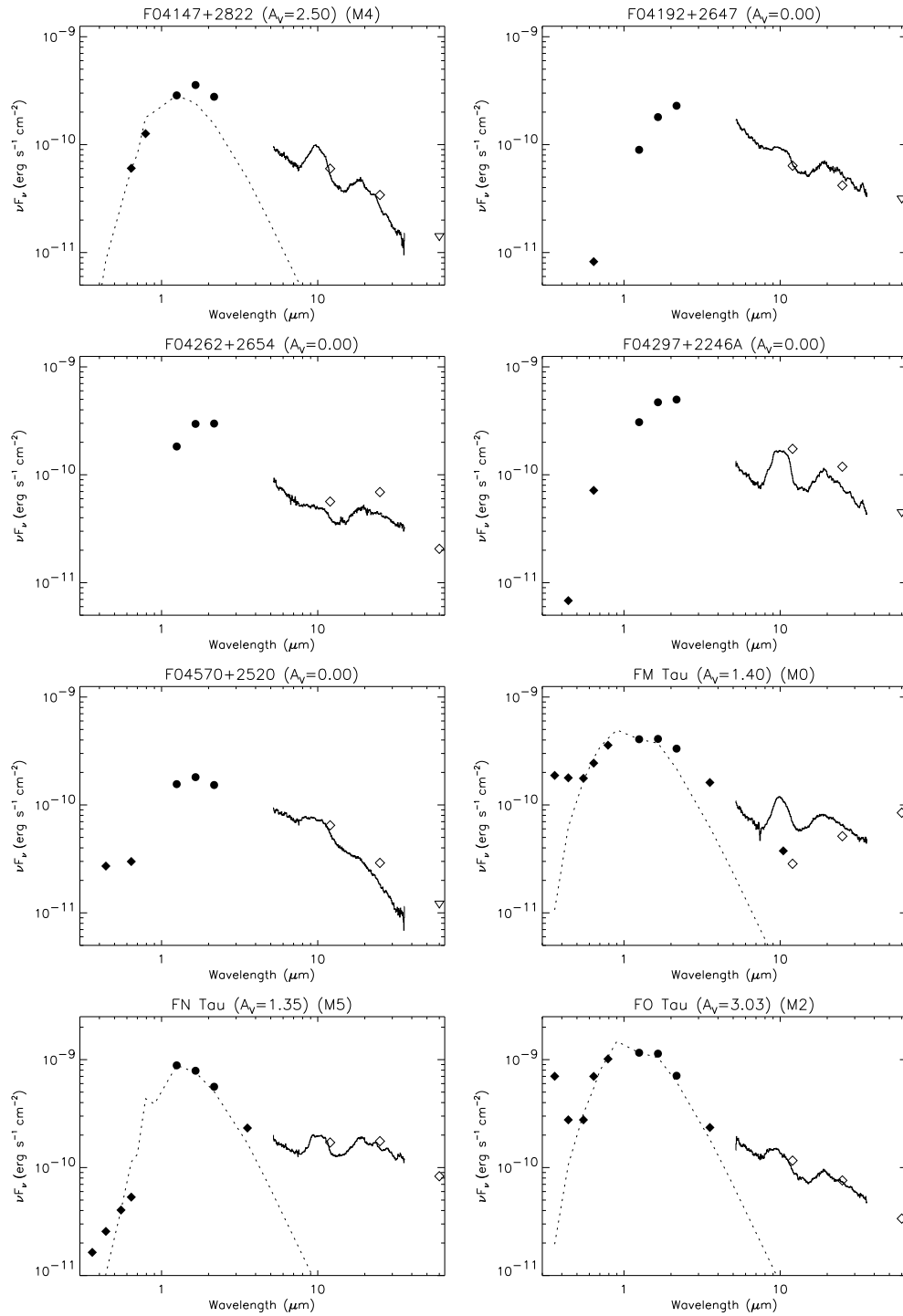


FIG. 1.— continued.

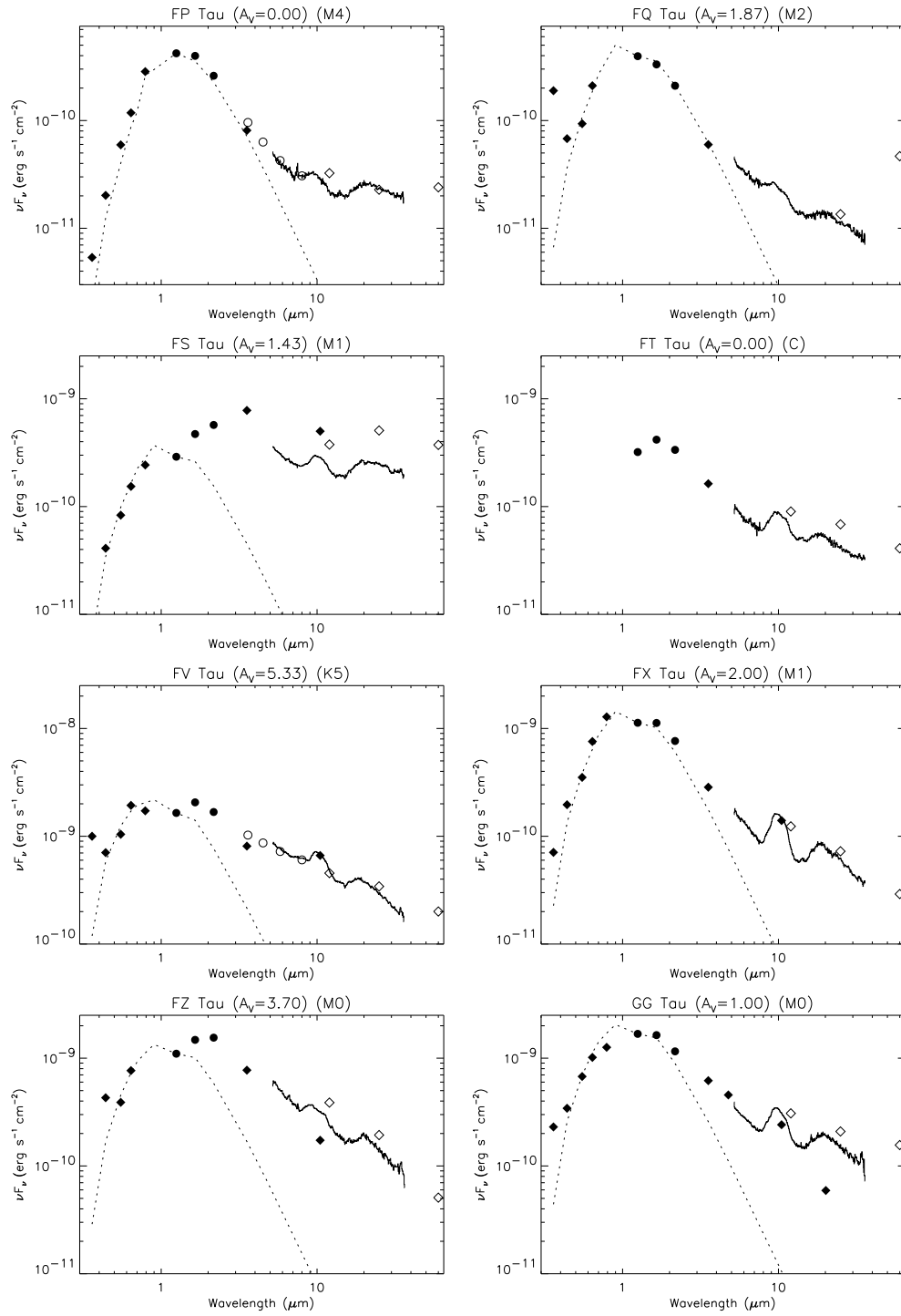


FIG. 1.— continued.

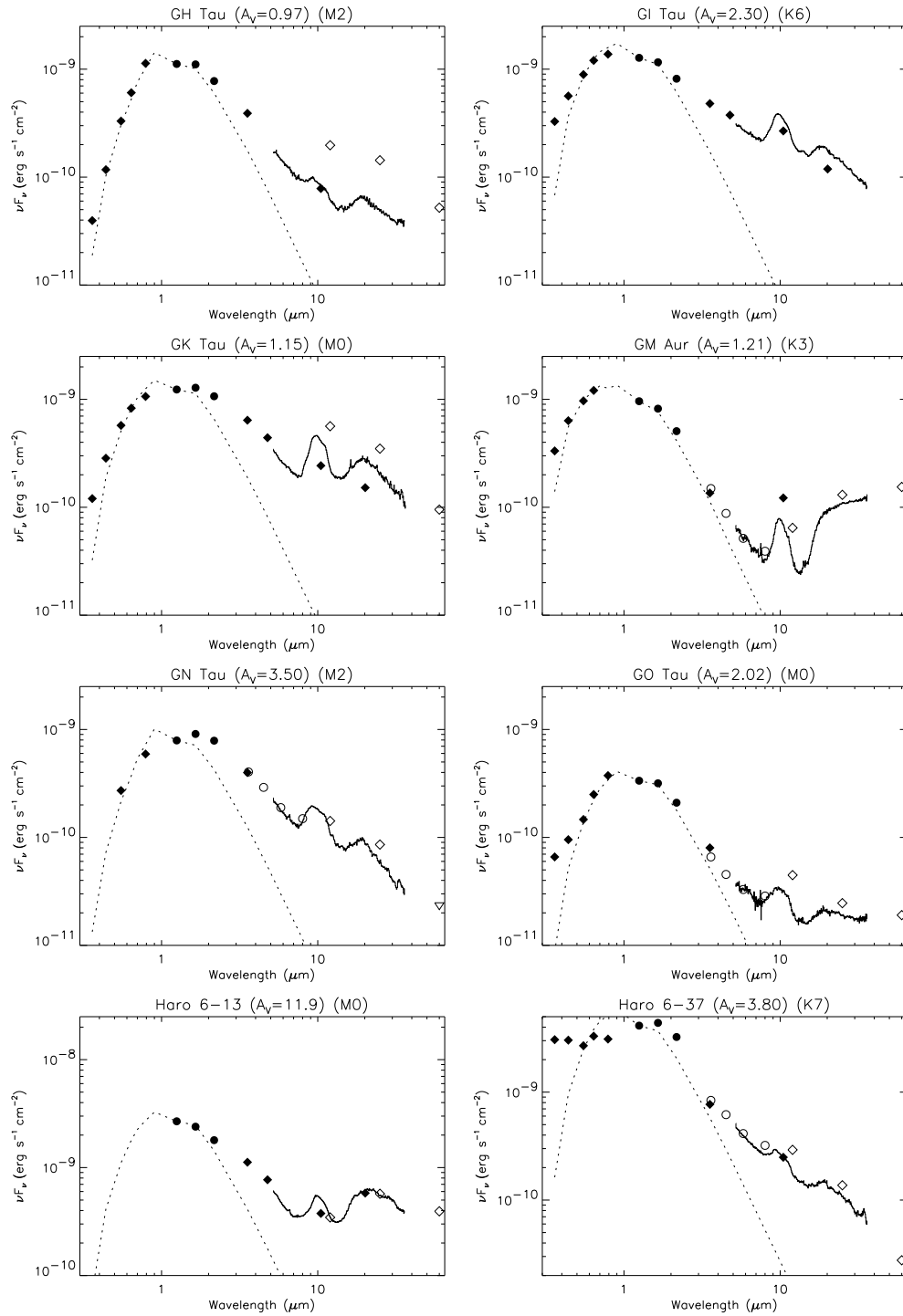


FIG. 1.— continued.

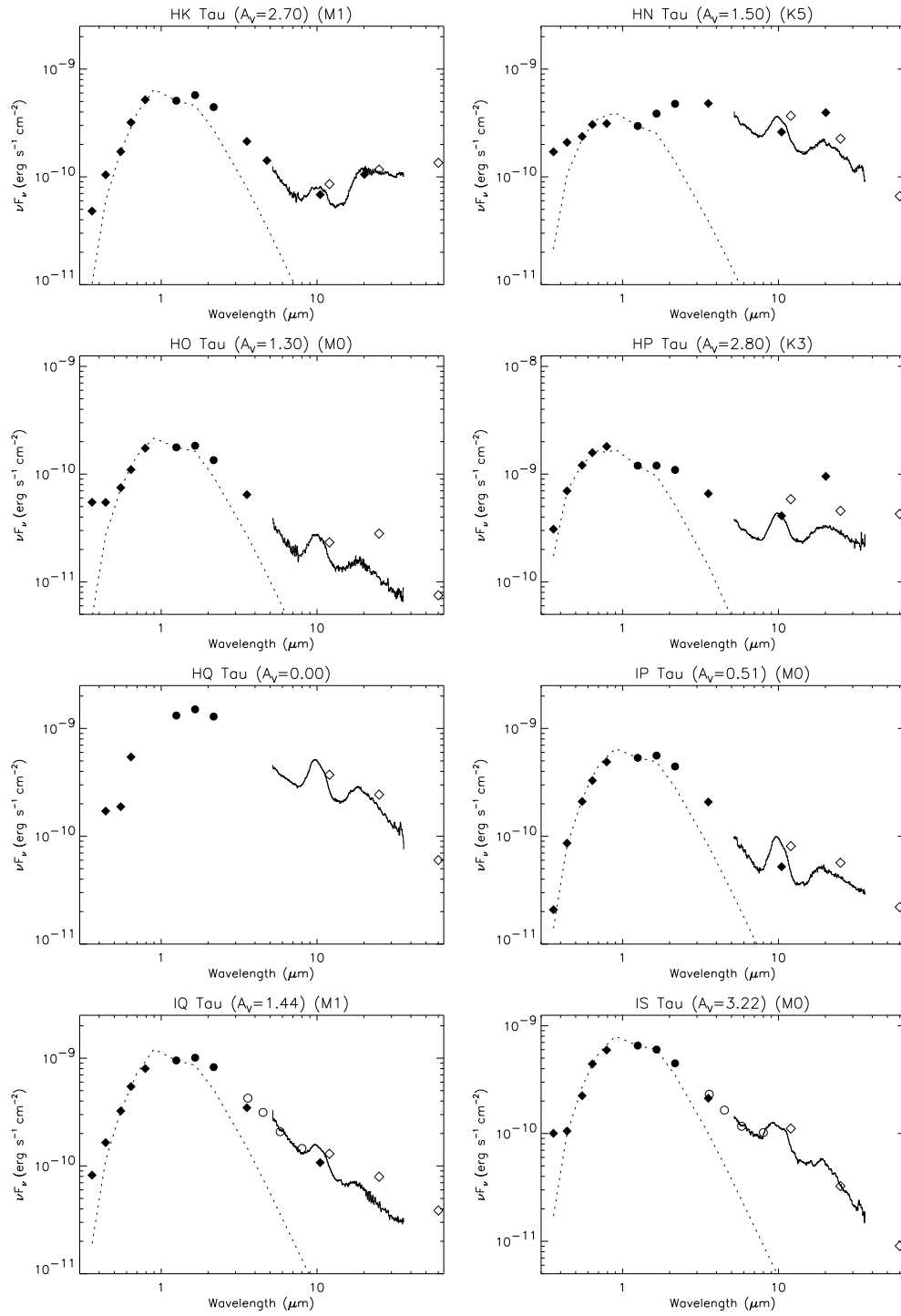


FIG. 1.— continued.

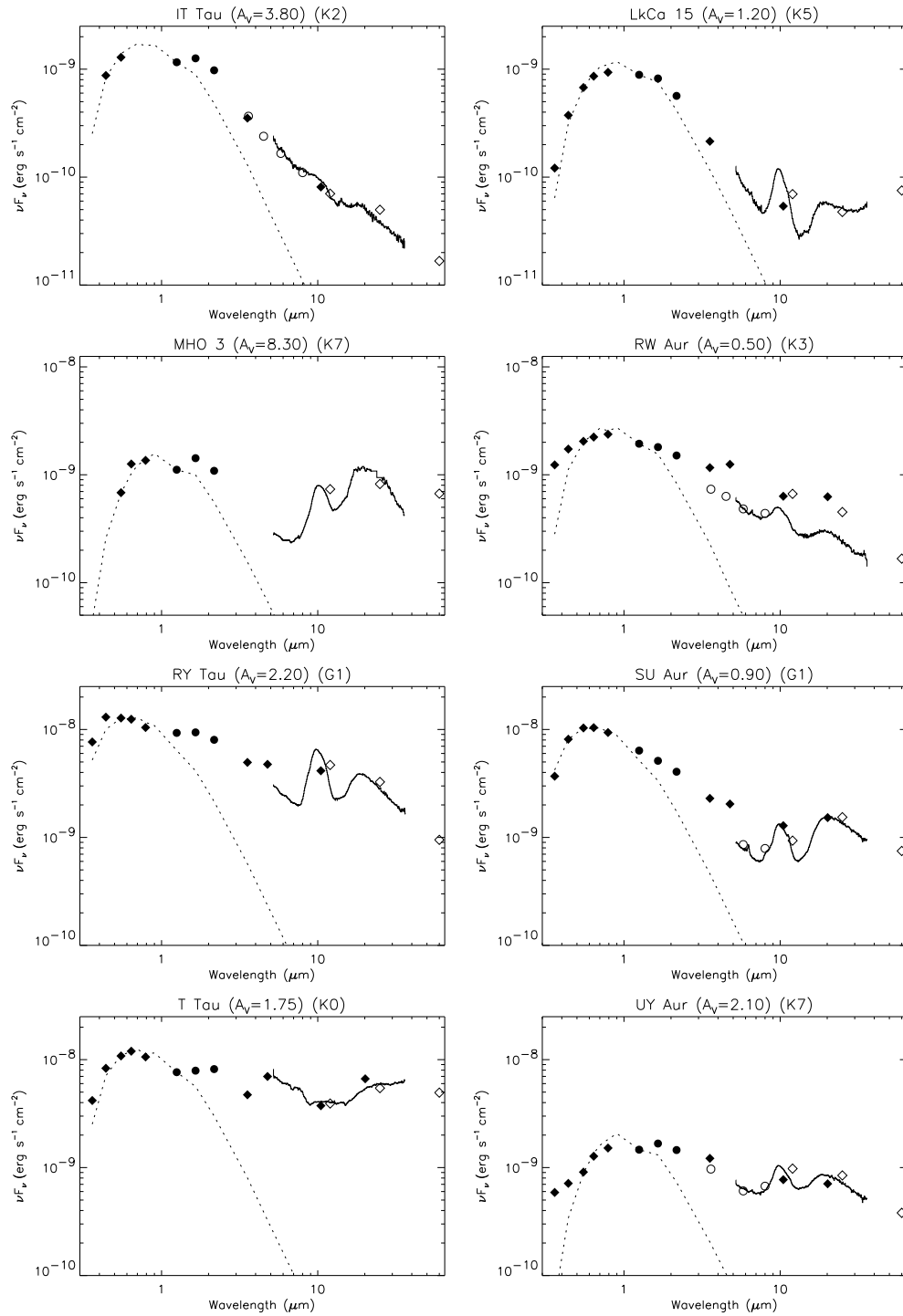


FIG. 1.— continued.

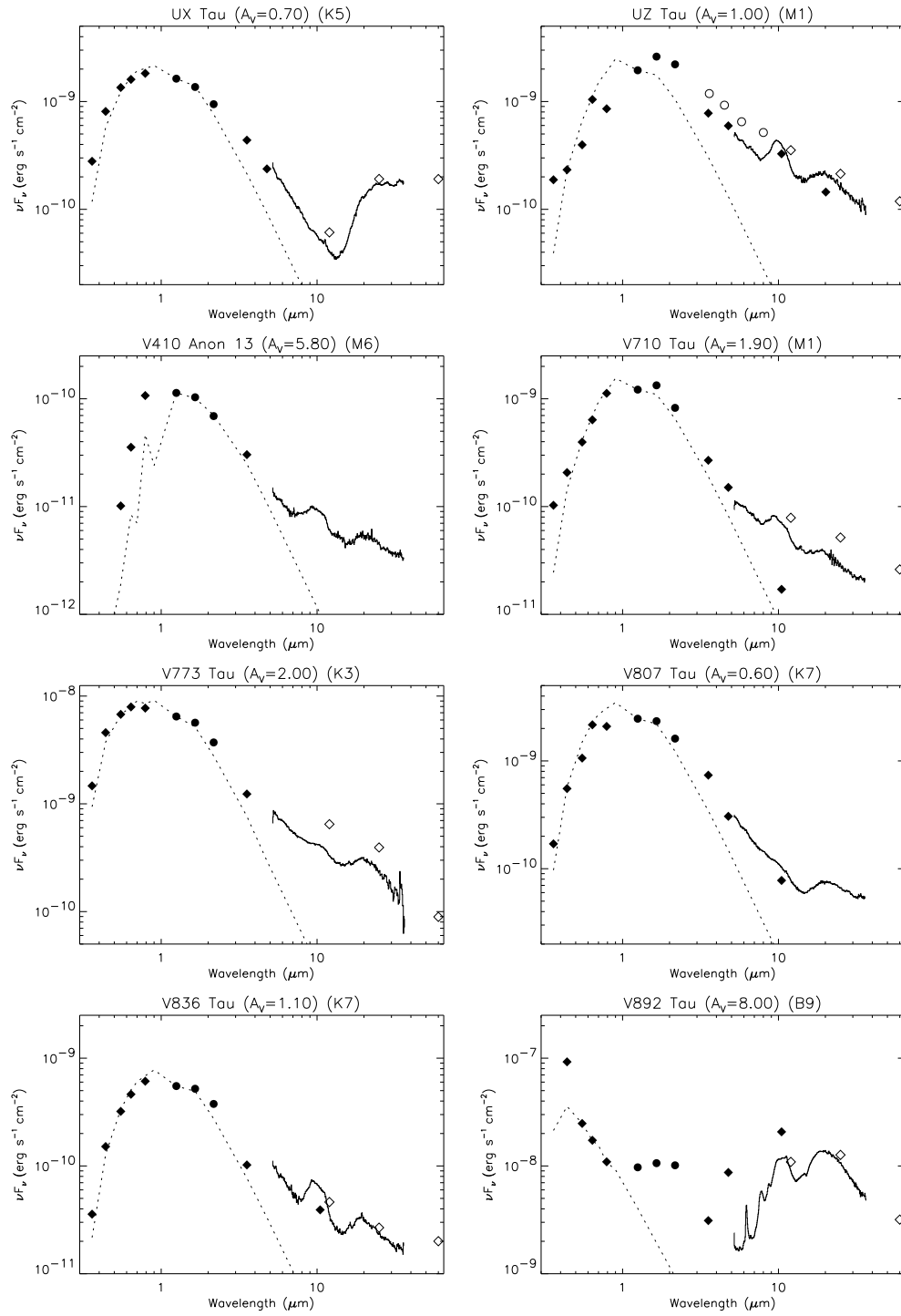


FIG. 1.— continued.

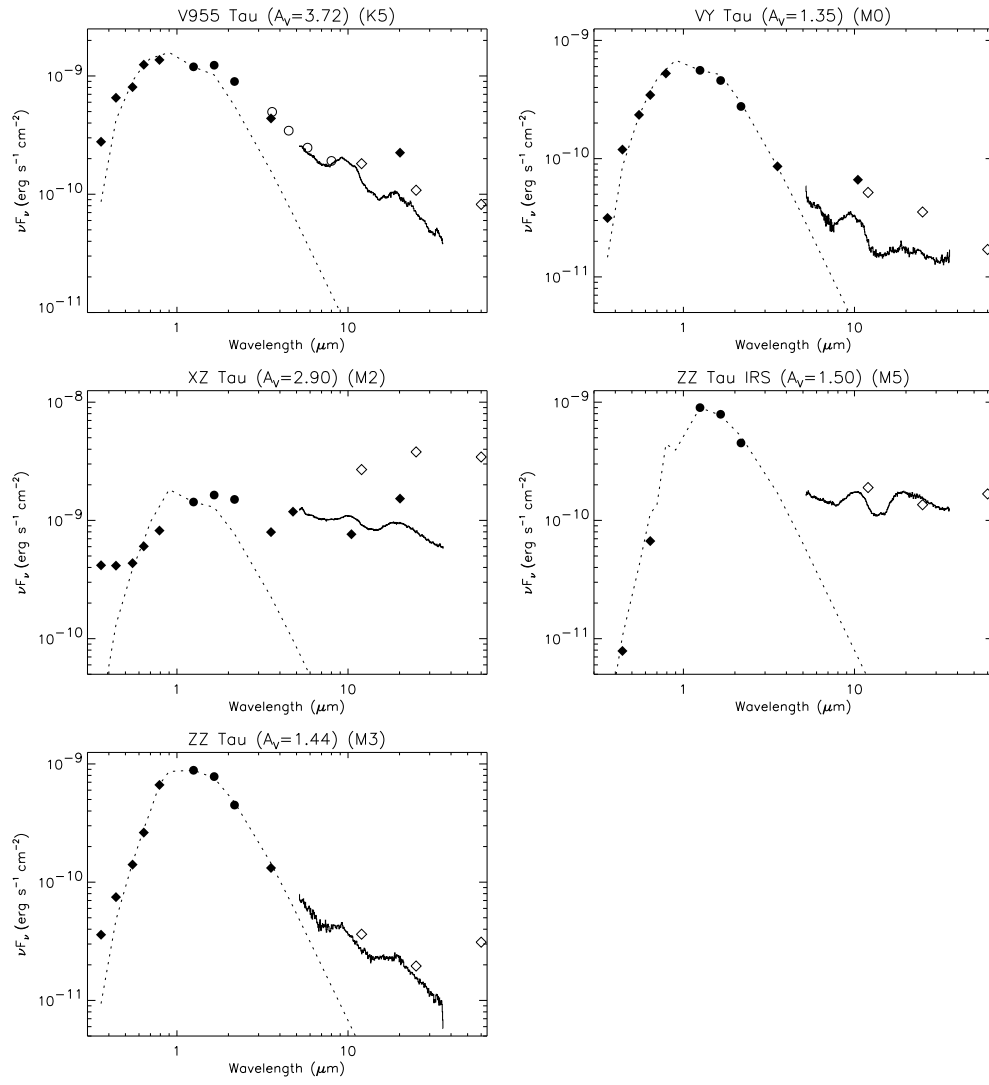


FIG. 1.— continued.

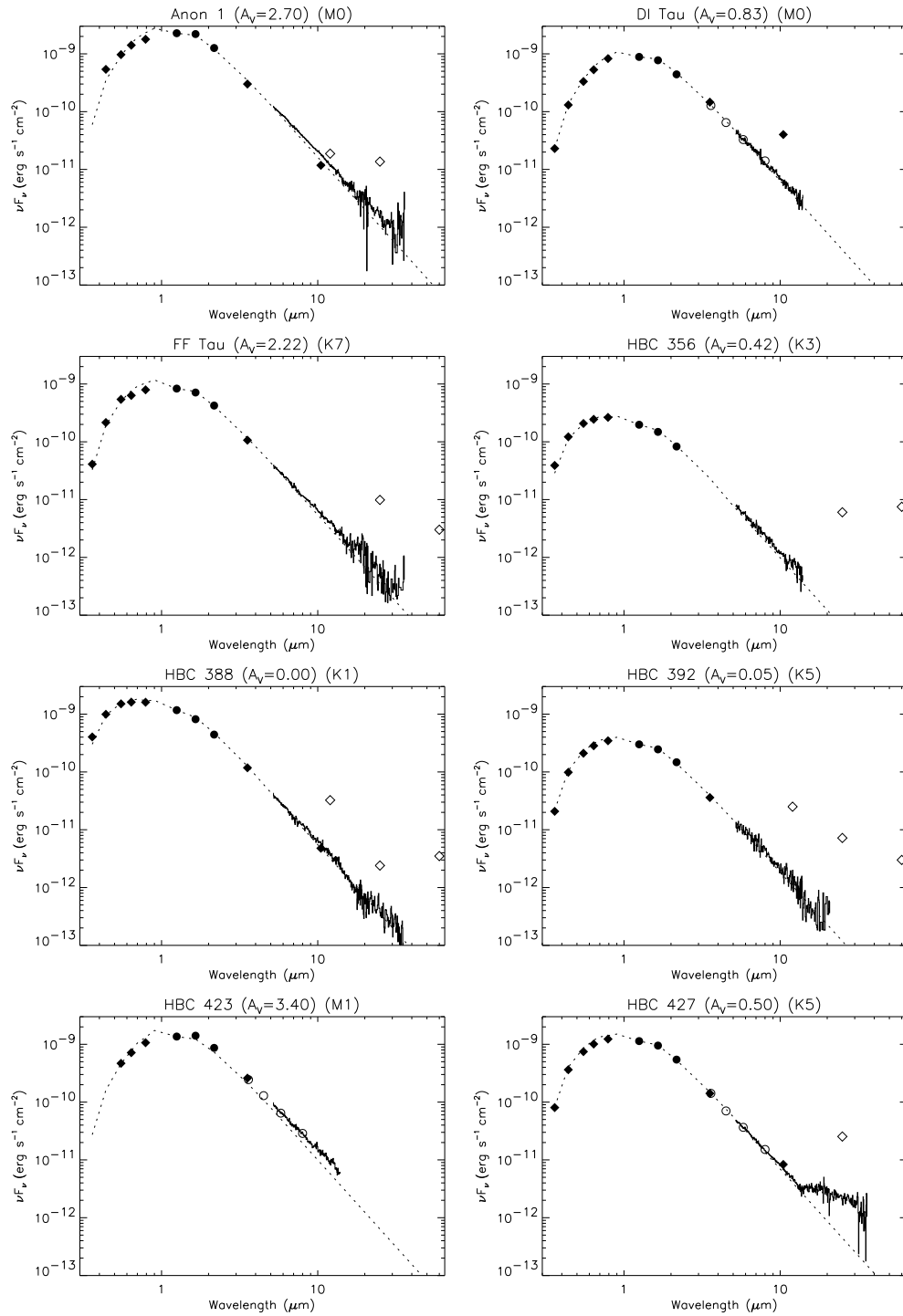


FIG. 2.— SED plots of the Class III objects in our sample, ordered alphabetically by their name. All fluxes, including the IRS spectrum, were dereddened using Mathis’s reddening law (Mathis 1990) and the extinctions listed in table 3. See Figure 1 legend for a description of the plotting symbols.

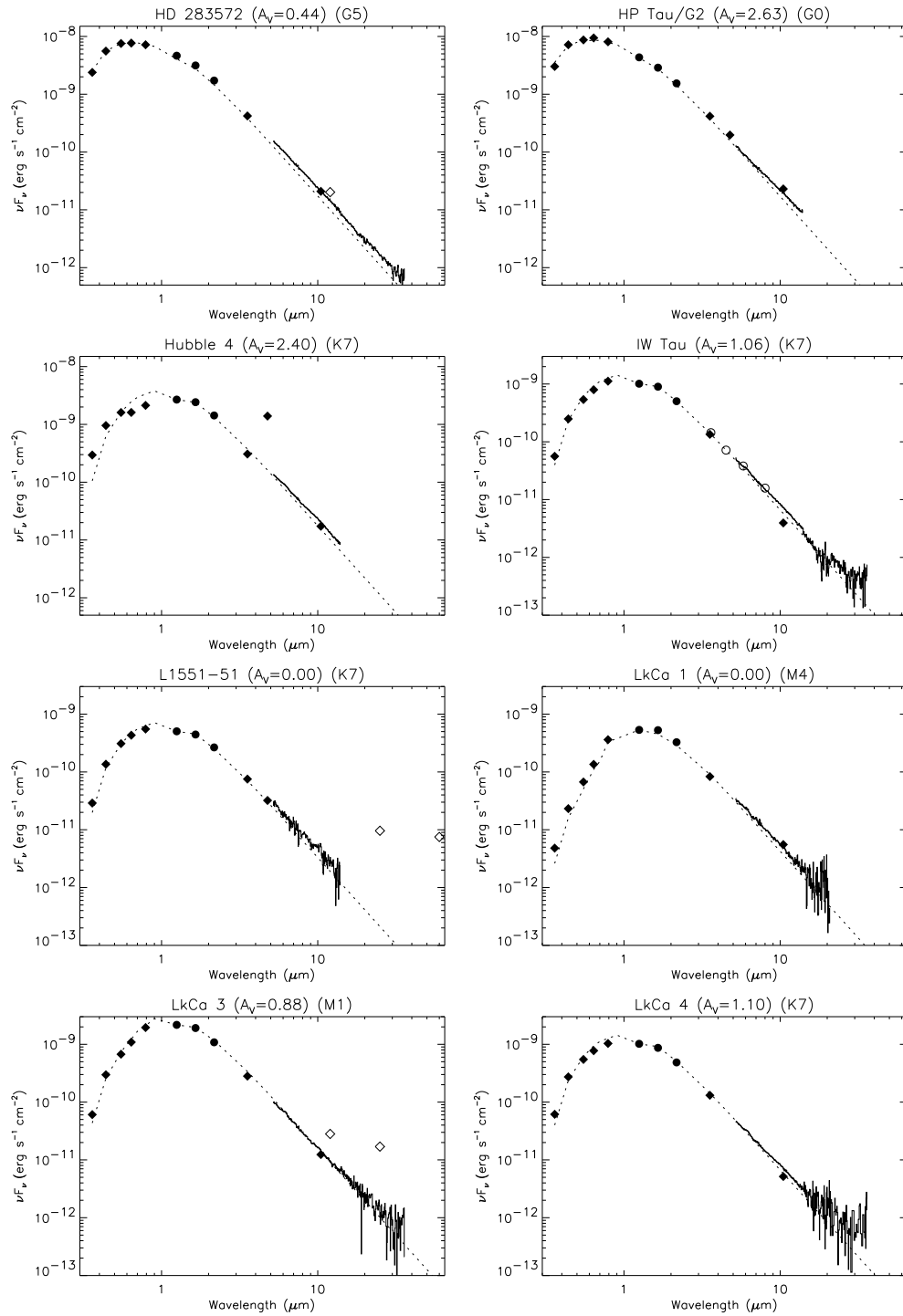


FIG. 2.— continued.

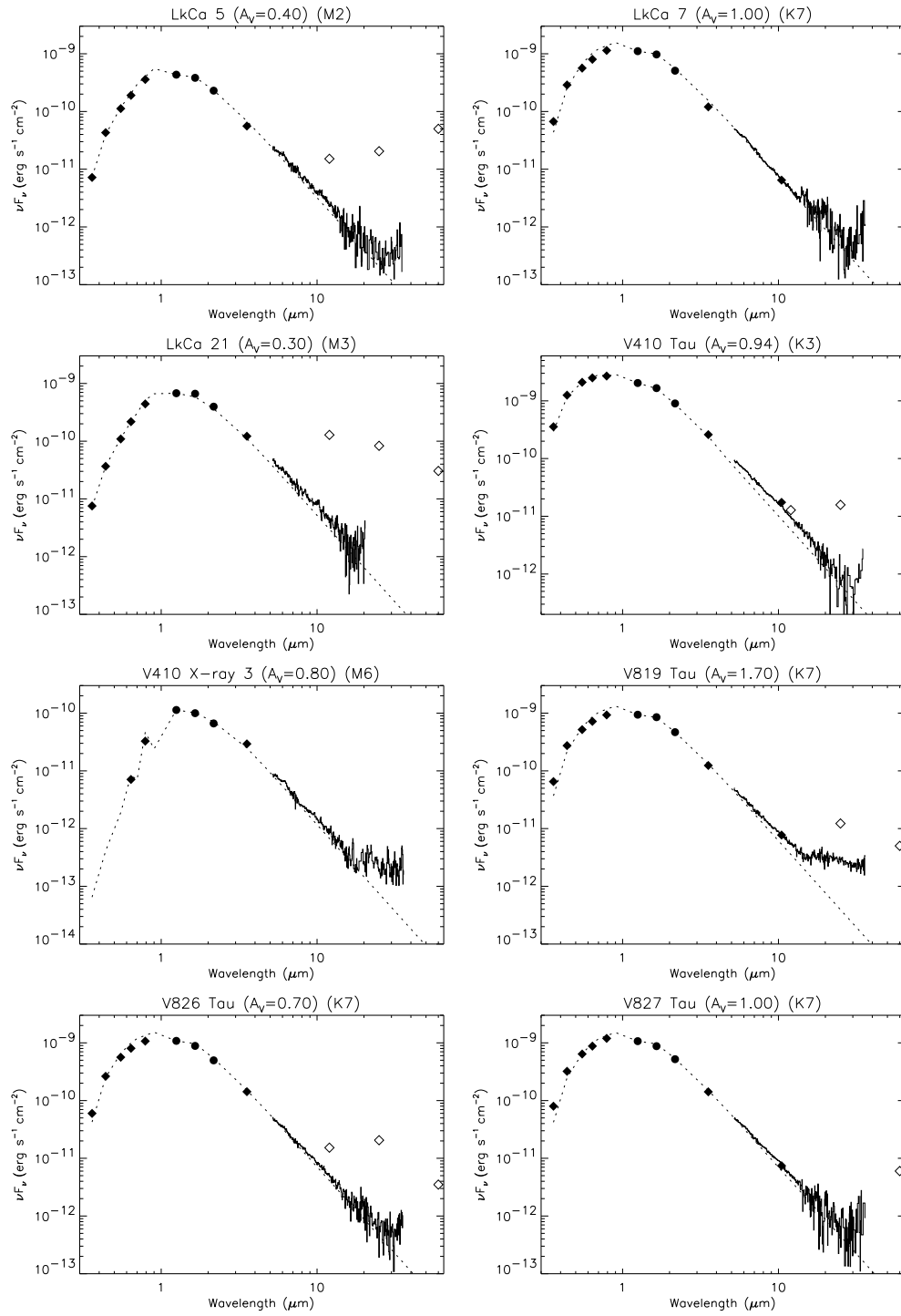


FIG. 2.— continued.

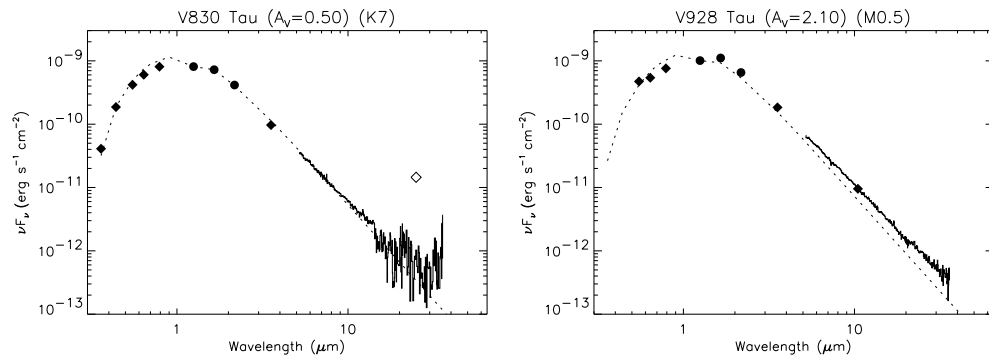


FIG. 2.— continued.

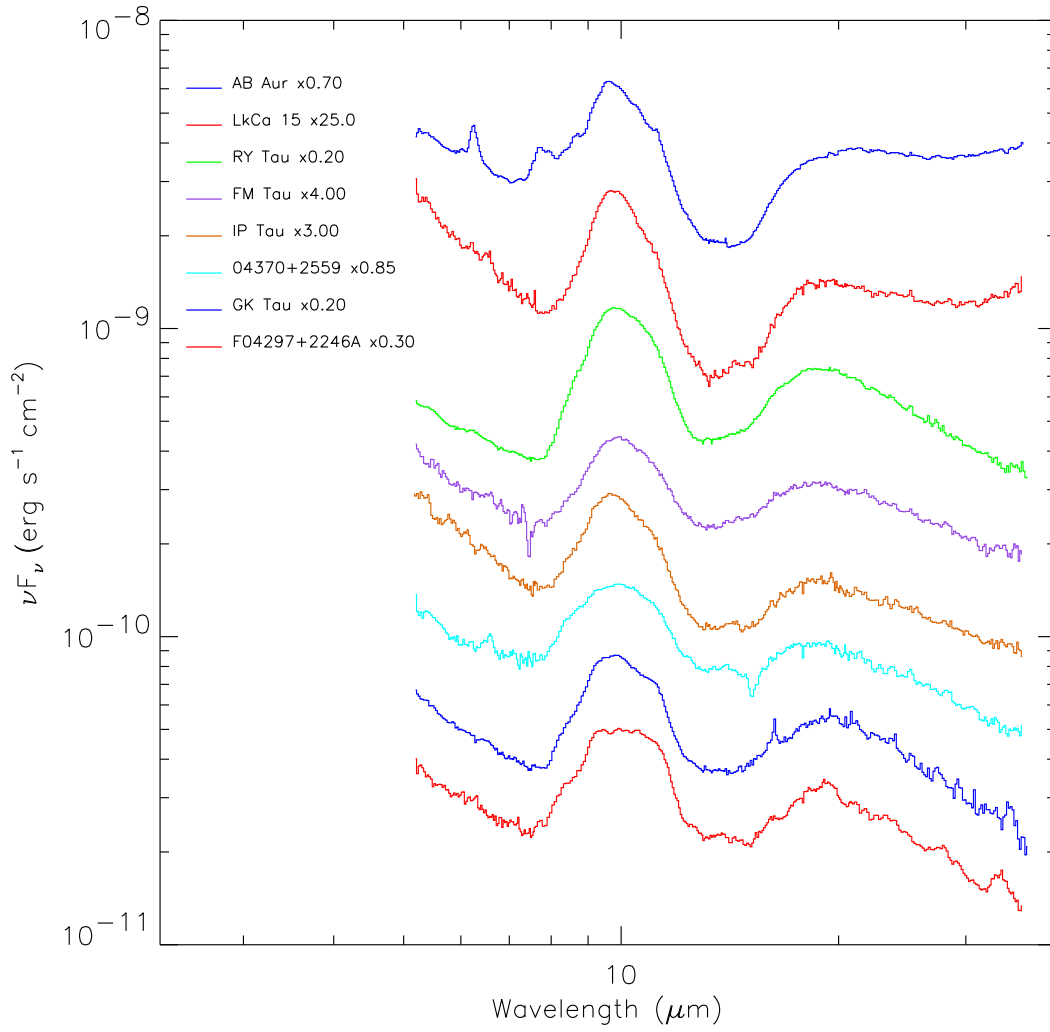


FIG. 3.— Morphological sequence of Class II objects: group A.

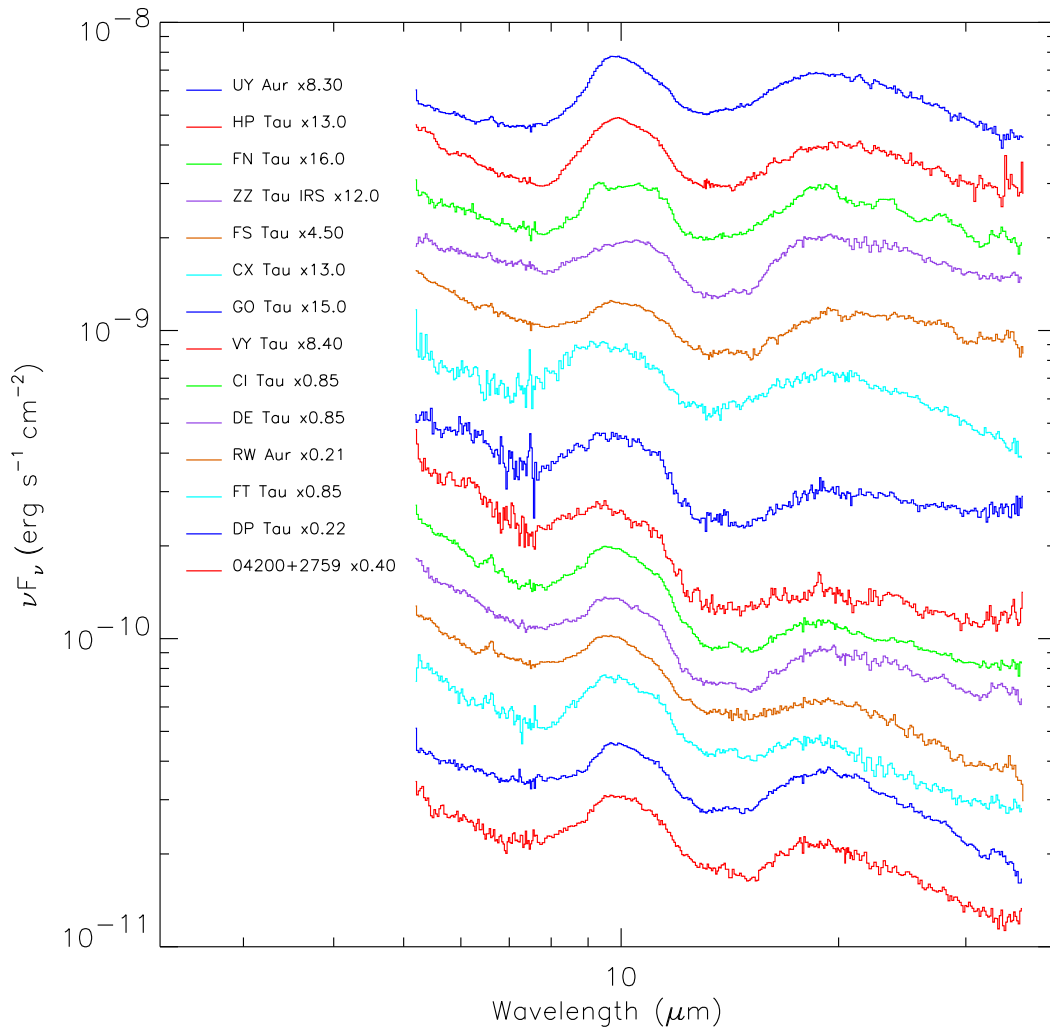


FIG. 4.— Morphological sequence of Class II objects: group B.

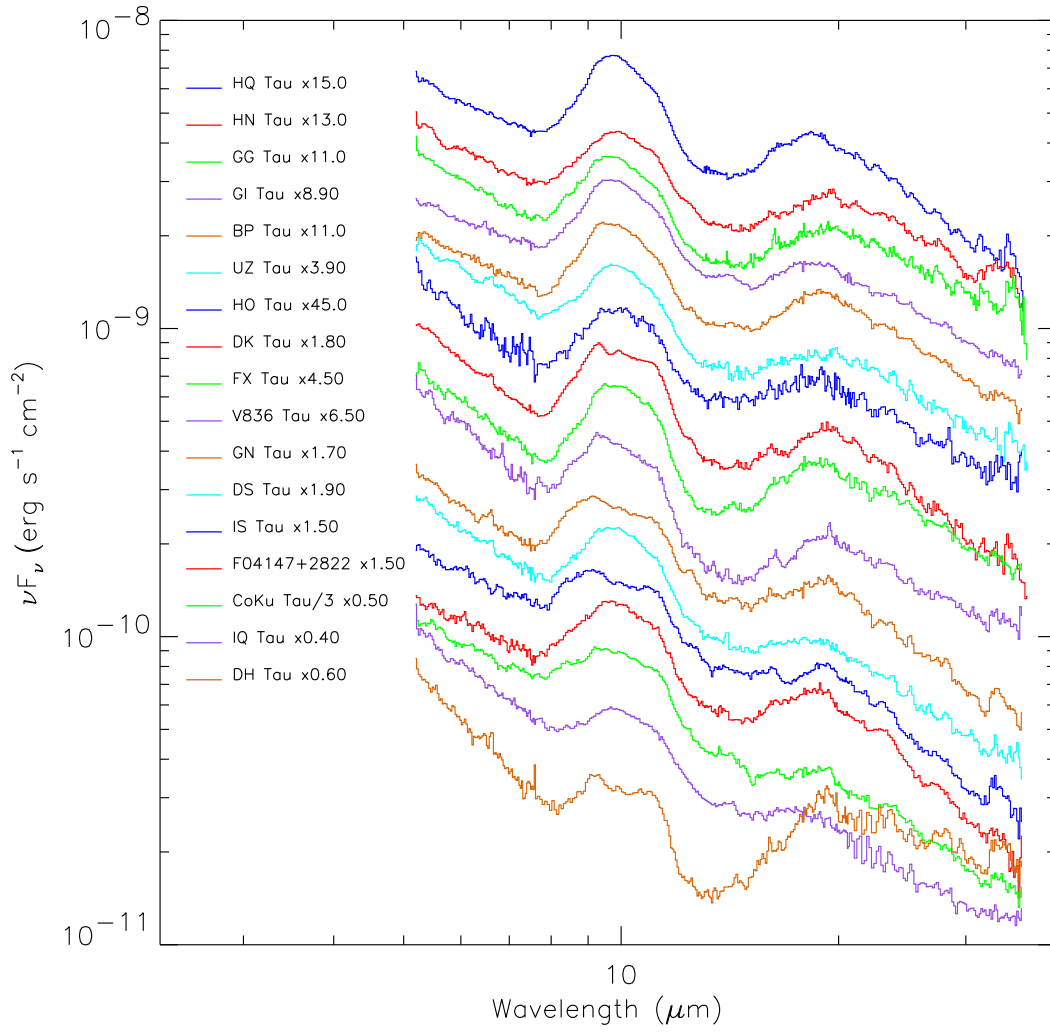


FIG. 5.— Morphological sequence of Class II objects: group C.

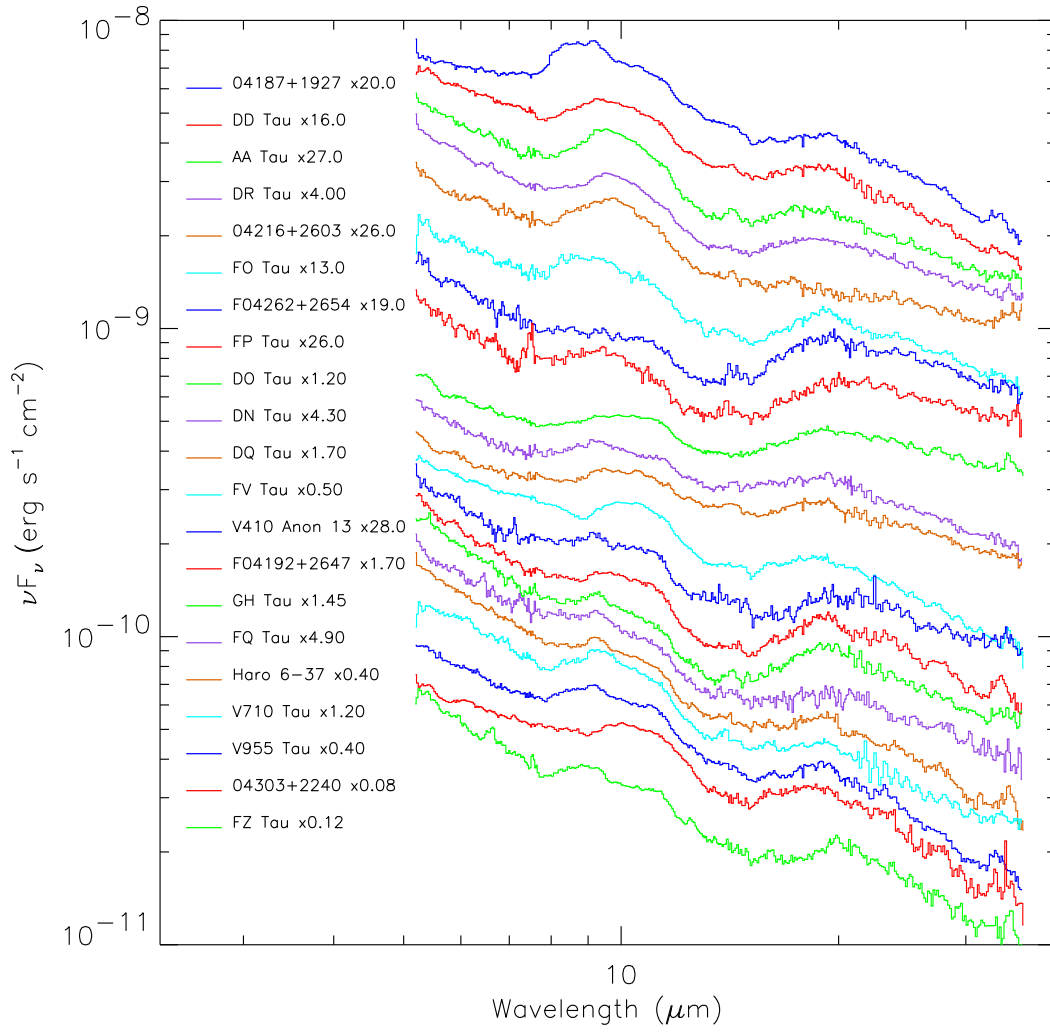


FIG. 6.— Morphological sequence of Class II objects: group D.

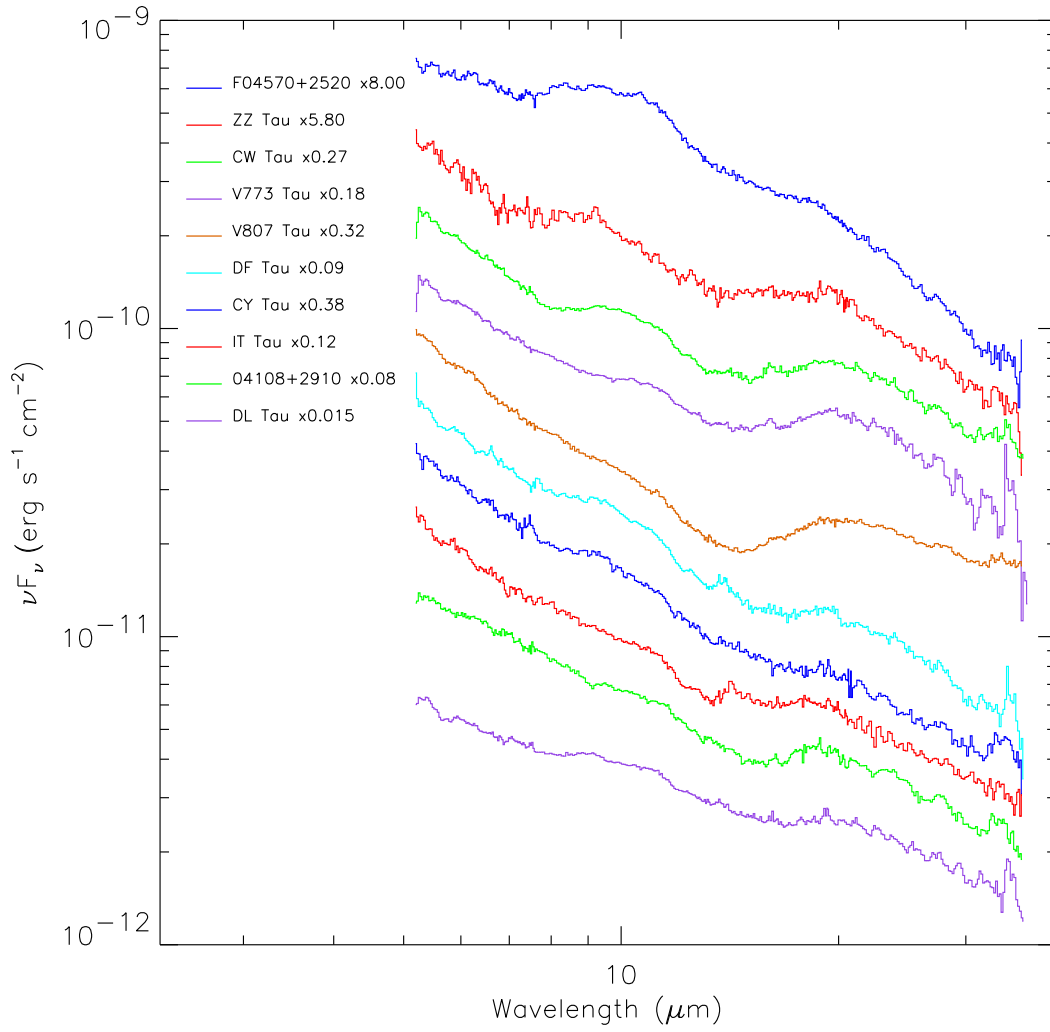


FIG. 7.— Morphological sequence of Class II objects: group E.

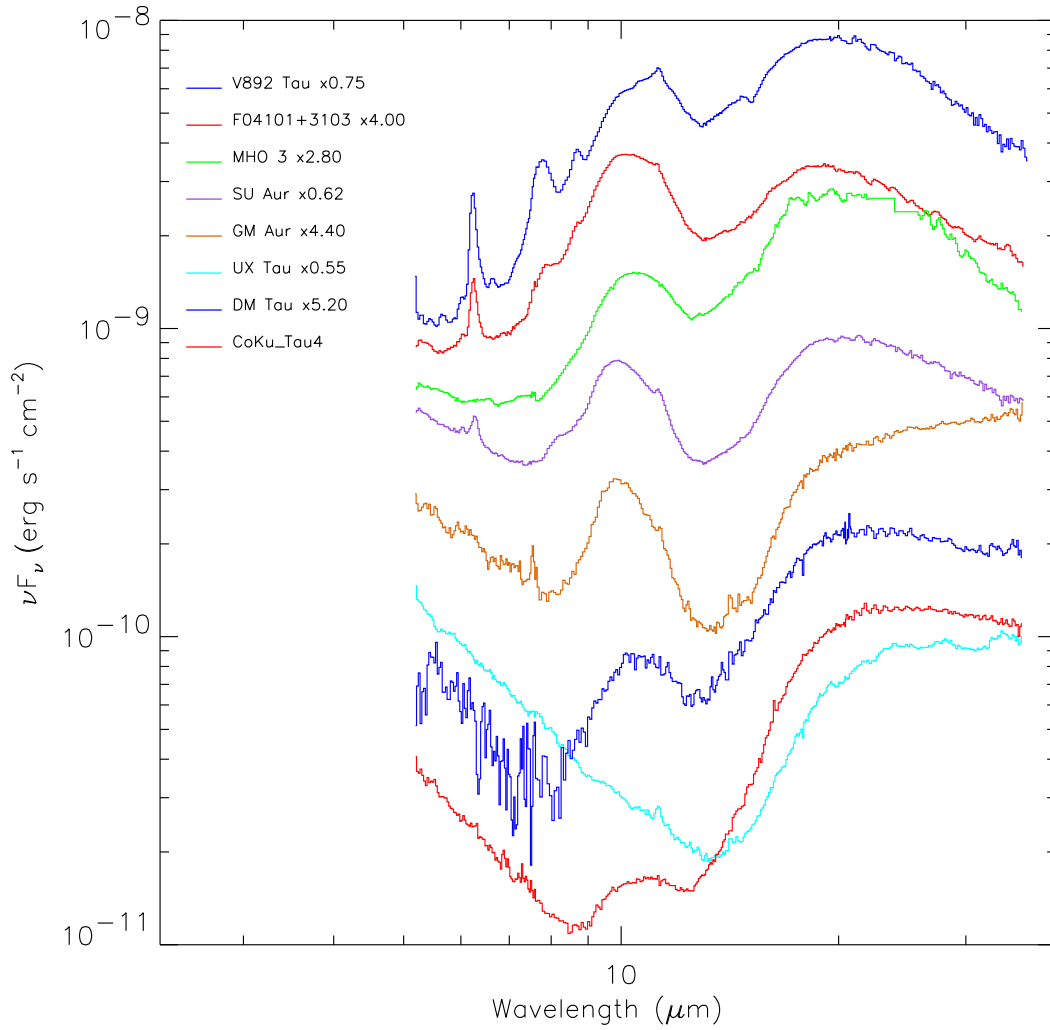


FIG. 8.— Morphological sequence of Class II objects; some of the “outliers” of the morphological sequence: Herbig Ae/Be stars, Class II objects with rising SEDs over the IRS spectral range, and the so-called transitional disks.

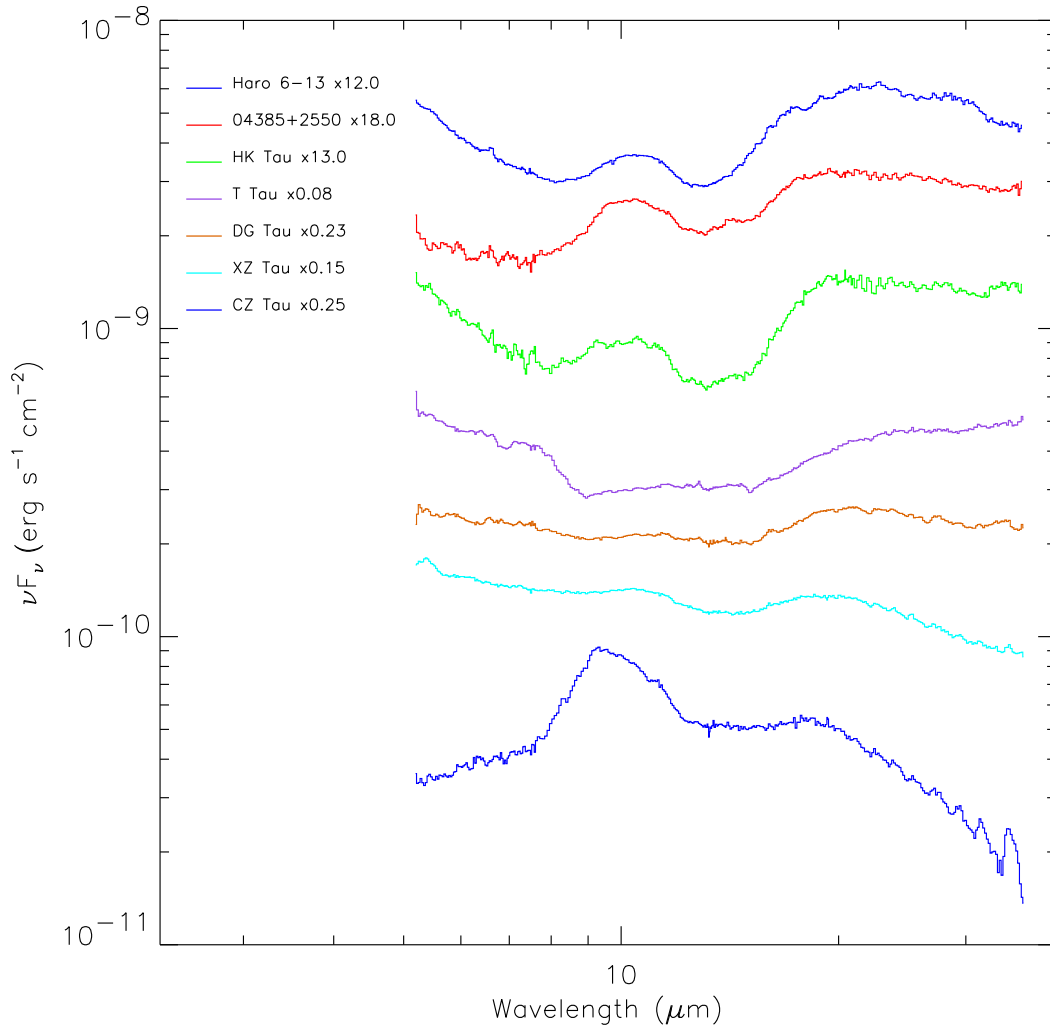


FIG. 9.— Morphological sequence of Class II objects; remaining “outliers” of the morphological sequence: embedded/heavily reddened T Tauri stars, and CZ Tau.

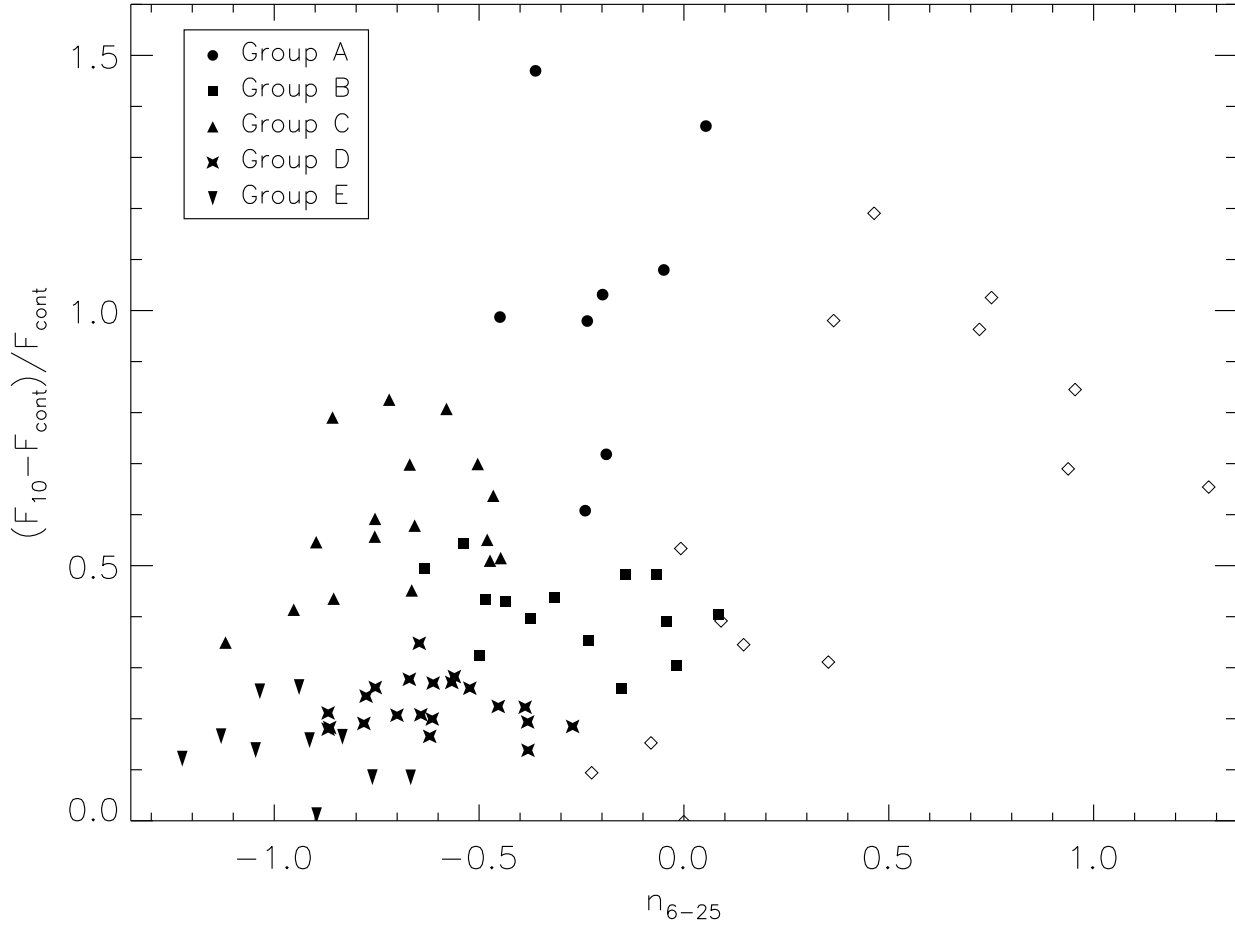


FIG. 10.— Strength of the continuum-subtracted 10- $\mu\text{m}$  feature, normalized to the continuum, vs. the spectral index between 6 and 25  $\mu\text{m}$ ,  $n_{6-25}$ . The data points belonging to the groups defined in our morphological sequence are identified by different plotting symbols: group A – circles, group B – squares, group C – upward facing triangles, group D – stars, group E – downward facing triangles. The open diamonds identify the “outliers” of the morphological sequence.

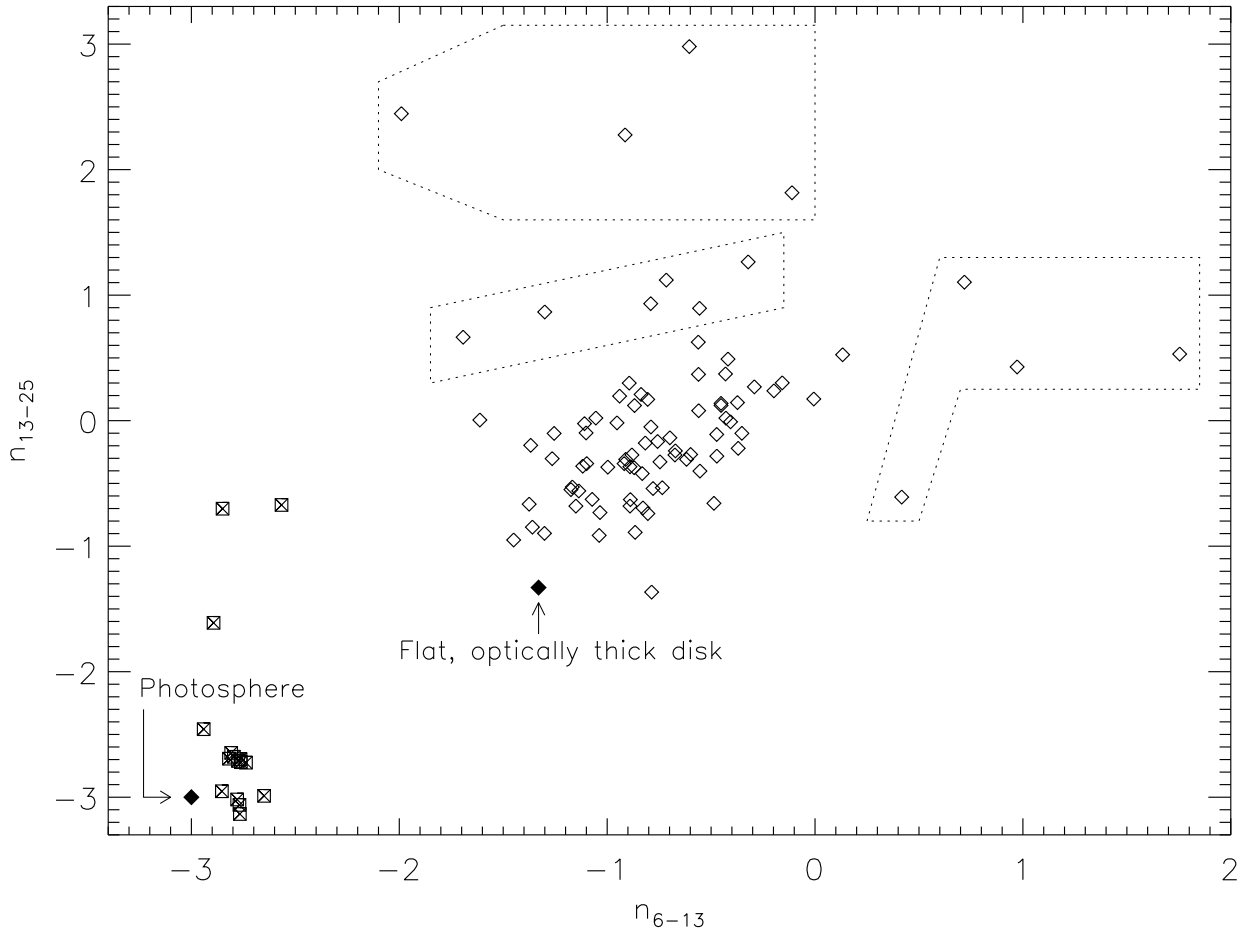


FIG. 11.— Spectral index  $n \equiv d \log(\lambda F_\lambda) / d \log(\lambda)$  evaluated between 13 and 25  $\mu\text{m}$  vs. the spectral index between 6 and 13  $\mu\text{m}$  for our sample of Class II (*open diamonds*) and Class III (*crossed squares*) objects, together with values for a stellar photosphere in the Rayleigh-Jeans limit ( $\lambda F_\lambda \propto \lambda^{-3}$ , i.e.  $n = -3$ ) and for a geometrically thin, optically thick disk ( $\lambda F_\lambda \propto \lambda^{-4/3}$ , i.e.  $n = -4/3$ ). The dotted regions delineate outliers in the plot discussed in the text.

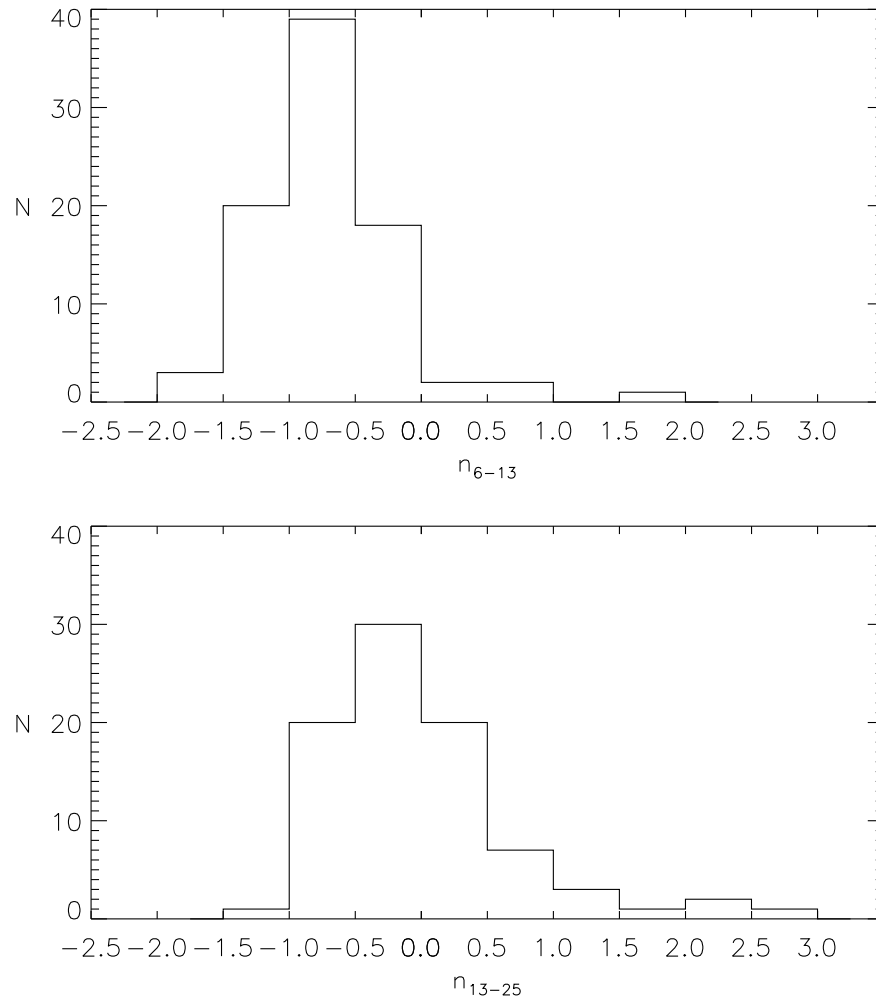


FIG. 12.— Frequency distribution of the spectral indices  $n_{6-13}$  (*top*) and  $n_{13-25}$  (*bottom*) for our sample of Class II objects.

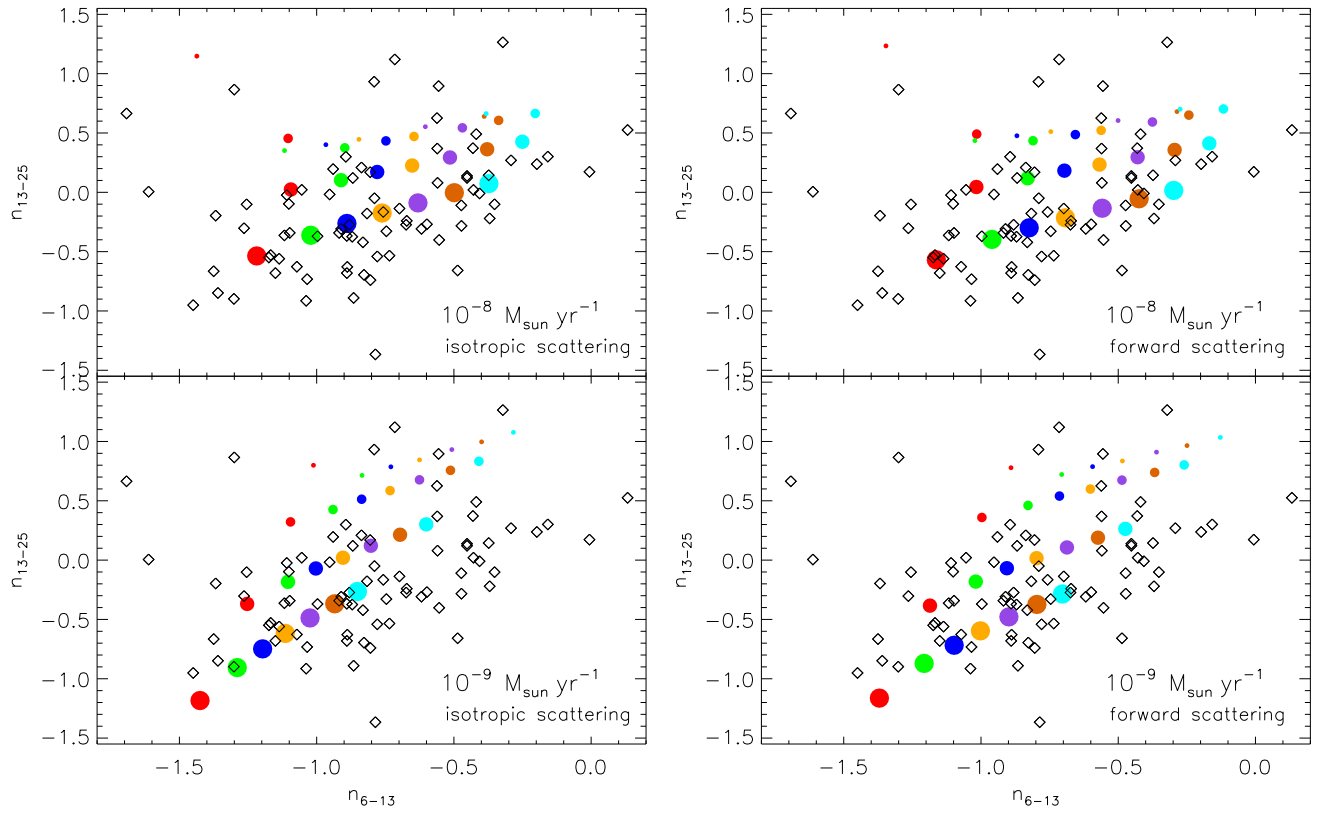


FIG. 13.— Spectral index between 13 and 25  $\mu\text{m}$  vs. the spectral index between 6 and 13  $\mu\text{m}$  for our sample of Class II objects (*open diamonds*) and for accretion disk models (*filled circles*) with  $10^{-8} M_{\odot} \text{yr}^{-1}$  (*upper panels*) and  $10^{-9} M_{\odot} \text{yr}^{-1}$  (*lower panels*). The models on the left-hand side were computed assuming isotropic scattering, while the models on the right-hand side included only perfectly forward scattering dust grains. The colors of the filled circles represent the following inclination angles: red –  $75^{\circ}$ , green –  $60^{\circ}$ , dark blue –  $50^{\circ}$ , yellow –  $40^{\circ}$ , purple –  $30^{\circ}$ , orange –  $20^{\circ}$ , and light blue –  $11^{\circ}$ . The sizes of the filled circles represent a depletion factor  $\epsilon$  of 0.001, 0.01, 0.1, and 1 from largest to smallest, respectively.

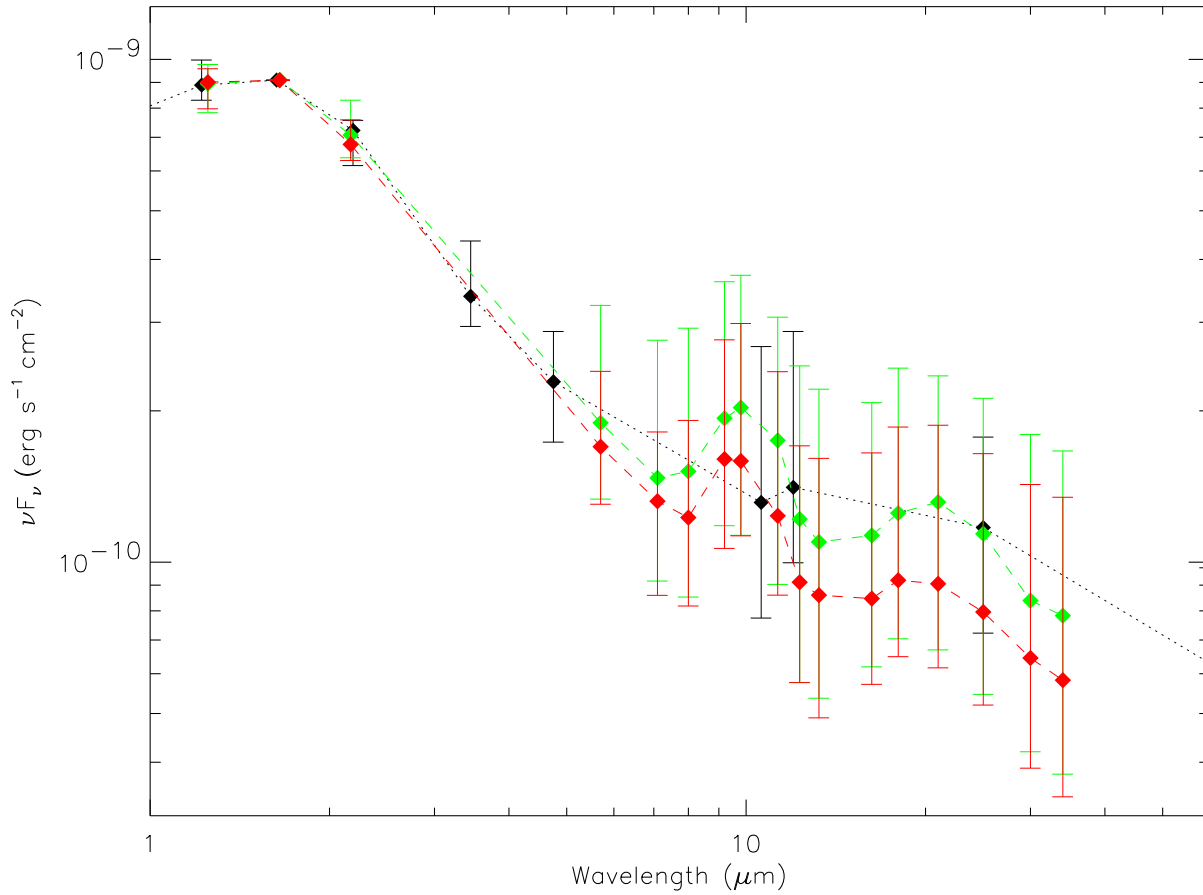


FIG. 14.— Median SED from 1.25 to 34  $\mu\text{m}$  computed using 2MASS photometry and the IRS spectrum of all 85 Class II objects (*green*) and of those 55 Class II objects with spectral types between K5 and M2 (*red*). Also shown is the median SED from D'Alessio et al. (1999) (*black*). The error bars define the quartiles, i.e. the range around the median where 50% of all flux values lie.

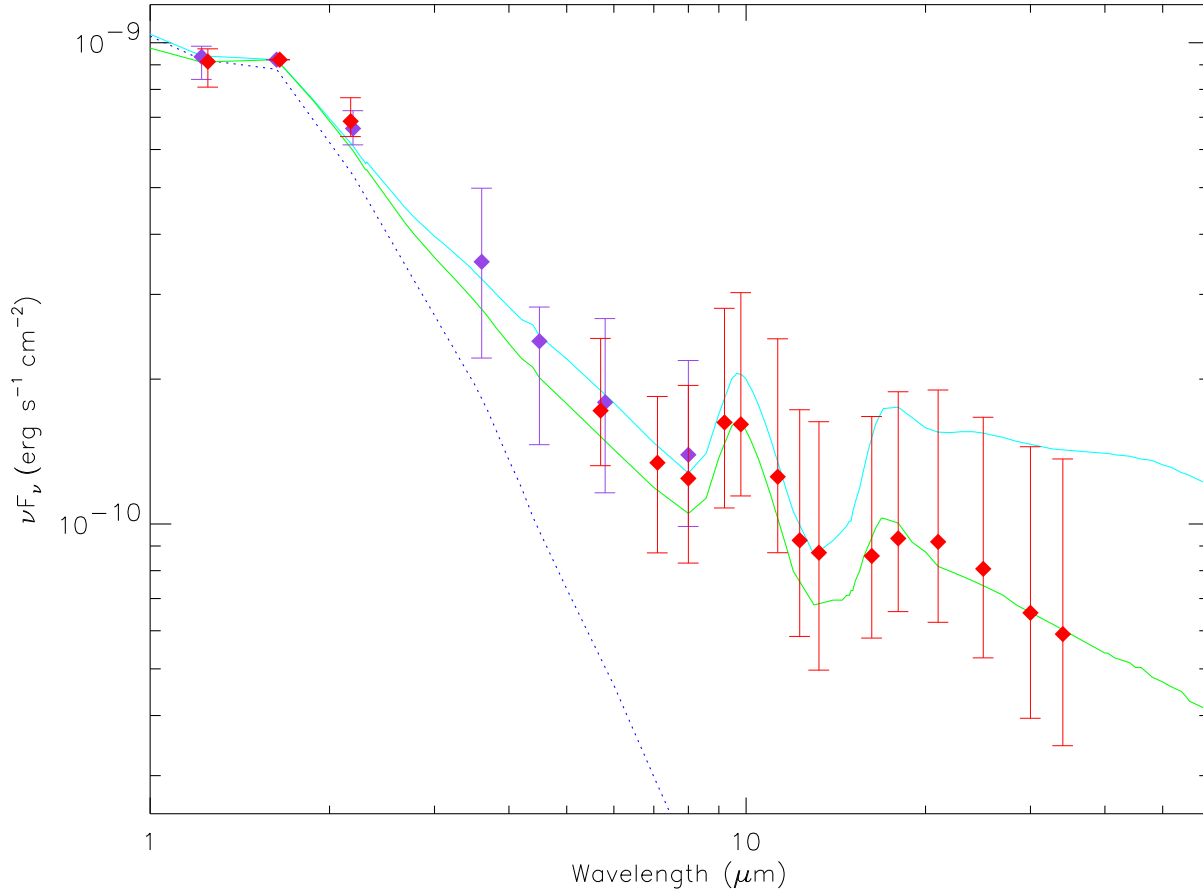


FIG. 15.— Median SED from 1.25 to 34  $\mu\text{m}$  computed using 2MASS photometry and the IRS spectrum of only those Class II objects with spectral types between K5 and M2 (*red*), as well as the median SED constructed using IRAC data from Hartmann et al. (2005a) (*purple*), compared to two models with  $\dot{M} = 3 \times 10^{-8} M_{\odot} \text{ yr}^{-1}$ ,  $i=60^{\circ}$ , dust consisting of amorphous pyroxene and graphite, and two values of settling parameter  $\epsilon$  (*upper, light blue line*,  $\epsilon = 0.1$ ; *lower, green line*,  $\epsilon = 0.001$ ). The dotted line represents the photosphere (SED of the WTTS HBC 427).

TABLE 1  
 PROPERTIES OF OBSERVED CLASS II OBJECTS IN MULTIPLE SYSTEMS

Name	N	Separation ["]	Spectral Type	CTTS (C)/ WTTS (W)	Brightness Comparison	Ref.
(1)	(2)	(3)	(4)	(5)	(6)	(7)
04370+2559 (A,B)	2	4.3''	~ K3-M1	C	A ≫ B	20,21
04385+2550 (A,B)	2	18.9''	M0	C	A ≫ B	22,2
CoKu Tau/3 (A,B)	2	2.05''	M1	C	A > B	1
CZ Tau (A,B) <sup>a</sup>	2	0.32''	M3	W	A ~ B	1
DD Tau (A,B) <sup>a</sup>	2	0.56''	M3+M3	C	A ~ B	1
DF Tau (A,B)	2	0.09''	M0.5+M3	C	A ~ B	1
DH Tau <sup>b</sup>	2	15''	M2+M2	C	DH > DI	7,8
DK Tau (A,B)	2	2.30''	K9+M1	C	A > B	1,7
DQ Tau (A,B)	2	SB	K5	C	A ~ B	12
F04192+2647 (A,B)	2	23.3''	...	...	A > B	23
F04297+2246 (A,B)	2	6.6''	...	...	A > B	23
FM Tau <sup>c</sup>	2	37.3''	M2	C	FM < V773	7,8
FO Tau (A,B)	2	0.15''	M2+M2	C	A ~ B	1
FQ Tau (A,B)	2	0.76''	M3+M3.5	C	A ~ B	1,17
FS Tau (Aa,Ab,B)	3	0.23'' (Aa,Ab), 20'' (A-B)	M1+M4 (Aa,Ab)	C	Aa > Ab	1,24
FV Tau (A,B) <sup>d</sup>	2	0.72''	K5+K6	C	A ~ B, FV > FV/c	1
FX Tau (A,B)	2	0.89''	M1+M4	C+W	A > B	1,6
FZ Tau <sup>e</sup>	2	16.9''	M0+K5	C	FZ > FY	7,8
GG Tau (A,B) <sup>f</sup>	4	10.3''	...	C	A ≫ B	1
GG Tau (Aa,Ab)	2	0.25''	K7+M0.5	C	Aa ≳ Ab	1
GG Tau (Ba,Bb)	2	1.48''	M5.5+M7.5	C	Ba > Bb	1
GH Tau (A,B) <sup>g</sup>	2	0.31''	M1.5+M2	C	A ~ B	1
GI Tau <sup>h</sup>	2	12.9''	K6	C	GI ~ GK	5,6
GK Tau (A,B) <sup>h</sup>	2	2.5''	K7	C	A ≫ B	5,6
GN Tau (A,B)	2	0.33''	M2.5	C	A ~ B	1,26
Haro 6-37 (Aa,Ab,B)	3	2.62'' (A,B), 0.33'' (Aa,Ab)	K7+M1	C	Aa > Ab, A > B	1,11
HK Tau (A,B)	2	2.34''	M1+M2	C	A ≫ B	1,7
HN Tau (A,B)	2	3.11''	K5+M4	C	A ≫ B	1
HP Tau (A,B) <sup>i</sup>	2	0.017''	K2	C	A > B	7,8,15
IS Tau (A,B)	2	0.22''	K7+M4.5	C+W	A > B	1
IT Tau (A,B)	2	2.39''	K3+M4	C	A ≳ B	1,6
RW Aur (A,B,C) <sup>j</sup>	3	1.42'' (A-BC), 0.12'' (B-C)	K1+K5 (A,B)	C	A > B ≫ C	1,10
T Tau (N,Sa,Sb)	3	0.70'' (N-S), 0.1'' (Sa-Sb)	K0	C	N ~ Sa ~ Sb	1,3
UX Tau (A,B,C)	4	5.86'' (A-B), 2.63'' (A-C)	K5+M2+M5	C+W+W	A > B, A ≫ C	1
UX Tau (Ba,Bb)	2	0.138''	M2	W	Ba > Bb	11
UY Aur (A,B)	2	0.88''	M0+M2.5	C	A ≳ B	1,17
VZ Tau (A,Ba,Bb)	4	SB (A), 3.54'' (A-Ba), 0.37'' (Ba-Bb)	M1+M2+M2	C	A > B, Ba ~ Bb	1,13
V710 Tau (A,B)	2	3.17''	M0.5+M2	C+W	A ~ B	1
V773 Tau (AB,C,D)	4	SB (AB), 0.12'' (AB-C), 0.24'' (AB-D)	K2+M0 (AB,C)	W+C	D > C > AB	1,4
V807 Tau (A,Ba,Bb) <sup>g</sup>	3	0.30'' (A-B), 0.04'' (Ba-Bb)	K7+M3	C+W	A > B, Ba ~ Bb	25,1
V892 Tau (Aa,Ab,B)	3	0.06'', 4.10''	B9+M2	W	Aa ~ Ab, A ≫ B	16,19
V955 Tau (A,B)	2	0.33''	K5+M1	C	A > B	1
VY Tau (A,B)	2	0.66''	M0	W	A > B	1
XZ Tau (A,B)	2	0.30''	M3+M1.5	C	B > A	1
ZZ Tau IRS <sup>k</sup>	2	35''	M4.5	C	ZZ IRS > ZZ	2
ZZ Tau (A,B)	2	0.04''	M3	C	A ≳ B	9

REFERENCES. — (1) White & Ghez (2001); (2) White & Hillenbrand (2004); (3) Koresko (2000); (4) Duchêne et al. (2003); (5) Kenyon & Hartmann (1995); (6) Duchêne et al. (1999); (7) Monin et al. (1998); (8) Hartigan, Strom, & Strom (1994); (9) Simon et al. (1996); (10) Ghez et al. (1993); (11) Duchêne (1999); (12) Mathieu et al. (1997); (13) Mathieu, Martin, & Magazzu (1996); (14) White & Hillenbrand (2005); (15) Richichi et al. (1994); (16) Leinert, Richichi, & Haas (1997); (17) Hartigan & Kenyon (2003); (18) Padgett et al. (1999); (19) Smith et al. (2005); (20) Itoh et al. (1999); (21) Itoh et al. (2002); (22) Duchêne et al. (2004); (23) 2MASS All-Sky Catalog of Point Sources; (24) Mundt et al. (1984); (25) Schaefer et al. (2003); (26) White & Basri (2003)

NOTE. — Column (1) gives the name of the object, column (2) the number of components, column (3) their separation in arcseconds (SB means “spectroscopic binary”), column (4) the spectral type (if only one type is listed, it is usually the one of the brighter star in the system), column (5) lists whether the components are classical or weak-lined T Tauri stars (if only one identifier is given, it applies to all components), column (6) shows how the components compare in brightness, and column (7) gives the references for the data listed in the previous columns.

<sup>a</sup> CZ Tau (A,B) is 30''.1 from DD Tau (A,B).

<sup>b</sup> The other component in the binary is DI Tau, which is itself a 0''.12 binary.

<sup>c</sup> The other component in the binary (if it is a real bound system) is V773 Tau, a quadruple system.

<sup>d</sup> FV Tau/c (a 0''.7 binary) is 12''.3 from FV Tau.

<sup>e</sup> The other component in the binary is FY Tau.

<sup>f</sup> We only observed GG Tau Aa+Ab with the IRS.

<sup>g</sup> GH Tau and V807 Tau are separated by 21''.5.

<sup>h</sup> GI Tau and GK Tau are separated by 12''.9.

<sup>i</sup> HP Tau might form a triple systems with HP Tau/G2 (21''.4 away) and HP Tau/G3 (17''.3 away).

<sup>j</sup> RW Aur C could be a false detection (White & Ghez 2001).

<sup>k</sup> ZZ Tau IRS is 35'' from ZZ Tau.

TABLE 2  
 PROPERTIES OF OBSERVED CLASS II OBJECTS

Name	Adopted Spectral Type	$A_V$	CTTS (C)/ WTTS (W)	Ref.
(1)	(2)	(3)	(4)	(5)
04108+2910	M0	1.40 <sup>a</sup>	C	1,3
04187+1927	M0	...	C	1,4
04200+2759	...	...	C	1,5
04216+2603	M1	...	C	1,3
04303+2240	...	11.7	C	6
04370+2559 (A,B)	...	9.82	C	7
04385+2550 (A,B)	M0	7.80 <sup>a</sup>	C	6,7
AA Tau	K7	1.75 <sup>a</sup>	C	1,3
AB Aur	A0	0.25	C	8,3
BP Tau	K7	1.00 <sup>a</sup>	C	1,3
CI Tau	K7	2.00 <sup>a</sup>	C	1,3
CoKu Tau/3 (A,B)	M1	5.00 <sup>a</sup>	C	1,2
CoKu Tau/4	M1	3.0	W	9,3
CW Tau	K3	2.75 <sup>a</sup>	C	1,3
CX Tau	M0	1.30 <sup>a</sup>	C	1,3
CY Tau	K7	1.70 <sup>a</sup>	C	1,3
CZ Tau (A,B)	M1	2.45 <sup>a</sup>	W	1,3
DD Tau (A,B)	M3	1.00 <sup>a</sup>	C	1,2
DE Tau	M0	1.20 <sup>a</sup>	C	1,3
DF Tau (A,B)	M0	1.60 <sup>a</sup>	C	1,2
DG Tau	K6	1.60	C	1,10,3
DH Tau	M0	1.70 <sup>a</sup>	C	1,3
DK Tau (A,B)	M0	1.30 <sup>a</sup>	C	1,2
DL Tau	K7	1.50 <sup>a</sup>	C	1,2
DM Tau	M1	0.72 <sup>a</sup>	C	1,2
DN Tau	M0	0.60 <sup>a</sup>	C	1,3
DO Tau	M0	2.05 <sup>a</sup>	C	1,3
DP Tau	M0	0.60 <sup>a</sup>	C	1,3
DQ Tau (A,B)	M0	1.60 <sup>a</sup>	C	1,3
DR Tau	K7	1.20	C	1,3
DS Tau	K5	1.10 <sup>a</sup>	C	1,3
F04101+3103	A1	1.90 <sup>a</sup>	C	1,4
F04147+2822	M4	2.50 <sup>a</sup>	C	1,3
F04192+2647 A	...	...	...	...
F04262+2654	...	...	...	...
F04297+2246 A	...	...	...	...
F04570+2520	...	...	...	...
FM Tau	M0	1.40 <sup>a</sup>	C	1,3
FN Tau	M5	1.35	C	1,3
FO Tau (A,B)	M2	3.03	C	2
FP Tau	M4	0.00	C	2
FQ Tau (A,B)	M2	1.87	C	1,3
FS Tau (Aa,Ab)	M1	1.43 <sup>a</sup>	C	1,2
FT Tau	C	...	...	1
FV Tau (A,B)	K5	5.33	C	2
FX Tau (A,B)	M1	2.00 <sup>a</sup>	C	1,3
FZ Tau	M0	3.70 <sup>a</sup>	C	1,3
GG Tau (Aa,Ab)	M0	1.00 <sup>a</sup>	C	1,2
GH Tau (A,B)	M2	0.97 <sup>a</sup>	C	1,2
GI Tau	K6	2.30 <sup>a</sup>	C	1,3
GK Tau (A,B)	M0	1.15 <sup>a</sup>	C	1,3
GM Aur	K3	1.21	C	2
GN Tau (A,B)	M2	3.50 <sup>a</sup>	C	11,12
GO Tau	M0	2.02 <sup>a</sup>	C	1,3
Haro 6-13	M0	11.9	C	6
Haro 6-37 (Aa,Ab,B)	K7	3.80 <sup>a</sup>	C	1,2
HK Tau (A,B)	M1	2.70 <sup>a</sup>	C	6
HN Tau (A,B)	K5	1.50 <sup>a</sup>	C	1,2
HO Tau	M0	1.30 <sup>a</sup>	C	1,3
HP Tau (A,B)	K3	2.80 <sup>a</sup>	C	1,3
HQ Tau	...	...	...	...
IP Tau	M0	0.51	C	2
IQ Tau	M1	1.44	W	2
IS Tau (A,B)	M0	3.22 <sup>a</sup>	C	1,2
IT Tau (A,B)	K2	3.80 <sup>a</sup>	C	1
LkCa 15	K5	1.20 <sup>a</sup>	C	1,3
MHO 3	K7	8.30 <sup>a</sup>	C	1,13
RW Aur (A,B,C)	K3	0.50 <sup>a</sup>	C	1,2
RY Tau	G1	2.20	C	14,3
SU Aur	G1	0.90	C	14
T Tau (N,Sa,Sb)	K0	1.75 <sup>a</sup>	C	1,2
UX Tau (A,Ba,Bb,C)	K5	0.70 <sup>a</sup>	C	2
UY Aur (A,B)	K7	2.10 <sup>a</sup>	C	1,3

TABLE 2 — *Continued*

Name	Adopted Spectral Type	$A_V$	CTTS (C)/ WTTS (W)	Ref.
(1)	(2)	(3)	(4)	(5)
UZ Tau (A,Ba,Bb)	M1	1.00	C	2
V410 Anon 13	M6	5.80	C	1,15,2
V710 Tau (A,B)	M1	1.90 <sup>a</sup>	C	1,2
V773 Tau (AB,C,D)	K3	2.00 <sup>a</sup>	W	1,2
V807 Tau (A,Ba,Bb)	K7	0.60 <sup>a</sup>	C	1,2
V836 Tau	K7	1.10 <sup>a</sup>	C/W	1,3
V892 Tau (Aa,Ab,B)	B9	8.00 <sup>a</sup>	W	16,3
V955 Tau (A,B)	K5	3.72	C	2
VY Tau (A,B)	M0	1.35 <sup>a</sup>	W	1,3
XZ Tau (A,B)	M2	2.90 <sup>a</sup>	C	1,2
ZZ Tau IRS	M5	1.50 <sup>a</sup>	C	1,6
ZZ Tau (A,B)	M3	1.44 <sup>a</sup>	C	1,3

REFERENCES. — (1) Kenyon & Hartmann (1995); (2) White & Ghez (2001); (3) Kenyon et al. (1998); (4) Kenyon et al. (1990); (5) Kenyon et al. (1994a); (6) White & Hillenbrand (2004); (7) Itoh et al. (2002); (8) DeWarf et al. (2003); (9) D’Alessio et al. (2005); (10) Gullbring et al. (2000); (11) White & Basri (2003); (12) Luhman (2004); (13) Briceño et al. (1998); (14) Calvet et al. (2004); (15) Furlan et al. (2005a); (16) Smith et al. (2005)

NOTE. — Column (1) gives the name of the object, column (2) the adopted spectral type, column (3) the adopted visual extinction (see also note (a) below), column (4) lists whether the object (the primary in case of multiple systems) is a classical or weak-lined T Tauri star, and column (5) gives the references for the data listed in the previous columns.

<sup>a</sup> Value of  $A_V$  derived from the observed V-I colors, spectral types, and intrinsic colors for main-sequence stars listed in Kenyon & Hartmann (1995), using the Mathis (1990) reddening law. In some cases the derived values of  $A_V$  were adjusted to yield a good match between the dereddened and true photospheric colors.

TABLE 3  
 PROPERTIES OF OBSERVED CLASS III OBJECTS

Name	Multiplicity <sup>a</sup>	Adopted Spectral Type	$A_V$	CTTS (C)/ WTTS (W)	Ref.
(1)	(2)	(3)	(4)	(5)	(6)
Anon 1	s	M0	2.70 <sup>b</sup>	W	1,6
DI Tau <sup>c</sup>	0.12'', 15''	M0	0.83 <sup>b</sup>	W	7,2,5
FF Tau (A,B)	0.026''	K7	2.22	W	2,4,5
HBC 356 <sup>d</sup>	1.33''	K3	0.42 <sup>b</sup>	W	3,2
HBC 388	s	K1	0.0	W	1
HBC 392	s	K5	0.05 <sup>b</sup>	W	2,5
HBC 423 <sup>e</sup>	0.24'', 10.4''	M1	3.40 <sup>b</sup>	W	1,2
HBC 427	SB ( $\sim 0.03''$ )	K5	0.50 <sup>b</sup>	W	2,5,9
HD 283572	s	G5	0.44 <sup>b</sup>	W	2,5
HP Tau/G2 <sup>f</sup>	9.9''	G0	2.63 <sup>b</sup>	W	2,4,5
Hubble 4	s	K7	2.40 <sup>b</sup>	W	1
IW Tau (A,B)	0.29''	K7	1.06 <sup>b</sup>	W	1
L1551-51	s	K7	0.0	W	1,6
LkCa 1	s	M4	0.0	W	1
LkCa 3 (A,B)	0.48''	M1	0.88 <sup>b</sup>	W	2,1
LkCa 4	s	K7	1.10 <sup>b</sup>	W	1
LkCa 5	s	M2	0.40 <sup>b</sup>	W	1
LkCa 7 (A,B)	1.02''	K7	1.00 <sup>b</sup>	W	1
LkCa 21	s	M3	0.30 <sup>b</sup>	W	2,6
V410 Tau (A,B,C) <sup>g</sup>	0.07'', 0.29''	K3	0.94 <sup>b</sup>	W	1
V410 X-ray 3	s	M6	0.80 <sup>b</sup>	W	1
V819 Tau	10.5''	K7	1.70 <sup>b</sup>	W	1,8
V826 Tau	SB	K7	0.70 <sup>b</sup>	W	8,5
V827 Tau	s	K7	1.00 <sup>b</sup>	W	1
V830 Tau	s	K7	0.50 <sup>b</sup>	W	1
V928 Tau (A,B)	0.19''	M0.5	2.10 <sup>b</sup>	W	2,6

REFERENCES. — (1) White & Ghez (2001) (2) Kenyon & Hartmann (1995) (3) Duchêne et al. (1999) (4) Simon et al. (1995) (5) Kenyon et al. (1998) (6) Martín et al. (1994) (7) Ghez et al. (1993) (8) Leinert et al. (1993) (9) Steffen et al. (2001)

NOTE. — Column (1) gives the name of the object, column (2) the multiplicity of the object (see footnote a), column (3) the adopted spectral type, column (4) the adopted visual extinction (see also note (b) below), column (5) lists whether the object (the primary in case of multiple systems) is a classical or weak-lined T Tauri star, and column (6) gives the references for the data listed in the previous columns.

<sup>a</sup> The letter “s” means single star; for multiple systems, the separation between the components in arcseconds is listed; SB means “spectroscopic binary”.

<sup>b</sup> Value of  $A_V$  derived from the observed V-I colors, spectral types, and intrinsic colors for main-sequence stars listed in Kenyon & Hartmann (1995), using the Mathis (1990) reddening law. In some cases the derived values of  $A_V$  were adjusted to yield a good match between the dereddened and true photospheric colors.

<sup>c</sup> DI Tau is separated by 15'' from DH Tau; DI Tau is a 0''12 binary.

<sup>d</sup> The other component is HBC 357.

<sup>e</sup> HBC 423 is also known as LkHa 332/G1. The separation between components A and B of HBC 423 is 0''24; the separation between HBC 423 and V955 Tau is 10''4.

<sup>f</sup> HP Tau/G2 is likely part of a triple system consisting of HP Tau, HP Tau/G2, and HP Tau/G3; the separation listed is the distance between HP Tau/G2 and HP Tau/G3 (also a WTTS).

<sup>g</sup> The value of 0''07 is the separation between A and B, 0''29 between A and C.

TABLE 4  
SPECTRAL INDEX  $n_{6-25}$  AND 10- $\mu\text{M}$  FEATURE STRENGTH FOR THE CLASS II  
OBJECTS IN OUR SAMPLE

Name	$n_{6-25}$	$(F_{10}-F_{\text{cont}})/F_{\text{cont}}$	Name	$n_{6-25}$	$(F_{10}-F_{\text{cont}})/F_{\text{cont}}$
04108+2910	-0.90	0.01	FS Tau	-0.15	0.26
04187+1927	-0.56	0.28	FT Tau	-0.48	0.43
04200+2759	-0.32	0.44	FV Tau	-0.62	0.17
04216+2603	-0.57	0.27	FX Tau	-0.58	0.81
04303+2240	-0.70	0.21	FZ Tau	-0.86	0.18
04370+2559	-0.24	0.61	GG Tau	-0.47	0.64
04385+2550	0.35	0.31	GH Tau	-0.75	0.26
AA Tau	-0.65	0.35	GI Tau	-0.47	0.51
AB Aur	-0.05	1.08	GK Tau	-0.20	1.03
BP Tau	-0.48	0.55	GM Aur	0.46	1.19
CI Tau	-0.54	0.54	GN Tau	-0.75	0.59
CoKu Tau/3	-0.95	0.41	GO Tau	-0.37	0.40
CoKu Tau/4	0.95	0.85	Haro 6-13	0.15	0.35
CW Tau	-0.83	0.16	Haro 6-37	-0.87	0.18
CX Tau	-0.14	0.48	HK Tau	0.09	0.39
CY Tau	-1.22	0.12	HN Tau	-0.45	0.51
CZ Tau	-0.01	0.53	HO Tau	-0.66	0.58
DD Tau	-0.64	0.21	HP Tau	-0.07	0.48
DE Tau	-0.44	0.43	HQ Tau	-0.50	0.70
DF Tau	-1.13	0.17	IP Tau	-0.45	0.99
DG Tau	0.00	0.00	IQ Tau	-1.12	0.35
DH Tau	-0.67	0.70	IS Tau	-0.85	0.44
DK Tau	-0.72	0.83	IT Tau	-1.05	0.14
DL Tau	-0.67	0.09	LkCa 15	-0.36	1.47
DM Tau	0.72	0.96	MHO 3	0.94	0.69
DN Tau	-0.45	0.22	RW Aur	-0.50	0.32
DO Tau	-0.27	0.18	RY Tau	0.05	1.36
DP Tau	-0.23	0.35	SU Aur	0.37	0.98
DQ Tau	-0.38	0.14	T Tau	-0.04	-0.10
DR Tau	-0.61	0.27	UX Tau A	-0.08	0.15
DS Tau	-0.90	0.55	UY Aur	0.08	0.40
F04101+3103	0.75	1.03	UZ Tau	-0.66	0.45
F04147+2822	-0.75	0.56	V410 Anon13	-0.61	0.20
F04192+2647	-0.67	0.28	V710 Tau	-0.87	0.21
F04262+2654	-0.38	0.19	V773 Tau	-0.76	0.09
F04297+2246 A	-0.24	0.98	V807 Tau	-0.91	0.16
F04570+2520	-1.04	0.25	V836 Tau	-0.86	0.79
FM Tau	-0.19	0.72	V892 Tau	1.28	0.65
FN Tau	-0.04	0.39	V955 Tau	-0.78	0.24
FO Tau	-0.52	0.26	VY Tau	-0.63	0.49
FP Tau	-0.39	0.22	XZ Tau	-0.23	0.09
FQ Tau	-0.78	0.19	ZZ Tau IRS	-0.02	0.31
			ZZ Tau	-0.94	0.26

NOTE. — Spectral indices are defined as  $n \equiv d\log(\lambda F_\lambda)/d\log(\lambda)$ . See text for the definition of the strength of the 10- $\mu\text{m}$  feature,  $(F_{10}-F_{\text{cont}})/F_{\text{cont}}$ .

TABLE 5  
SPECTRAL INDICES OF THE CLASS II AND III OBJECTS IN OUR SAMPLE

Name	$n_{6-13}$	$n_{13-25}$	Name	$n_{6-13}$	$n_{13-25}$
<i>Class II Objects</i>					
04108+2910	-1.17	-0.55	GN Tau	-0.89	-0.63
04187+1927	-0.49	-0.66	GO Tau	-0.80	0.17
04200+2759	-0.47	-0.11	Haro 6-13	-0.56	0.90
04216+2603	-0.75	-0.33	Haro 6-37	-1.17	-0.53
04303+2240	-0.80	-0.74	HK Tau	-0.72	1.12
04370+2559	-0.37	-0.22	HN Tau	-0.70	-0.14
04385+2550	0.13	0.53	HO Tau	-0.89	-0.37
AA Tau	-0.87	-0.37	HP Tau	-0.43	0.37
AB Aur	-0.79	0.93	HQ Tau	-0.76	-0.17
BP Tau	-0.67	-0.24	IP Tau	-0.94	0.20
CI Tau	-0.95	-0.02	IQ Tau	-1.30	-0.90
CoKu Tau/3	-1.04	-0.91	IS Tau	-0.87	-0.89
CoKu Tau/4	-0.60	2.98	IT Tau	-1.38	-0.67
CW Tau	-1.26	-0.30	LkCa 15	-1.30	0.87
CX Tau	-0.37	0.14	MHO 3	0.72	1.10
CY Tau	-1.45	-0.95	RW Aur	-0.67	-0.27
CZ Tau	0.42	-0.61	RY Tau	-0.16	0.30
DD Tau	-0.73	-0.53	SU Aur	-0.32	1.26
DE Tau	-0.87	0.12	T Tau	-0.56	0.63
DF Tau	-1.36	-0.85	UX Tau A	-1.99	2.45
DG Tau	-0.20	0.24	UY Aur	-0.01	0.17
DH Tau	-1.69	0.66	UZ Tau	-0.92	-0.34
DK Tau	-1.00	-0.37	V410 Anon 13	-0.91	-0.31
DL Tau	-0.78	-0.54	V710 Tau	-1.07	-0.63
DM Tau	-0.11	1.82	V773 Tau	-1.10	-0.34
DN Tau	-0.60	-0.27	V807 Tau	-1.61	0.01
DO Tau	-0.56	0.08	V836 Tau	-1.37	-0.20
DP Tau	-0.43	0.02	V892 Tau	1.75	0.53
DQ Tau	-0.47	-0.28	V955 Tau	-0.89	-0.68
DR Tau	-0.88	-0.27	VY Tau	-1.11	-0.02
DS Tau	-1.03	-0.73	XZ Tau	-0.35	-0.10
F04101+3103	0.97	0.43	ZZ Tau IRS	-0.42	0.49
F04147+2822	-0.83	-0.70	ZZ Tau	-1.15	-0.68
F04192+2647	-1.10	-0.10			
F04262+2654	-0.89	0.30	<i>Class III Objects</i>		
F04297+2246 A	-0.41	-0.01	Anon 1	-2.78	-2.71
F04570+2520	-0.79	-1.37	FF Tau	-2.76	-2.70
FM Tau	-0.45	0.14	HBC 388	-2.78	-3.02
FN Tau	-0.29	0.27	HBC 427	-2.85	-0.70
FO Tau	-0.82	-0.18	HD 283572	-2.85	-2.95
FP Tau	-0.84	0.21	IW Tau	-2.82	-2.69
FQ Tau	-1.12	-0.36	LkCa 3	-2.81	-2.65
FS Tau	-0.56	0.37	LkCa 4	-2.74	-2.72
FT Tau	-0.62	-0.31	LkCa 5	-2.77	-3.06
FV Tau	-0.83	-0.42	LkCa 7	-2.94	-2.46
FX Tau	-1.05	0.02	V410 Tau	-2.78	-5.19
FZ Tau	-1.14	-0.56	V410 Xray 3	-2.89	-1.61
GG Tau	-0.79	-0.05	V819 Tau	-2.57	-0.67
GH Tau	-1.26	-0.10	V826 Tau	-2.80	-2.68
GI Tau	-0.55	-0.40	V827 Tau	-2.77	-3.13
GK Tau	-0.45	0.12	V830 Tau	-2.65	-2.99
GM Aur	-0.91	2.28	V928 Tau	-2.76	-2.72

NOTE. — Spectral indices are defined as  $n \equiv d \log(\lambda F_\lambda) / d \log(\lambda)$ .

TABLE 6  
IRS TAURUS MEDIAN (K5-M2 SPECTRAL TYPES)

Wavelength [ $\mu\text{m}$ ]	Median [ $\log(\nu F_\nu)$ ] <sup>a</sup>	Lower Quartile [ $\log(\nu F_\nu)$ ] <sup>a</sup>	Upper Quartile [ $\log(\nu F_\nu)$ ] <sup>a</sup>
1.25 <sup>b</sup>	-9.039	-9.092	-9.013
1.65 <sup>b</sup>	-9.035	-9.035	-9.035
2.17 <sup>b</sup>	-9.163	-9.195	-9.114
5.70	-9.764	-9.879	-9.614
7.10	-9.873	-10.060	-9.735
8.00	-9.905	-10.081	-9.712
9.20	-9.789	-9.967	-9.552
9.80	-9.793	-9.942	-9.519
11.30	-9.902	-10.060	-9.615
12.30	-10.034	-10.234	-9.763
13.25	-10.060	-10.304	-9.787
16.25	-10.066	-10.237	-9.777
18.00	-10.030	-10.182	-9.725
21.00	-10.037	-10.204	-9.722
25.00	-10.093	-10.278	-9.778
30.00	-10.185	-10.404	-9.839
34.00	-10.229	-10.461	-9.865

NOTE. — <sup>a</sup> Units of median, lower and upper quartiles are  $\text{ergs s}^{-1} \text{cm}^{-2}$ .

<sup>b</sup> The median at these 3 wavelengths was constructed from reddening-corrected 2MASS data.